Use of Parametric Equations of Motion to Study Metastable States

A thesis submitted in fulfilment of the requirements

for the degree of Doctor of Philosophy

by

Deepak Kumar

Roll No. 206122103

Under the Guidance of

Prof. Ashish Kumar Gupta

DEPARTMENT OF CHEMISTRY

INDIAN INSTITUTE OF TECHNOLOGY GUWAHATI

GUWAHATI 781039, ASSAM, INDIA

Dedicated to my beloved Grandparents and parents.

Certificate

This is to certify that the thesis entitled **"Use of Parametric Equations of Motion to Study Metastable States"**, submitted by **Deepak Kumar** to the Indian Institute of Technology Guwahati, for the award of the degree of **Doctor of Philosophy** in Chemistry, is a record of the original, bona fide research work carried out by him under my supervision and guidance. The thesis has reached the standards fulfilling the requirements of the regulations related to the award of the degree.

The results contained in this thesis have not been submitted in part or in full to any other University or Institute for the award of any degree or diploma to the best of our knowledge.

....

Prof. Ashish Kumar Gupta
Department of Chemistry,
Indian Institute of Technology Guwahati.

Declaration

This is to certify that the thesis titled **"Use of Parametric Equations of Motion to Study Metastable States"** has been authored by me. It presents the research conducted by me under the supervision of **Prof. Ashish Kumar Gupta**.

To the best of my knowledge, it is an original work, both in terms of research content and narrative, and has not been submitted elsewhere, in part or in full, for a degree. Where others' ideas and words have been included, I have adequately cited and referenced the original source.

Deepak Kumar
Roll No. 206122103
Department of Chemistry
Indian Institute of Technology Guwahati

Acknowledgements

First of all, I would like to express my deepest gratitude to my supervisor, Professor Ashish Kumar Gupta, for his immense support throughout my PhD journey. The in-depth discussions and relentless focus on problem-solving have significantly shaped my research. His profound knowledge and vast experience have been a constant source of inspiration. Without his help with both minor and major challenges throughout my research, none of the work presented here would have taken shape.

I would also like to thank my Doctoral Committee members: Prof. Aditya Narayan Panda, Prof. Sumana Dutta, and Prof. Manabendra Sarma for their continuous support and valuable advice.

I am grateful to IIT Guwahati for providing the PARAM-ISHAN and PARAM-KAMRUPA supercomputing facilities, as well as for the financial support I received.

Additionally, I extend my sincere appreciation to my labmates Hrishikesh Rajbongshi, Dr. Mwdansar Banuary, and Dr. Rolly for the pleasant atmosphere they created during work and for their assistance with various research tasks.

I would also like to express my gratitude to my friends from college, IITM, IITG, and school, especially Gaurav, Anshumaan, Mohit and Shivam. I consider myself very fortunate to have shared my PhD journey with Shubham, Anand, Palak, Hrishikesh, Jagynesh, Vishwa, Maitery, Ritvika, Kirti, Abhay, Vishal, Ajit, Sourav, Chahal, Ravi Mishra, Rohit, Ravi Vashist, Rabu, Roop, Malay, Srijan, Biman and many more. I'm grateful to everyone mentioned here and those not mentioned. A special mention goes to Shubham, from whom I have learned a lot, and who has been a constant source of motivation. Our numerous discussions on research and problem-solving have had a significant impact on my understanding of certain issues.

Last but not least, I would like to express my gratitude to my parents and my younger brother, Divesh, for their unconditional love and support, and for being there for me at every stage of my life.

Abstract

Name of the student: **Deepak Kumar** Roll No: **206122103**
Degree for which submitted: **PhD** Department: **Department of Chemistry**
Thesis title: **Use of Parametric Equations of Motion to Study Metastable States**
Thesis supervisors: **Prof. Ashish Kumar Gupta**

In this thesis, a “resonance” describes an electronically metastable state, that is, a state of a metastable anion that lies energetically above the ground state of the associated neutral molecule. These metastable states can decay by losing an electron, a process known as autodetachment, or by fragmenting into a stable anion and a radical, which is called dissociative electron attachment (DEA). In studying these metastable states, it is crucial to identify the Lowest Unoccupied Molecular Orbital (LUMO), as this is the orbital that will be filled by an electron. In this context, we have developed a methodology that utilizes the Parametric Equations of Motion (PEM) with the nuclear charge stabilization method to identify the LUMO obtained from the Self-Consistent-Field (SCF) solution. This approach demonstrates stability across different basis sets, including those with diffuse functions.

However, a common issue with the SCF solution of metastable anion is that it tends to converge to a minimum energy state with an additional electron occupying the most diffuse orbital present in the basis set. As diffuse functions are increased, this solution typically converges into that of a neutral molecule and a free electron, a situation referred to as variational collapse. To address this, we have introduced a modified PEM approach in conjunction with the nuclear charge stabilization to obtain a meaningful SCF solution for a metastable anion. Here, the SCF solution for an anion with a higher nuclear charge serves as the starting point, where the anion remains bound. The modified PEM is then executed until the additional nuclear charge approaches zero, ultimately producing the SCF solution for the metastable

anion. A critical aspect of obtaining meaningful SCF solutions for metastable anions is maintaining a fixed occupation number for the orbital corresponding to the singly occupied molecular orbital throughout the PEM calculation. Furthermore, an alternative solution is provided to prevent variational collapse for metastable anions which involves removing the non-physical pseudo-continuum states at the SCF stage and implementing the process in a non-Hermitian domain, where lifetime of the electron-attached state is also accessed.

Additionally, an alternative approach named PEM-CAP has been developed for applying the Complex Absorbing Potential (CAP) at the Hartree-Fock level. This methodology was successfully applied to the uracil molecule, where identification of multiple resonances is also achieved for the first time using the nuclear charge stabilization method in conjunction with PEM. Finally, an application of parametric equations of motion to calculate the resonances in the physical limit of $\eta = 0$ for the complex absorbing potential is also discussed. In this physical limit of $\eta = 0$, the effects of the CAP are eliminated, and complex values are still obtained for $\eta = 0$, indicating reflection-free results. To eliminate the artificial reflections caused by CAP, a methodology is introduced that employs a backward PEM-CAP approach (i.e., starting from higher CAP strength parameter η to $\eta = 0$).

Contents

Acknowledgements iv

List of Figures x

List of Tables xvi

Abbreviations xix

Symbols xxii

List of Publications xxiii

1 Introduction 1
- 1.1 Resonance . . . 1
- 1.2 Theoretical Background . . . 2
  - 1.2.1 Complex Scaling Method . . . 3
  - 1.2.2 Exterior Complex Scaling Method . . . 5
  - 1.2.3 Complex Basis Functions Method . . . 6
  - 1.2.4 Complex Absorbing Potential . . . 6
  - 1.2.5 Conventional Stabilization Methods . . . 8
  - 1.2.6 Extrapolation Methods . . . 8
- 1.3 Methodology . . . 9
  - 1.3.1 Hartree-Fock . . . 9
  - 1.3.2 Nuclear Charge Stabilization Method . . . 10
  - 1.3.3 Implementation of Nuclear Charge Stabilization Method via Parametric Equations of Motion . . . 11

- 1.3.4 Parametric Equations of Motion-Complex Absorbing Potential (PEM-CAP) Approach . . . 13
- 1.3.5 Second-order Dilated Electron Propagator (SoDEP) approach 14
- 1.4 Motivation of the Thesis . . . 15

2 Precise Identification of the Lowest Unoccupied Molecular Orbital using the Parametric Equations of Motion 18

- 2.1 Introduction . . . 18
- 2.2 Results and Discussion . . . 21
  - 2.2.1 Pre-defined basis sets without extra augmentations . . . 21
    - 2.2.1.1 Identification of $\pi^\star$ orbital of neutral N_2 molecule . . 22
    - 2.2.1.2 Identification of $\pi^\star$ orbital of neutral C_2H_4 and neutral C_2H_2 molecule . . . 28
  - 2.2.2 Effect of additional diffuse basis function . . . 36
    - 2.2.2.1 $\pi^\star$ orbital of neutral C_2H_4 molecule for different basis sets . . . 36
    - 2.2.2.2 $\pi^\star$ orbital of neutral C_2H_2 molecule for different basis sets . . . 52
- 2.3 Concluding Remarks . . . 65

3 Self-Consistent-Field Solution for Metastable Anions using Bound-State Method 67

- 3.1 Introduction . . . 67
  - 3.1.1 Results and Discussion . . . 69
  - 3.1.2 Ethylene anion ($C_2H_4^-$) . . . 69
  - 3.1.3 Acetylene anion ($C_2H_2^-$), Dinitrogen anion (N_2^-) and Formaldehyde anion ($HCHO^-$) . . . 84
- 3.2 Concluding Remarks . . . 84

4 Application of Parametric Equations of Motion in non-Hermitian Domain using Complex Absorbing Potential 86

- 4.1 Introduction . . . 86
- 4.2 Results and Discussion . . . 88
  - 4.2.1 Ethylene (C_2H_4) . . . 88
  - 4.2.2 Uracil . . . 91
- 4.3 Concluding Remarks . . . 98

5 Self-Consistent-Field Solution for Metastable Anions after the Removal of Pseudo-Continuum States 99

- 5.1 Introduction . . . 99
- 5.2 Methodology . . . 101
- 5.3 Results and Discussion . . . 103
  - 5.3.1 Ethylene anion ($C_2H_4^-$) . . . 103

5.3.2 Formaldehyde anion ($HCHO^-$) 111
5.4 Concluding Remarks 114

6 Reflection-Free CAP using Parametric Equations of Motion 115
6.1 Introduction 115
6.2 Methodology 117
6.3 Results and Discussion 118
6.4 Concluding Remarks 125

7 Summary and Conclusion 126

A Molecular Coordinates 131

Bibliography 133

List of Figures

2.1 Plots of few virtual orbitals of neutral N_2 molecule for 6-311G basis set. The degenerate states LUMO and LUMO+1 are clearly identified as $\pi^\star$ antibonding orbitals. 23

2.2 Plots of few virtual orbitals of neutral N_2 molecule for cc-pVTZ basis set. The degenerate states LUMO and LUMO+1 are clearly identified as $\pi^\star$ antibonding orbitals. 23

2.3 Plots of few virtual orbitals of neutral N_2 molecule for aug-cc-pVDZ basis set. The degenerate states LUMO+1 and LUMO+2 are clearly identified as $\pi^\star$ antibonding orbitals. 24

2.4 Plots of few virtual orbitals of neutral N_2 molecule for aug-cc-pVTZ basis set. The degenerate states LUMO+4 and LUMO+5 are clearly identified as $\pi^\star$ antibonding orbitals. 24

2.5 Plot of the few lowest virtual orbital energies in Hartree (on y-axis) as function of additional nuclear charge (on x-axis) of neutral N_2 molecule for different basis sets. The degenerate states LUMO and LUMO+1 are getting more stabilized for 6-311G, cc-pVTZ basis sets, while degenerate states(i.e., LUMO+1 and LUMO+2) and degenerate states (i.e., LUMO+4 and LUMO+5) are getting stabilized in the case of aug-cc-pVDZ and aug-cc-pVTZ basis sets respectively as the nuclear charge increases. The PEM solution agrees well with diagonalization results (represented by green dots). 26

2.6 Plots of few virtual orbitals of neutral C_2H_4 molecule for 6-311G basis set. LUMO is perfect candidate for $\pi^\star$ antibonding orbital. 28

2.7 Plots of few virtual orbitals of neutral C_2H_4 molecule for cc-pVTZ basis set. LUMO is perfect candidate for $\pi^\star$ antibonding orbital. . . . 29

2.8 Plots of few virtual orbitals of neutral C_2H_4 molecule for aug-cc-pVDZ basis set. LUMO+4 is perfect candidate for $\pi^\star$ antibonding orbital. . 29

2.9 Plots of few virtual orbitals of neutral C_2H_4 molecule for aug-cc-pVTZ basis set. LUMO+4 is perfect candidate for $\pi^\star$ antibonding orbital. . 30

2.10 Plots of few virtual orbitals of neutral C_2H_2 molecule for 6-311G basis set. The degenerate states LUMO+2 and LUMO+3 are clearly identified as $\pi^\star$ antibonding orbitals. 30

2.11 Plots of few virtual orbitals of neutral C_2H_2 molecule for cc-pVTZ basis set. The degenerate states LUMO+2 and LUMO+3 are clearly identified as $\pi^\star$ antibonding orbitals. 31

2.12 Plots of few virtual orbitals of neutral C_2H_2 molecule for aug-cc-pVDZ basis set. The degenerate states LUMO+2 and LUMO+3 are clearly identified as $\pi^\star$ antibonding orbitals. 31

2.13 Plots of few virtual orbitals of neutral C_2H_2 molecule for aug-cc-pVTZ basis set. The degenerate states LUMO+4 and LUMO+5 are clearly identified as $\pi^\star$ antibonding orbitals. 32

2.14 Plot of the few lowest virtual orbital energies in Hartree (on y-axis) as function of additional nuclear charge (on x-axis) of neutral C_2H_4 molecule for different basis sets. For increasing nuclear charge, the LUMO state is more stabilized for the 6-311G and cc-pVTZ basis sets, while LUMO+4 is more stabilized for the aug-cc-pVDZ and aug-cc-pVTZ basis sets. The PEM solution agrees well with diagonalization results (represented by green dots). 33

2.15 Plot of the few virtual lowest orbital energies in Hartree (on y-axis) as function of additional nuclear charge (on x-axis) of neutral C_2H_2 molecule for different basis sets. The degenerate states (i.e.,LUMO+2 and LUMO+3) are getting more stabilized for 6-311G,cc-pVTZ and aug-cc-pVDZ basis sets, while degenerate states (i.e., LUMO+4 and LUMO+5) are getting stabilized in the case of aug-cc-pVTZ basis set as the nuclear charge increases. The PEM solution agrees well with diagonalization results (represented by green dots). 34

2.16 Plot of the few lowest virtual orbital energies in Hartree (on the y-axis) as function of additional nuclear charge (on the x-axis) of neutral C_2H_4 molecule using cc-pVDZ+np basis set. The PEM solution agrees well with diagonalization results (represented by green dots). . 38

2.17 Plot of the virtual orbitals having $\pi^\star$ antibonding character involved in avoided crossings with true LUMO using cc-pVDZ+10p basis set of neutral C_2H_4 molecule. 39

2.18 Same as Figure 2.17 using cc-pVDZ+9p basis set. 40

2.19 Same as Figure 2.17 using cc-pVDZ+8p basis set. 40

2.20 Same as Figure 2.17 using cc-pVDZ+7p basis set. 41

2.21 Same as Figure 2.17 using cc-pVDZ+6p basis set. 41

2.22 Same as Figure 2.17 using cc-pVDZ+5p basis set. 42

2.23 Same as Figure 2.17 using cc-pVDZ+4p basis set. 42

2.24 Same as Figure 2.17 using cc-pVDZ+3p basis set. 42

2.25 Same as Figure 2.17 using cc-pVDZ+2p basis set. 43

2.26 Same as Figure 2.17 using cc-pVDZ+1p basis set. 43

2.27 Same as Figure 2.17 using cc-pVDZ basis set. 43

2.28 Plot of the virtual orbital energies in Hartree (on y-axis) of $\pi^\star$ antibonding type orbitals involved in avoided crossing as function of additional nuclear charge (on x-axis) of neutral C_2H_4 molecule for cc-pVDZ+np basis set. 45

2.29 Plot of the few lowest virtual orbital energies in Hartree (on the y-axis) as function of additional nuclear charge (on the x-axis) of neutral C_2H_4 molecule using cc-pVDZ+np basis set. The plot corresponds to modified PEM case I. 48

2.30 Plot of the few lowest virtual orbital energies in Hartree (on the y-axis) as function of additional nuclear charge (on the x-axis) of neutral C_2H_4 molecule using cc-pVDZ+np basis set. The plot corresponds to modified PEM case II. 50

2.31 Plot of Orbital probability density (on the y-axis) vs r in angstrom (on the the x-axis) for true LUMO and the most diffuse state involved in avoided crossing of C_2H_4 using cc-pVDZ+np basis set. 51

2.32 Plot of the few lowest virtual orbital energies in Hartree (on the y-axis) as function of additional nuclear charge (on the x-axis) of neutral C_2H_2 molecule using cc-pVDZ+np basis set. The PEM solution agrees well with diagonalization results (represented by green dots). . 54

2.33 Plot of the virtual orbitals having $\pi^\star$ antibonding character involved in avoided crossings with true LUMO using cc-pVDZ+10p basis set for neutral C_2H_2 molecule. 55

2.34 Same as Figure 2.33 using cc-pVDZ+9p basis set. 56

2.35 Same as Figure 2.33 using cc-pVDZ+8p basis set. 56

2.36 Same as Figure 2.33 using cc-pVDZ+7p basis set. 57

2.37 Same as Figure 2.33 using cc-pVDZ+6p basis set. 57

2.38 Same as Figure 2.33 using cc-pVDZ+5p basis set. 58

2.39 Same as Figure 2.33 using cc-pVDZ+4p basis set. 58

2.40 Same as Figure 2.33 using cc-pVDZ+3p basis set. 58

2.41 Same as Figure 2.33 using cc-pVDZ+2p basis set. 59

2.42 Same as Figure 2 using cc-pVDZ+1p basis set. 59

2.43 Same as Figure 2.33 using cc-pVDZ basis set. 59

2.44 Plot of the few lowest virtual orbital energies in Hartree (on the y-axis) as function of additional nuclear charge (on the x-axis) of neutral C_2H_2 molecule using cc-pVDZ+np basis set. The plot corresponds to modified PEM case I. 61

2.45 Plot of the few lowest virtual orbital energies in Hartree (on the y-axis) as function of additional nuclear charge (on the x-axis) of neutral C_2H_2 molecule using cc-pVDZ+np basis set. The plot corresponds to modified PEM case II. 63

2.46 Plot of Orbital probability density (on the y-axis) vs r in angstrom (on the the x-axis) for true LUMO state of C_2H_2 using cc-pVDZ+np basis set. 65

3.1 Plot of Orbital probability density (on the y-axis) vs r in angstrom (on the the x-axis) for SOMO of $C_2H_4^-$ using different basis sets. . . . 70
3.2 SOMO's orbital picture for different basis sets (i.e. 6-311G, cc-pVDZ, aug-cc-pVDZ, aug-cc-pVTZ and aug-cc-pVQZ) for $C_2H_4^-$. These orbital pictures corresponds to SCF solution at $z = 0$ without implementing PEM. 70
3.3 Plot of the orbital energies in Hartree (on y-axis) as function of additional nuclear charge (on x-axis) of $C_2H_4^-$ using diffrent basis sets (i.e. 6-311G, cc-pVDZ, aug-cc-pVDZ, aug-cc-pVTZ and aug-cc-pVQZ). f) Zoom in on the aug-cc-pVDZ results to clearly see the avoided crossing. The PEM solution agrees well with diagonalization results (represented by green dots). These solutions correspond to the SCF solution for anions obtained by diagonalization and the PEM-based approach. 72
3.4 Plot of the orbital energies in Hartree (on the y-axis) as function of additional nuclear charge (on the x-axis) of $C_2H_4^-$ molecule using cc-pVDZ+np basis set. These charge stabilization plots are obtained by using the PEM calculations without modification. 75
3.5 Plot of Orbital probability density (on the y-axis) vs r in angstrom (on the the x-axis) for SOMO of $C_2H_4^-$ using cc-pVDZ+np basis set, with the additional nuclear charge set to zero. 76
3.6 Plot of the orbital energies in Hartree (on the y-axis) as function of additional nuclear charge (on the x-axis) of $C_2H_4^-$ using cc-pVDZ+np basis set. These charge stabilization plots are obtained by applying modified PEM. 79
3.7 Plot of the orbital energies in Hartree (on the y-axis) as function of additional nuclear charge (on the x-axis) of $C_2H_4^-$ using cc-pVDZ+4p/5p/6p/7p basis sets. These charge stabilization plots are obtained by applying modified PEM. Figures a-d shows that results obtained from modified PEM and from the ϵ-matrix (i.e. from equation 3.2) are indistinguishable 80
3.8 Plot of Orbital probability density (on the y-axis) vs r in angstrom (on the the x-axis) for SOMO of $C_2H_4^-$ using cc-pVDZ+np basis set. These plots are obtained after applying the modified PEM. In all cases electron density is much localized near to the nucleus. 81
3.9 Plot of Orbital probability density (on the y-axis) vs r in angstrom (on the the x-axis) for SOMO of $C_2H_4^-$ using different basis sets. These plots are obtained after applying the modified PEM. 82
3.10 SOMO's orbital picture for different basis sets (i.e. aug-cc-pVDZ, aug-cc-pVTZ and aug-cc-pVQZ) for $C_2H_4^-$. These orbital pictures corresponds to SCF solution obtained by applying the modified PEM. 82

4.1 $\eta-$trajectories for C_2H_4 using cc-pVDZ+5p and cc-pVDZ+8p basis sets respectively. Dot represents the results from Diagonalization approach while line plot is obtained via PEM approach. 89

4.2 Charge stabilization plot for C_2H_4 at η_{opt} using cc-pVDZ+5p and cc-pVDZ+8p basis sets respectively at CAP/KT level. The red line represents the true resonance state. 90

4.3 $\eta-$trajectories for C_2H_4 using cc-pVDZ+5p and aug-cc-pVDZ+5p basis sets at CAP/KT and CAP/SoDEP level. $\star$ represent the resonance energy at η_{opt} value. 91

4.4 (a) $\eta-$trajectories for uracil using cc-pVDZ+4p basis set. Dot represents the results from Diagonalization approach while line plot is obtained via PEM approach. (b) Charge stabilization plot for uracil at η_{opt} using cc-pVDZ+4p basis set at CAP/KT level. 94

4.5 Identified LUMO's orbital picture for uracil at η_{opt} value using cc-pVDZ+4p basis set at CAP/KT level. Isovalue is chosen as 0.02. . . 94

4.6 $\eta-$trajectories for different states of uracil using cc-pVDZ+4p basis set at CAP/KT level. $\star$ represent the resonance energy at η_{opt} value. 95

4.7 $\eta-$trajectories for different states of uracil using cc-pVDZ+5p basis set at HF level. $\star$ represent the resonance energy at η_{opt} value. . . . 95

4.8 $\eta-$trajectories for different states of uracil using cc-pVDZ+5s5p basis set at CAP/KT level. $\star$ represent the resonance energy at η_{opt} value. 95

4.9 $\eta-$trajectories for different states of uracil using cc-pVDZ+5p1d basis set at CAP/KT level. $\star$ represent the resonance energy at η_{opt} value. 96

4.10 $\eta-$trajectories for different states of uracil using cc-pVDZ+5p2d basis set at CAP/KT level. $\star$ represent the resonance energy at η_{opt} value. 96

4.11 $\eta-$trajectories for different states of uracil using cc-pVDZ+4p basis set at CAP/SoDEP level. $\star$ represent the resonance energy at η_{opt} value. 97

5.1 The $\eta-$trajectories for $^2B_{2g}$ resonance in $C_2H_4{}^-$ corresponding to different box-size parameter using cc-pVDZ+5p basis set. 106

5.2 The η-trajectories corresponding to the $^2B_{2g}$ resonance in $C_2H_4^-$ using various basis sets at both the HF and MP2 levels. 109

5.3 The η-trajectories corresponding to the $^2B_1$ resonance in $HCHO^-$ using various basis sets at both the HF and MP2 levels. 112

6.1 η-trajectory plot corresponding to Forward η-trajectory obtained by diagonalization(represented by orange dots) and backward PEM-CAP calculations starting from different η values (i.e., represented by red dots) using grid basis with 200 functions. In the first two top panels, red dots are on top of the orange dots as they follow the same trajectories. 120

6.2 η-trajectory plot corresponding to Forward η-trajectory obtained by diagonalization(represented by violet dots) and backward PEM-CAP calculation goes to $\eta = 0$ starting from $\eta = 0.0040$ (i.e., represented by red dots) using grid basis with 200 functions. Complex scaling results are also plotted for comparison and represented by orange dots. 122

6.3 η-trajectory plot corresponding to backward PEM-CAP calculation goes to $\eta = 0$ starting from $\eta = 0.0040$ for different box sizes using grid basis with 200 functions. Complex scaling results are also plotted for comparison and represented by red dots. 123
6.4 Wavefunction plot corresponding to bound state and first three resonances using grid basis with 300 functions at $\eta = 0$ obtained after backward PEM-CAP approach. 124

List of Tables

2.1 Tabular data for orbital energies(in Hartree) of neutral N_2 molecule for different basis sets. The identified LUMO energies are marked in bold. 27

2.2 Tabular data for orbital energies(in Hartree) of neutral C_2H_4 molecule for different basis sets. The identified LUMO energies are marked in bold. 35

2.3 Tabular data for orbital energies(in Hartree) of neutral C_2H_2 for different basis sets. The identified LUMO energies are marked in bold. . . 35

2.4 Orbital energies of identified LUMOs (in Hartree) of neutral C_2H_4 molecule using different basis sets upto extra augmentation of 10 p-type functions. 52

2.5 Orbital energies of identified LUMOs (in Hartree) of neutral C_2H_2 molecule using different basis sets upto extra augmentation of 10 p-type functions. 64

3.1 HF and MP2 energies of neutral and anionic C_2H_4 using different basis sets. Vertical electron affinities at HF and MP2 level are represented as Δ^{HF} and Δ^{MP2} respectively in eV. 71

3.2 HF and MP2 energies for neutral and anionic C_2H_4 using cc-pVDZ+np sets. Vertical electron affinities at HF and MP2 level are represented as Δ^{HF} and Δ^{MP2} respectively in eV. 81

3.3 HF and MP2 energies of neutral and anionic C_2H_4 using aug-cc-pVDZ, aug-cc-pVTZ, and aug-cc-pVQZ basis sets. Vertical electron affinities at HF and MP2 level are represented as Δ^{HF} and Δ^{MP2} respectively in eV. The results correspond to the SCF solution after applying modified PEM. 83

3.4 HF and MP2 energies of neutral and anionic C_2H_4 for different basis sets. Experimental result is included for comparison of calculated vertical electron affinities. 83

3.5 HF and MP2 energies of neutral and anionic C_2H_2, N_2, and HCHO for different basis sets. Experimental results are included for comparison of calculated vertical electron affinities. 84

4.1 Resonance Energies and widths (in parenthesis) of C_2H_4 obtained in this work at CAP/KT and CAP/SoDEP level using different basis set, and comparisons with experimental result. 92
4.2 Energy corresponding to the dipole-bound state of uracil using different basis sets at HF level. 92
4.3 Resonance Energies and widths (in parenthesis) of uracil obtained in this work at the CAP/KT-level using different basis sets 96
4.4 Tabular Data for resonance Energies and widths (in parenthesis) of uracil obtained in this work at the CAP/SoDEP level using cc-pVDZ+4p basis set, along with comparisons to previous theoretical and experimental results. 97

5.1 Tabular data for CPU time taken with all the states and after removing pseudo-continuum states using cc-pVTZ+7p/8p basis sets for C_2H_4 104
5.2 The table presents the correlation energy obtained using conventional SCF method, as well as the results after removing pseudo-continuum states. It also includes the differences and percentage differences, along with the number of states removed using various basis sets for neutral C_2H_4 molecule. 105
5.3 Resonance energies for $^2B_{2g}$ resonance in $C_2H_4^-$ at HF-level are tabulated for different box size using cc-pVDZ+5p basis set. 106
5.4 Tabular data for HF and MP2 energies obtained with all the states and with removal of states using cc-pVDZ+4p for C_2H_4 107
5.5 Tabular data for HF and MP2 energies obtained with all the states and with removal of states using cc-pVDZ+5p for HCHO 107
5.6 Resonance energies for $^2B_{2g}$ resonance in $C_2H_4^-$ at both HF and MP2 methods are presented using different basis sets. 110
5.7 Tabular data corresponding to previous theoretical and experimental result for resonance energy and width of the $^2B_{2g}$ resonance in in $C_2H_4{}^-$.110
5.8 The table presents the correlation energy obtained using conventional SCF method, as well as the results after removing pseudo-continuum states. It also includes the differences and percentage differences, along with the number of states removed using various basis sets for neutral HCHO molecule. 111
5.9 Resonance energies for $^2B_1$ resonance in HCHO$^-$ at both HF and MP2 methods are presented using different basis sets. 113
5.10 Tabular data corresponding to previous theoretical and experimental result for resonance Energy and width of the $^2B_1$ resonance of HCHO$^-$.113

6.1 Tabular data for resonance energies (in a.u.) corresponding to first three resonances obtained at $\eta = 0$ after performing back-PEM starting from different η-values using grid basis with 200 functions. Complex scaling results are also obtained for comparison using grid basis with 2000 functions 121

6.2 Tabular data for resonance energies (in a.u.) corresponding to first three resonances obtained at $\eta = 0$ after performing back-PEM for different boxes using grid basis with 200 functions. 123

Abbreviations

LEEs	Low Energy Electrons
TDSE	Time Dependent Schrodinger Equation
TISE	Time Independent Schrodinger Equation
DEA	Dissociative Electron Attachment
PEM	Parametric Equations of Motion
CS	Complex Scaling
BO	Born–Oppenheimer
HF	Hartree-Fock
RHF	Restricted Hartree-Fock
UHF	Unrestricted Hartree-Fock
SE	Static-Exchange
SCF	Self Consistent Field
MCSCF	Multi Configurational Self Consistent Field
DFT	Density Functional Theory
TDDFT	Time-dependent Density Functional Theory

ECS	Exterior Complex Scaling
MSES	Modified Smooth Exterior Scaling
CBFs	Complex Basis Functions
CAP	Complex Absorbing Potential
IP	Ionization Potential
EA	Electron Affinity
VEA	Vertical Electron Affinity
SoDEP	Second Order Dilated Electron Propagator
KT	Koopmans' Theorem
MO	Molecular Orbital
LUMO	Lowest Unoccupied Molecular Orbital
HOMO	Highest Occupied Molecular Orbital
SOMO	Singly Occupied Molecular Orbital
MP2	Second-Order Moller-Plesset Perturbation Theory
CI	Configuration Interaction
MRCI	Multi-reference Configuration Interaction
CCSD	Coupled Cluster Singles and Doubles
EOM-CCSD	Equation-of-Motion Coupled Cluster Singles and Doubles
SM	Stabilization Method
TNIs	Transient Negative Ions
SKT	Stabilized Koopmans' Theorem

GPA	Generalized Pade Approximation
SAC-CI	Symmetry-Adapted Cluster-Configuration Interaction
OBC	Outgoing Boundary Conditions

Symbols

ψ	psi
Γ	Gamma
η	eta
α	alpha
θ	theta
δ	delta
Δ	Delta
π	pi
σ	sigma
$\dagger$	dagger
ϕ	phi
ω	omega
λ	lambda
ϵ	epsilon
$\star$	asterisk
$\mathring{A}$	Angstrom

List of Publications

Publications from Thesis

1. Kumar, D., Gupta, A.K., Application of parametric equations of motion to study uracil anion. *J. Chem. Phys.* 2025, 163, 014103. *110.1063/5.0277968*.
2. Kumar, D., Banuary, M., Gupta, A.K., An innovative approach for precise identification of the Lowest Unoccupied Molecular Orbital using the Parametric Equation of Motion. *J. Chem. Theory Comput.* 2024, 20, 6009–6019. *10.1021/acs.jctc.4c00470*.
3. Kumar, D., Gupta, A.K., A unique approach to address avoided crossings in the charge stabilization curve for LUMO identification. *J. Chem. Phys.* 2024, 161, 094108. *10.1063/5.0225287*.
4. Kumar, D., Gupta, A.K., Self-consistent-field solution for unstable anions. *Phys. Rev. A* 2024, 110, 062821. *10.1103/PhysRevA.110.062821*.
5. Kumar, D., Gupta, A.K., Self-consistent-field solution for anions: Effect of removal of the pseudo-continuum states. *Under revision*.
6. Kumar, D., Gupta, A.K., Reflection free CAP using Parametric Equations of Motion. *In peer-review*.

Others

1. Banuary, M., Kumar, D., Gupta, A.K., Use of dilated electron propagator in conjunction with modified smooth exterior scaling method to characterize ^{2}S Be$^+$ (1s^{-1}), ^{2}S Ne$^+$ (1s^{-1}) Auger and ^2P Be$^-$ shape resonances. *New J. Chem.* 2024, 48, 4772-4782. *10.1039/D3NJ04908F*.

Chapter 1

Introduction

1.1 Resonance

Resonances are metastable states that decay slowly and have a finite lifetime, which is long enough to be characterized experimentally[1, 2, 3]. These metastable states have sufficient energy to break the system into two or more subsystems. In 1928, Gamow[4] provided the first description of resonance states while studying the α-decay of heavy nuclei. Since then, these resonances have been observed and characterized across various fields. These metastable states, or resonances, play a crucial role in nuclear, atomic, and molecular physics, mesoscopic physics, and chemical dynamics. Understanding these metastable states is essential for explaining various physical processes. This includes phenomena such as plasma quenching, electron-driven fragmentation of biomolecules like DNA and RNA, dissociative electron attachment (DEA)[5, 6, 7, 8, 9, 10], and radiation damage from radiotherapy. Furthermore, the discovery of DEA as a process that contributes to radiation-induced DNA damage is considered a significant breakthrough in cancer treatment research through radiotherapy. These metastable states are also relevant in the study of autoionization[11, 12] and the interstellar medium, or the formation of molecules in interstellar space[13, 14, 15, 16, 17]. Recent advances in light sources, particularly attosecond and X-ray spectroscopies[18, 19, 20, 21], have increased renewed interest in autoionizing states. The development of attosecond lasers is particularly noteworthy because the energies of these laser systems, typically falls within the extreme ultraviolet (XUV) range, can excite most molecules to metastable states that exist above the energy level of the cation[22].

In the field of chemistry, the significance of electronic decay, which involves unbound electrons, is becoming increasingly important. This includes phenomena such as core vacancies created by X-rays and metastable anions formed by the attachment of low-energy electrons. The metastable anions are formed due to electron-molecule collisions having a finite lifetime[23, 24, 25, 26, 27]. These anions are also known as transients anion or temporary anions. Experimental techniques, such as electron transmission spectroscopy[28], Photodetachment spectroscopy[29] etc., are used to detect these short-lived species.

Resonances can occur in different types based on their mechanisms. One example is shape resonances, which arise when an incident electron with non-zero angular momentum (i.e., creating a barrier in the potential) is temporarily trapped in the ground state of a molecule. Another type, known as core-excited resonances or Feshbach resonances, occurs when an electron is temporarily bound to an existing excited state of a target molecule.

1.2 Theoretical Background

Resonances are defined as eigenstates with complex eigenvalues that are obtained by applying outgoing boundary conditions to the eigenfunctions associated with a time-independent Hamiltonian. The resonance wave functions are asymptotically divergent and not square integrable and hence do not belong to the Hermitian domain of Hamiltonian. To address this issue, several advanced methods have been developed that impose outgoing boundary conditions for resonances. One such method employs non-Hermitian quantum mechanics, which includes techniques like complex scaling[30, 31, 32, 33], complex-absorbing potentials (CAP [34, 35, 36, 37], and smooth exterior scaling (SES [38, 39, 40, 41, 42, 43]. In non-Hermitian quantum mechanics (NHQM), resonances are linked to complex eigenvalues as

$$E = E_r - i\frac{\Gamma}{2} \tag{1.1}$$

where E$_r$ is the resonance position and Γ is the decay width, where $\tau = \frac{\hbar}{\Gamma}$ is the corresponding lifetime of the resonance.

Since resonance wave functions are not square integrable, their theoretical study poses significant challenges. Therefore, the primary goal of the techniques discussed is to make these divergent wave functions square integrable through appropriate mathematical transformations. Below is a brief description of the already developed methods and also the methodologies implemented in this thesis to study these metastable states.

1.2.1 Complex Scaling Method

Complex scaling (CS) method or "complex coordinate method" is one of the most widely used method for studying resonance states. The mathematical foundation of the CS method is based on the Balslev–Combes theorem[44, 45, 46]. It is important to note that the CS method relies on the analytic continuation of the Hamiltonian into the complex plane. Consequently, CS method is only applicable to Hamiltonians that have dilation-analytic potentials.

In the CS approach, a dilation transformation of the coordinates is performed as $r \rightarrow re^{i\theta}$. This scaling of all coordinates in the Hamiltonian by $e^{i\theta}$ transforms the resonance wavefunction into a form that is square-integrable. The discrete complex eigenvalues obtained from the non-Hermitian Hamiltonian operator (i.e., after the dilation transformation) are associated with resonance. Following the CS transformation, the asymptotic wavefunction changes from $\psi = e^{i(k_r+ik_{im})r}$ to a decaying form given by $\psi=$ e$^{i(k_r+ik_{im})re^{i\theta}}$, which on simplifying leads to $\psi=$ e$^{ir(k_r cos\theta - k_{im} sin\theta)}e^{-r(k_r sin\theta + k_{im} cos\theta)}$. The second term ensures that the wavefunction is square integrable. For $\theta > \theta_c$, the resonance wavefunction becomes squared-integrable because of their dumping forms at the asymptotic region where the critical value of θ_c is given by

$$\theta_c = arctan(\frac{\Gamma}{2(E_{res} - E_t)}) \tag{1.2}$$

with E$_t$ as threshold energy. For $\theta > \theta_c$, the resonance energies are independent of θ.

The Hamiltonian obtained through the dilation transformation of coordinates is not Hermitian; instead, it is a complex symmetric Hamiltonian. Therefore, the methods developed for bound states are not applicable, and modifications are necessary. One approach is to use a generalized variational principle based on a bi-orthogonal formulation. This bi-orthogonal variational principle serves as a complex variational principle that utilizes the c-product[1, 2, 3].

To study atomic resonances, implementing the CS method is quite straightforward. To describe the resonance properly, diffuse basis functions are necessary. In previous literatures, CS has been applied using various ab-initio methods to investigate resonances or metastable states, which includes Hartree-Fock (HF) [47, 48, 49], Density Functional Theory (DFT) [50], Multiconfigurational Self-Consistent Field (MCSCF) [51, 52] with standard basis sets augmented with additional diffuse functions.

However, applying CS to study molecular resonances is not as straightforward as it is for atomic resonances. The potential part of the Hamiltonian must be an analytical function[53] when employing CS. When CS is applied to molecular systems, the following transformations are carried out.

$$r_j \to e^{i\theta} r_j \tag{1.3}$$

$$R_k \to e^{i\theta} R_k \tag{1.4}$$

where $\{r_j\}$ and $\{R_k\}$ are the electronic and nuclear coordinates respectively and consequently the transformed Hamiltonian will have the following form

$$\hat{H}_{mol} = e^{-2i\theta}(\hat{T}_e + \hat{T}_N) + e^{-i\theta}(\hat{V}_{eN} + \hat{V}_{ee} + \hat{V}_{NN}) \tag{1.5}$$

where $\hat{T}_e$ & $\hat{T}_N$ is the kinetic energy operator of the electron and nucleus respectively and $\hat{V}_{eN}$, $\hat{V}_{NN}$ and $\hat{V}_{ee}$ are electron-nucleus, nucleus-nucleus and electron-electron potential energy operators. When CS method is applied with unscaled nuclear coordinates, the electron-nuclear attraction is not dilation analytic within the Born–Oppenheimer (BO) approximation. This means that it is not feasible to apply CS method in molecular systems for obtaining resonance position and resonance width. However, in 1979[54], it was demonstrated that this can be addressed by performing the analytical continuation of Hamiltonian matrix elements instead of scaling the Hamiltonian. Later, it is applied to investigate the shape resonances in various molecular systems[55, 56, 57, 58, 59].

1.2.2 Exterior Complex Scaling Method

The implementation of CS is more straightforward when the potential is dilation analytic; however, it presents significant numerical challenges when dealing with systems where the potential is not dilation analytic, such as in cases of resonance in molecular systems. To address this issue, Lipkin et al.[60] introduced a more general method known as exterior complex scaling (ECS) by using Simons[61] exterior-scaling procedure within the finite-basis-set approximation. It is applicable when the potential is dilation analytic in the asymptotic region. In the ECS method, scaling is applied only in the external region, where the potential remains dilation analytic. The variable r is scaled beyond a distance r_0 as follows:

$$z = \begin{cases} r, & r < r_0 \\ (r - r_0)e^{i\theta} + r_0, & r \geq r_0 \end{cases} \tag{1.6}$$

and the transformed Hamiltonian is given by

$$\hat{H}_\theta = -\frac{\hbar^2}{2M}\left[f^2(r)\frac{d^2}{dr^2} + (e^{-i\theta} - 1)\delta(r - r_0)\frac{d}{dr}\right] + V(z) \tag{1.7}$$

where the function f(r)is given by

$$f(r) \equiv \frac{dr}{dz} = \begin{cases} 1, & r < r_0 \\ e^{-i\theta}, & r \geq r_0 \end{cases} \tag{1.8}$$

In the context of three-dimensional many-body problems, complications arise due to the presence of a delta function potential term in the complex scaled Hamiltonian, as shown in equation (1.7)[62]. This presents challenges for simplifying numerical calculations using the ECS method to study resonance.

1.2.3 Complex Basis Functions Method

The Complex Basis Functions (CBF) method was introduced by McCurdy and Rescigno [63] and utilizes the unscaled molecular Hamiltonian. In this method, complex scaling is applied to the exponential part of the basis functions by a complex factor. In a Gaussian basis, this approach is asymptotically equivalent to employing basis functions with complex exponents.

Implementing this method with existing electronic structure codes necessitates the evaluation of one- and two-electron integrals over nonstandard basis functions. To successfully implement this method in electronic structure codes, existing electronic structure frameworks need to be modified to a greater extent. The shape resonance in molecular systems [64, 65, 66, 67, 68, 69] has been investigated using the CBFs method. Recently, White et al.[70, 71] applied the CBFs method to polyatomic molecules using the static-exchange (SE) and Hartree-Fock (HF) levels of theory.

1.2.4 Complex Absorbing Potential

The Complex Absorbing Potential (CAP) was first introduced by Jolicard and Austin and later modified by Riss and Meyer. Within the interaction region, the effect of a CAP is negligible; however, it becomes significant outside of this region, where it effectively "turns on." In this method, the Hamiltonian is perturbed by an appropriate potential to create an absorbing boundary condition. Through the CAP approach, divergent resonance wave functions are transformed into square-integrable wave functions. CAP remains appealing due to its straightforwardness and numerical simplicity.

In the CAP approach, a complex potential $-i\eta W$ is added to the physical Hamiltonian H_0,

$$H = H_0 - i\eta W \tag{1.9}$$

where η is a strength parameter and H has linear dependency on it. W is usually introduced only into the exterior region of the system such that it is zero inside the interaction region and has a finite value outside the interaction region, which can be described by the following equations,

$$W = \sum_{i=x,y,z} W_i \tag{1.10}$$

$$W_i = \begin{cases} 0, & |r_i| < r_i^0 \\ (r_i - r_i^0)^2, & |r_i| > r_i^0 \end{cases} \tag{1.11}$$

where r_i denotes the three Cartesian coordinates ($i = x, y, z$) and r_i^0 represents the CAP box-size parameter.

CAP is incorporated into the system Hamiltonian to make the resonance wavefunction square integrable. However, the artificial introduction of the CAP does perturb the Hamiltonian. The exact resonance eigenvalues and eigenfunctions can be obtained in the limit as ($\eta \to 0$) when using a complete basis set. In practice, for incomplete basis sets, a finite value of the CAP strength parameter (i.e., η) is necessary to accurately determine the resonance energies. The complex Hamiltonian matrix H(η) is diagonalized for a number of η values to obtain the resonance energy. The η trajectories are examined by using logarithmic velocity $\eta \, \frac{dE}{d\eta}$. To determine the optimal CAP strength (η_{opt}), one can employ the condition $\eta \, \frac{dE}{d\eta} =$ min. One can also determine the optimal CAP strength by graphically analyzing the η-trajectory, as at the optimum, the resonance is associated with a stabilization point or cusp. To optimize the box size, several calculations are performed at the optimal η value. The chosen optimized box size is the one where the resonance energies show minimal variation. The CAP approach has proven to be effective in studying atomic and molecular resonances and has been incorporated into various electronic structure methods[72, 73, 74, 75, 76, 77, 78, 79, 80].

Another type of method involves the use of bound state calculations, i.e., conventional Hermitian quantum mechanics. This includes artificially binding an extra electron, which can be accomplished by using a compact basis set or introducing a potential wall[81, 82] to capture the electron inside. Additionally, it also includes stabilization methods and extrapolation methods are used to describe the metastable states.

1.2.5 Conventional Stabilization Methods

In conventional stabilization methods (SMs)[83, 84, 85, 86, 87, 88, 89], the procedure involves computing the energies of several states in a specific range where a metastable state is anticipated. The presence of a potential metastable state is identified by the fact that a small change in the radial extent of diffuse functions in the basis set has a greater impact on the continuum states compared to the metastable state's energy, which remains relatively constant over a wide range of scaled basis sets. In the adiabatic picture, a series of avoided crossings is generated by the stabilization graph, and the resonance parameters can be derived from the avoided crossings in the plots of eigenvalues as functions of the scaling parameter.

1.2.6 Extrapolation Methods

In extrapolation methods[90, 91, 92, 93, 94, 95, 96], a potential is added to the Hamiltonian of the electron-attached species that varies with an adjustable parameter. This potential helps in differentiating the stabilization of electrons in the core and valence regions from the stabilization of electrons that are further away. Eventually, at a specific value of the parameter, the electron-attached species become electronically stable, forming a bound anion by placing the extra electron in a valence state rather than in a diffuse state. After this point, conventional electronic structure tools can be used to calculate the electronic energy of this artificially stabilized species, provided that there is a theoretical framework to extrapolate the electronic energy from values of the adjustable parameter, Z, where the species is bound, to regions of Z where it is metastable, and all the way to $Z = 0$. In another method, called the charge stabilization method introduced by Nestmann and Peyerimhoff[90], the unstable anion is converted to a bound anion by adjusting the nuclear charge of the nuclei of interest. The data for bound anions at several nuclear charge values is then used to extrapolate to the anionic state where the anion is no longer bound. So far, this method has been applied to energies calculated with unrestricted Hartree-Fock (UHF)[97], DFT[98, 99, 100], second-order Moller-Plesset perturbation theory (MP2), fourth-order Moller-Plesset perturbation theory

(MP4)[97, 98, 101, 102], coupled-cluster singles and doubles with different perturbative triples corrections [CCSD(T)][97, 101, 103], and multi-reference configuration interaction (MRCI)[103].

1.3 Methodology

The earlier section discusses the various methods developed by researchers to study metastable states. The following section focuses on the methodologies implemented in this thesis for examining these metastable states in detail. It includes a brief description of the Hartree-Fock method, the nuclear charge stabilization method introduced by Nestmann and Peyerimhoff, and an innovative approach for implementing the nuclear charge stabilization method at the SCF level using Parametric Equations of Motion (PEM). Additionally, an alternative approach for implementing CAP at the SCF level using PEM is also discussed. Finally, a brief description is provided for Second-order dilated electron propagator(SODEP) approach.

1.3.1 Hartree-Fock

The Hartree-Fock (HF) method is a self consistent field method that is used for the determination of the wave function and the energy of a quantum many-body system with successive iterations. The problem of determining the Hartree-Fock molecular orbitals and orbital energies involve solving the Roothaan equation

$$FC = SC\epsilon \tag{1.12}$$

where F is the Fock matrix, ϵ is a diagonal matrix of the orbital energies and eigenvector (i.e., C) is the matrix of coefficients describing the molecular orbitals. Following the conventional SCF, after diagonalizing the F' , the orbital energies(ϵ) and C' is obtained,

$$F'C' = C'\epsilon, \tag{1.13}$$

where F' is defined conventionally as

$$F' = X^T F X. \tag{1.14}$$

X is canonical orthogonalizing transformation matrix[104] which is defined as

$$X = Us^{-\frac{1}{2}} \tag{1.15}$$

where U is the unitary matrix that performs the diagonalization of the overlap matrix S, and s = U†SU. The matrix elements corresponding to the Fock matrix are;

$$F_{mn} = T_{mn} + V_{mn}^{nucleus} + \sum_{\lambda\sigma} P_{\lambda\sigma}[(mn|\sigma\lambda) - \frac{1}{2}(m\lambda|\sigma n)] \tag{1.16}$$

where

$$P_{\lambda\sigma} = \sum_{a}^{occ} C_{\lambda a} C_{\sigma a}^{\star}, \tag{1.17}$$

and T_{mn} is the matrix elements of kinetic energy whereas $V_{mn}^{nucleus}$ is matrix elements of the electron-nucleus attraction term. Closed-shell Hartree-Fock (HF) is utilized when applying Koopman's theorem to describe the resonance state. Conversely, Unrestricted Hartree-Fock (UHF) is employed when the resonance is represented as the difference between the total anionic and neutral species. In the case of the UHF equations, the α and β-spin orbitals are similar to those in the closed-shell equations.

1.3.2 Nuclear Charge Stabilization Method

The method applied in this work is the nuclear charge stabilization[90] method as introduced by Nestmann and Peyerimhoff. In this method, some atomic nuclei are given additional charges to create a potential that stabilizes certain regions of space. This potential is generated by adjusting the nuclear charges in the molecule by a factor of z to nuclei of interest. The Hamiltonian then takes the following form

$$H_z = T + V_{en}(R) + V_{ee} + zU_{en}(R) \tag{1.18}$$

where U_{en} is the Coulomb attraction term corresponding to those nuclei where the scaling of nuclear charge is to be performed. In quantum-chemistry codes, it can be applied by modifying the value of the nuclear charges for the evaluation of the Coulomb attraction term.

Throughout, scaling of nuclear charge by a factor of z is done in Fock matrix and corresponding Fock matrix elements are

$$F_{mn} = T_{mn} + V_{mn}^{nucleus} + zU_{mn}^{nucleus} + \sum_{\lambda\sigma} P_{\lambda\sigma}[(mn|\sigma\lambda) - \frac{1}{2}(m\lambda|\sigma n)] \tag{1.19}$$

where

$$P_{\lambda\sigma} = \sum_{a}^{occ} C_{\lambda a} C_{\sigma a}^{\star}, \tag{1.20}$$

and

T_{mn} is the matrix elements of kinetic energy whereas $V_{mn}^{nucleus}$ and $U_{mn}^{nucleus}$ are matrix elements of the electron-nucleus attraction corresponds to all nuclei and to the nuclei where scaling is to be performed, respectively.

1.3.3 Implementation of Nuclear Charge Stabilization Method via Parametric Equations of Motion

One way to solve the eigenvalue problem with an adjustable parameter is by diagonalizing the Fock matrix obtained at each value of that parameter. Another effective method is to use the Parametric Equations of Motion (PEM). PEM was proposed by Rabitz and co-workers [105] and successfully applied to the family of Schrodinger equations with one or more continuous parameters present in the Hamiltonian. In this method, the Schrodinger equation was solved explicitly only once at initial parameter values and the solutions at other parameter values are obtained by integrating a set of ordinary differential equations through the parameter space of the Hamiltonian. These differential equations are known as PEM, which can explore the energy eigenvalues and eigenstates of quantum systems. These types of equations were also applied in the field of quantum chaos[106, 107, 108]. Later, Gross et al.[109] used PEM to obtain quantum dynamics of molecular systems under the influence of strong periodic fields of the form $A cos \omega t$ over a wide range of field amplitudes and frequencies by solving the time-dependent Schrodinger equation (TDSE) once. This method utilizes Floquet's theory as well and integrates through amplitude or frequency space using the PEM for quasienergies and Floquet eigenvectors. Further, Gupta et al. applied PEM to obtain the 3D plots of population dynamics as a function of frequency and phase (or amplitude and phase)[110] and to study the laser-induced multiphoton dissociation dynamics of H_2^+ as a function of the laser field amplitude[111] and frequency[112]. The PEM method in conjunction with modified smooth exterior scaling method[41] was also used to study the resonance coalescence in H_2^+ [113]. In the current study, the nuclear charge stabilization technique has been implemented in conjunction with the PEM method. The procedure how PEM is implemented is described below in details.

The F' in Eq. (1.13) depends on z as

$$F' = X^T(F^0 + zU^{nucleus})X \tag{1.21}$$

$$F' = X^T F^0 X + zX^T U^{nucleus} X \tag{1.22}$$

where $U^{nucleus}$ is z independent

and the F^0 is defined as

$$F^0_{mn} = H^{core}_{mn} + \sum_a^{occ} \sum_{\lambda\sigma} P_{\lambda\sigma}[2(mn|\sigma\lambda) - (m\lambda|\sigma n)] \tag{1.23}$$

where

$$H^{core}_{mn} = T_{mn} + V^{nucleus}_{mn} \tag{1.24}$$

Following the derivation of Rabitz and co-workers[105] evolution of eigen values (ϵ) and eigen vectors (C') as a function of the linear perturbation parameter z is given as

$$\frac{\partial \epsilon_n}{\partial z} = (C'_n)^T \frac{\partial F'}{\partial z} C'_n \tag{1.25}$$

$$\frac{\partial C'_i}{\partial z} = -\sum_{j\neq i} \frac{(C'_j)^T \left(\frac{\partial F'}{\partial z}\right) C'_i}{\epsilon_j - \epsilon_i} C'_j \tag{1.26}$$

$$\frac{\partial F'}{\partial z} = X^T \frac{\partial (F^0 + zU^{nucleus})}{\partial z} X = X^T \frac{\partial F^0}{\partial z} X + X^T U^{nucleus} X \tag{1.27}$$

where matrix elements

$$\left(\frac{\partial F^0}{\partial z}\right)_{mn} = \frac{\partial F^0_{mn}}{\partial z} = \sum_{\lambda}\sum_{\sigma} \frac{\partial P_{\lambda\sigma}}{\partial z}[(mn|\sigma\lambda) - \frac{1}{2}(m\lambda|\sigma n)] \tag{1.28}$$

The PEM are integrated numerically using Euler's method. Before integrating the PEM equations, it is important to have initial conditions to proceed further.The initial conditions for orbital energies ϵ and eigen vector C_i are obtained from SCF solution at an initial nuclear charge of dz value. But there is a problem while solving these equations as $\frac{\partial P}{\partial z}$ is not known initially. To have appropriate initial condition for $\frac{\partial P}{\partial z}$, two SCF calculations were performed at z and $z + dz$ in order to have $P(z)$ and $P(z + dz)$. $\frac{\partial P}{\partial z}$ at $z + dz$ is calculated using $P(z + dz)$ and $P(z)$

$$\frac{\partial P}{\partial z} = \frac{P(z + dz) - P(z)}{dz}. \tag{1.29}$$

After solving PEM, $P(z + 2dz)$ is obtained and now using 3-point finite difference method formula, $\frac{\partial P}{\partial z}$ at $z + dz$ is evaluated and the PEM calculation is performed again. This step is performed repeatedly until convergence for $P(z+2dz)$ is obtained. The procedure is then carried out for each z value.

1.3.4 Parametric Equations of Motion-Complex Absorbing Potential (PEM-CAP) Approach

In PEM-CAP approach, CAP-matrix (W_{mn}) is added in the Fock matrix and corresponding Fock matrix elements are

$$F_{mn} = T_{mn} + V^{nucleus}_{mn} + \eta(-iW_{mn}) + \sum_{\lambda\sigma} P_{\lambda\sigma}[(mn|\sigma\lambda) - \frac{1}{2}(m\lambda|\sigma n)] \tag{1.30}$$

where

$$P_{\lambda\sigma} = \sum_{a}^{occ} C_{\lambda a} C^{\star}_{\sigma a}, \tag{1.31}$$

and

$$W_{mn} = \langle m|W|n\rangle \tag{1.32}$$

The transformed Fock matrix F' in orthogonalized basis depends on η as

$$F' = X^T F X = X^T(F^0 + \eta(-iW))X \tag{1.33}$$

$$F' = X^T F^0 X + \eta X^T(-iW)X \tag{1.34}$$

Similarly, as described in previous section, the evolution of eigen values (ϵ) and eigen vectors (C) as a function of the linear perturbation parameter η is given as

$$\frac{\partial \epsilon_n}{\partial \eta} = (C'_n)^T \frac{\partial F'}{\partial \eta} C'_n \tag{1.35}$$

$$\frac{\partial C'_i}{\partial \eta} = -\sum_{j\neq i} \frac{(C'_j)^T \left(\frac{\partial F'}{\partial \eta}\right) C'_i}{\epsilon_j - \epsilon_i} C'_j \tag{1.36}$$

$$\frac{\partial F'}{\partial \eta} = X^T \frac{\partial (F^0 + \eta(-iW))}{\partial \eta} X = X^T \frac{\partial F^0}{\partial \eta} X + X^T(-iW)X \tag{1.37}$$

where matrix elements

$$\left(\frac{\partial F^0}{\partial \eta}\right)_{mn} = \frac{\partial F^0_{mn}}{\partial \eta} = \sum_{\lambda}\sum_{\sigma} \frac{\partial P_{\lambda\sigma}}{\partial \eta}[(mn|\sigma\lambda) - \frac{1}{2}(m\lambda|\sigma n)] \tag{1.38}$$

1.3.5 Second-order Dilated Electron Propagator (SoDEP) approach

The electron propagator theory is considered an efficient method in improving the electron affinities and ionization potentials that are calculated from the bivariational SCF level. These improvements can be done by introducing an effective potential, called self-energy, which was formulated by Dyson[104]. The Dyson equation for dilated electron propagator $\mathbf{G}$ can be written as[56]

$$\mathbf{G}^{-1}(\eta, E) = \mathbf{G}_0^{-1}(\eta, E) + \Sigma(\eta, E) \tag{1.39}$$

where $\mathbf{G}_0(\eta, E)$ is known as the zeroth order dilated electron propagator and is a matrix of the electron propagator of uncorrelated electron motion and $\Sigma(\eta, E)$ is defined as

$$\Sigma(\eta, E) = \Sigma^{(2)}(\eta, E) + \Sigma^{(3)}(\eta, E) + ... \tag{1.40}$$

$\Sigma(\eta, E)$ is the matrix representation of the exact self-energy in the basis of spin orbitals obtained from bivariational SCF solution, which is the sum of different orders such as second order, $\Sigma^{(2)}(\eta, E)$, and third order, $\Sigma^{(3)}(\eta, E)$. This self-energy matrix contains the relaxation and correlation effects.

In particular, the elements of the second order self-energy matrix are given as follow[104, 114]

$$\Sigma_{ij}^{(2)}(\eta, E) = \frac{1}{2}\sum_{ars} \frac{<rs||ia><ja||rs>}{E + \epsilon_a - \epsilon_r - \epsilon_s} + \frac{1}{2}\sum_{abr} \frac{<ab||ir><jr||ab>}{E + \epsilon_r - \epsilon_a - \epsilon_b} \tag{1.41}$$

where the indices a,b,... represent occupied spin orbitals, r,s,... represent unoccupied spin orbitals and i,j,... represent unspecified orbitals and the antisymmetric two-electron integral is given by

$$<ij||kl> = \eta^{-1} \int \psi_i(1)\psi_j(2)\frac{(1 - P_{12})}{r_{12}}\psi_k(1)\psi_l(2)dx_1dx_2. \tag{1.42}$$

1.4 Motivation of the Thesis

The main objective of this thesis is to provide an accurate approach for obtaining resonance energies in the most precise manner. The PEM approach offers several advantages and more clearer picture for understanding the basics of electronic resonances. The key outcomes derived from the PEM approach are as follows:

1. The identification of the true Lowest Unoccupied Molecular Orbital (LUMO) is a crucial step in the study of electronic resonance. The nuclear charge stabilization method proves to be a valuable tool for this identification. However, generating a charge stabilization plot can be quite challenging, as it requires careful tracking of every orbital. In cases of avoided crossings, producing the charge stabilization plot becomes nearly impossible. To address these difficulties, the use of parametric equations of motion offers a solution for generating charge stabilization plots to identify the true LUMO. This approach also helps manage avoided crossings involving states of the same symmetry. The implementation of the nuclear charge stabilization method, in conjunction with the parametric equations of motion, allows for the accurate identification of the true LUMO, even when using heavily diffuse basis sets (see Chapter 2).

2. Obtaining the SCF solution for metastable anions is nearly impossible because using a heavily diffuse basis set often leads to variational collapse, resulting in a solution that corresponds to a neutral atom and a free electron. However, implementing the nuclear charge stabilization method, along with the parametric equations of motion, proves to be an effective approach to avoid variational collapse at the SCF level when studying metastable anions (see Chapter 3).

3. PEM offer an alternative method for implementing the CAP at the SCF level. This approach is extremely fast compared to the diagonalization method and also helps in keeping track of each orbital (see Chapter 4).

4. An effort has also been made to obtain the SCF solution for metastable anions by eliminating the pseudo-continuum states. To obtain the η trajectory via this approach, it is crucial to keep track of the orbitals; otherwise, it would require an enormous amount of human effort. To effectively keep the orbitals at each η, the PEM-CAP approach appears to be a highly effective method (see Chapter 5).

5. Since the CAP is an artificial potential, a finite value for the CAP strength parameter, denoted as η, is necessary in order to determine the resonance energies. This finite value of η introduces perturbations within the system,

resulting in affecting the accuracy of the resonance energy values. The application of the PEM-CAP approach proves to be highly effective for calculating resonances in the physical limit where η equals 0 for the CAP (see Chapter 6).

Chapter 2

Precise Identification of the Lowest Unoccupied Molecular Orbital using the Parametric Equations of Motion

2.1 Introduction

For neutral molecules, defining virtual orbitals obtained from SCF calculation is not straightforward and depends heavily on the basis sets used. For instance, when using a highly diffuse basis set, the energy for the lowest empty molecular orbital (MO) will be almost zero, making it unreliable. In Post-SCF[115, 116, 117, 118] theories such as configuration interaction (CI), coupled cluster (CC), and perturbation theory, electron correlation effects beyond the mean-field approximation are taken into account to provide more accurate descriptions of molecular systems. Among these theories, the LUMO plays a crucial role in theoretical analyses and practical applications.

Techniques such as time-dependent density functional theory (TDDFT) and equation-of-motion coupled cluster (EOM-CC) exploit the LUMO to compute electronic transition energies[119, 120] and intensities, enabling accurate simulations of various spectroscopic experiments, including UV-Vis absorption, fluorescence, and etc. Identifying transitions between MOs is usually done by visually inspecting their shapes and characteristics. However, this method can be problematic because the orbital character may not be well-defined, making it challenging to assign a specific transition. Furthermore, characterizing a transition based on orbital label can be difficult due to the strong dependence of virtual orbitals on the basis set and exchange-correlation functional. Therefore, relying solely on orbital character may not always result in accurate or reliable assignments.

Additionally, the LUMO plays a crucial role in analyzing molecular reactivity and chemical bonding, which are key concepts of theoretical chemistry. It is a key factor in facilitating the identification of electrophilic and nucleophilic sites within a molecule, as well as the frontier orbitals[121, 122] that govern chemical reactions. By providing valuable insights into reaction mechanisms, transition states, and molecular interactions, the identification of LUMO helps researchers to design catalysts, drugs, and functional materials with specific reactivity and selectivity profiles.

Furthermore, in the study of unstable anions[123, 124, 125, 126, 127, 128, 42, 43], LUMOs are very important as they are only the states that are going to be filled by an electron. Hence their identification becomes very much important otherwise system will converges to neutral molecule and a free electron.

Several works have been done so far to deal with the virtual orbitals[129, 130, 131]. An article by Krylov[132] from 2020 describes advanced methods for obtaining the $\pi^\star$ electron-attached states and $\pi^\star$ excited states. Other researchers[133, 134, 135] have also described how to extract various $\pi^\star$, including localized $\pi^\star$ orbitals and those used for inter-fragment interaction energy calculations, from electronic structure calculations. In addition, Jordan et al.[136] and Chen et al.[137] used the stabilization method. The main idea was that temporary anion states have a localized wavefunction in the molecular region, and a small change in the radial extent of the most diffuse functions in the bases set affects the continuum energies more than the energies corresponding to localized wavefunction of temporary anion. The stabilization plots are calculated as a function of the exponent, and the MO energy corresponding to the electron-attached state is calculated as the mean value of eigenvalues at the avoided crossing. However, here, the main goal is the identification of MO itself, which can be used for post-SCF calculation to incorporate the correlation energy for more accurate results.

Here, the charge stabilization method of Nestmann and Peyerimhoff[90] is applied, which involves the introduction of additional charges to specific atomic nuclei, ultimately creating a potential that effectively stabilizes the corresponding LUMO, keeping the continuum states less affected. In 2022, Simon[138] published an article discussing the search for antibonding valence virtual orbitals within continuum states. When conducting calculations that use a stabilizing electronic potential to stabilize electronically metastable states, two routes are typically used. The first method involves adding excess charges to some atomic nuclei, producing a potential that stabilizes these regions of space. The second method involves adding a dielectric continuum solvation potential to generate stabilization. In the latter method, the electronic energies of the states are obtained for a range of dielectric constant (ϵ) values for which the anion is stable by employing the polarized continuum solvation model (PCM)[139, 140, 141] within SCF treatment. The nuclear charge stabilization method has also been applied to unstable anions where extrapolation[92, 94, 89, 96] of bound state data is required.

In the current study, the nuclear charge stabilization technique has been implemented in conjunction with the PEM approach. This approach aims to identify the desired LUMO of the parent molecule effectively. The efficiency of the PEM lies in the fact that the variation of a specific state with respect to variation of nuclear charge parameter can be easily traced whereas in case of diagonalization, it will be difficult to connect a state at two different parameter values when lots of states are close to each other and even crossing each other. It would be impossible to recognize if there was an avoided crossing in case of diagonalization method. Therefore, PEM is much more useful as it keeps track of the order of orbitals and orbital energies because the line number of a particular state remains fixed, hence providing a line plot, whereas, in the matrix diagonalization, it is rearranged every time and getting data points on the graph without knowing which two dots to connect.

In this chapter, the virtual orbitals of neutral N_2, C_2H_4 and C_2H_2 molecules are examined by applying the nuclear charge stabilization method in conjunction with PEM method, and the LUMOs have been identified. However, identification of the LUMO can be challenging when using a diffuse basis set or if the SCF solution includes molecular orbitals with the same symmetry as the LUMO. This results in multiple avoided crossings, making it difficult to identify the LUMO using the current form of PEM. Avoided crossings can cause an exchange of orbital character, and tracking the stabilization curve can result in a state with the same symmetry as the LUMO, making it unsuitable for LUMO identification. In such cases, further analysis and investigation are necessary to prevent the stabilization of states involved in avoided crossings. The identification of LUMO in such cases is achieved by modifying the PEM preventing the stabilization of such states in charge stabilization curve, which is detailed in this chapter for neutral C_2H_4 and C_2H_2 molecules for heavily diffused basis sets.

2.2 Results and Discussion

The results and discussion are structured to first apply the nuclear charge stabilization method in conjunction with the PEM, using predefined basis sets without augmentation. This approach aims to observe and visualize the importance of accurately identifying the true LUMO even when using these predefined basis sets including compact basis sets for the N_2, C_2H_4, and C_2H_2 molecules. Subsequently, the effect of adding diffuse basis functions on the position and energy of the true LUMO is also examined and discussed specifically for the C_2H_4 and C_2H_2 molecules.

2.2.1 Pre-defined basis sets without extra augmentations

The HF orbital energies were obtained from calculations performed using 6-311G, cc-pVTZ, aug-cc-pVDZ, and aug-cc-pVTZ basis sets for N_2, C_2H_4 and C_2H_2 molecules. All quantum chemistry calculations were performed using the Molgw[143] package. The cube file generated from Molgw was used to plot the orbitals using the Gaussian16[144] package. In all orbital plots generated for the 6-311G and cc-pVTZ basis sets, the iso value has been set to 0.05. However, for the aug-cc-pVDZ and aug-cc-pVTZ basis sets, the iso value has been set to 0.05 for the identified LUMO state and 0.002 for other states as nothing was observed at 0.05. The iso value for other states was chosen low as they are continuum states in diffuse basis set. Same isovalue has been used for all the molecules unless explicitly stated.

2.2.1.1 Identification of $\pi^\star$ orbital of neutral N_2 molecule

The N_2 molecule is placed along the x-axis symmetrical to the origin considering the bond length of 1.09 Å. In order to visualize the behaviour of virtual orbitals, few virtual orbitals were plotted corresponding to different basis sets (see figures 2.1-2.4). Observing the orbital plots, it becomes apparent that the LUMO orbital does not closely resemble the antibonding $\pi^\star$ orbital. Instead, the LUMO+N orbital (where N is different for different basis sets) as shown in the Figure 2.1-2.4), appears to be a more suitable candidate for the $\pi^\star$ orbital. However, it is important to note that this identification is merely a reasonable approximation and not an exact representation. From figures 2.3 and 2.4 , it is very evident that LUMO is not the $\pi^\star$ antibonding orbital instead LUMO+1 and LUMO+4 corresponds to actual $\pi^\star$ antibonding orbital in the case of aug-cc-pVDZ and aug-cc-pVTZ basis sets respectively while in the case of 6-311G and cc-pVTZ basis sets LUMO (i.e. figures 2.1 and 2.2) corresponds to the actual $\pi^\star$ antibonding orbital but there is significant orbital energy difference from earlier basis sets used.

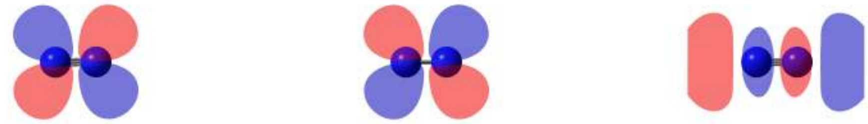

(a) LUMO (b) LUMO+1 (c) LUMO+2

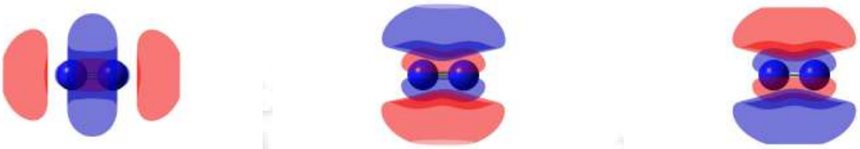

(d) LUMO+3 (e) LUMO+4 (f) LUMO+5

FIGURE 2.1: Plots of few virtual orbitals of neutral N_2 molecule for 6-311G basis set. The degenerate states LUMO and LUMO+1 are clearly identified as $\pi^\star$ antibonding orbitals.

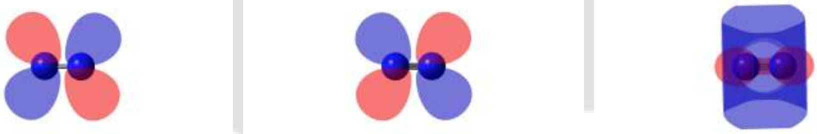

(a) LUMO (b) LUMO+1 (c) LUMO+2

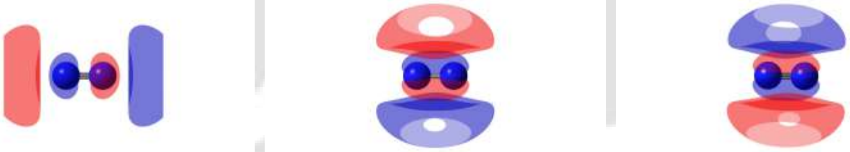

(d) LUMO+3 (e) LUMO+4 (f) LUMO+5

FIGURE 2.2: Plots of few virtual orbitals of neutral N_2 molecule for cc-pVTZ basis set. The degenerate states LUMO and LUMO+1 are clearly identified as $\pi^\star$ antibonding orbitals.

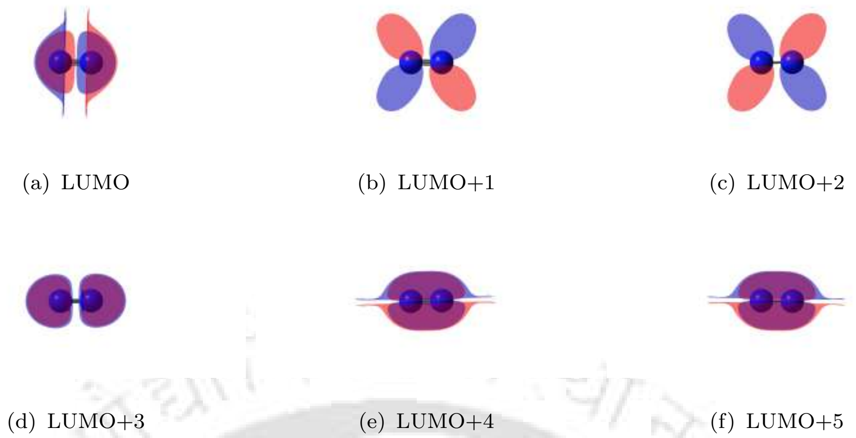
(a) LUMO (b) LUMO+1 (c) LUMO+2

(d) LUMO+3 (e) LUMO+4 (f) LUMO+5

FIGURE 2.3: Plots of few virtual orbitals of neutral N_2 molecule for aug-cc-pVDZ basis set. The degenerate states LUMO+1 and LUMO+2 are clearly identified as $\pi^{\star}$ antibonding orbitals.

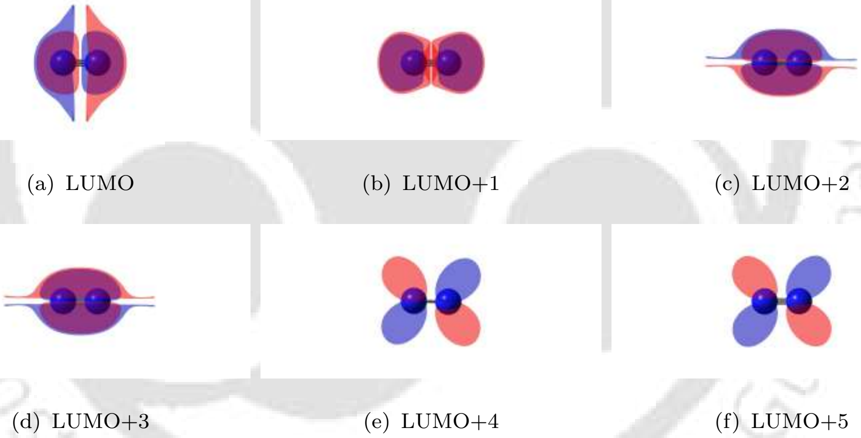
(a) LUMO (b) LUMO+1 (c) LUMO+2

(d) LUMO+3 (e) LUMO+4 (f) LUMO+5

FIGURE 2.4: Plots of few virtual orbitals of neutral N_2 molecule for aug-cc-pVTZ basis set. The degenerate states LUMO+4 and LUMO+5 are clearly identified as $\pi^{\star}$ antibonding orbitals.

It is of utmost significance to acquire a comprehensive understanding of the nature of LUMO to LUMO+N-1 orbitals and the intricate manner in which they contribute to the complexity of the calculations. Since our HF calculation was executed using a finite basis set, these orbitals can be classified as pseudo-continuum states. If these orbitals were to be incorporated into electron-attached states, the consequence would be that the electron would not be bound in the valence framework of the molecule. Instead, the additional electron would remain unbound and exhibit scattering phenomena with the neutral molecule.

To determine the precise location of the LUMO, it is necessary to perform an HF calculation on a neutral molecule with varying nuclear charge along with PEM. The PEM method is particularly advantageous as it keeps track of line number of each orbital energy varying with the value of additional nuclear charge z. In contrast, diagonalization tends to result in rearranging orbital energies, making it less suitable for this purpose. Therefore, in the comparison plot (in fig 2.5), diagonalization results have been depicted as green dots since it is challenging to generate a line plot due to the rearrangement in orbital energies. This could be understood as, at z = 0, the states are ordered according to their orbital energy obtained from the SCF solution. In PEM, the states will remain arranged according to their orbital character. For example, the 9^{th}(i.e., LUMO+1) state in aug-cc-pVDZ has $\pi^\star$ character; it will remain the 9^{th} state, at all z values, resulting in a line plot. However, in the case of diagonalization, 9^{th} state at z = 0 becomes 8^{th} state at higher z values due to rearrangement based on energy. Consequently, generating a line plot becomes challenging. As can be seen for the even more diffuse basis set, the state may undergo multiple crossings, thus generating the line plot even more challenging. From figure 2.5, it is clearly seen that the orbital energies obtained from PEM and diagonalization via SCF at different values of nuclear charge value for different basis sets are in excellent agreement. The results for diagonalization and PEM are indistinguishable when plotted, thus reinforcing the method's reliability and accuracy when evaluating the impact of additional z values on the system. The computational time was assessed for both the PEM and diagonalization results. Upon comparison, the computational time required for obtaining results through the PEM method was found to be significantly lower than that for diagonalization. Specifically, the PEM results were determined to be approximately ten times faster than the results obtained through diagonalization. This indicates a substantial efficiency advantage in favor of the PEM method in terms of computational time.

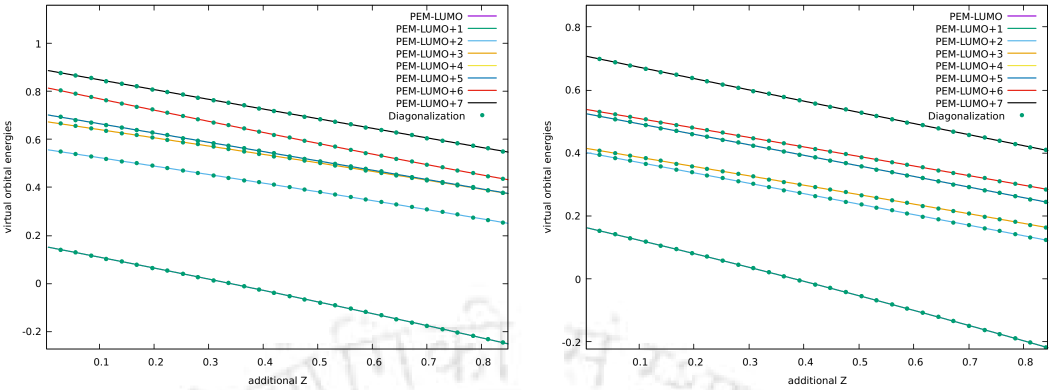

(a) 6-311G (b) cc-pVTZ

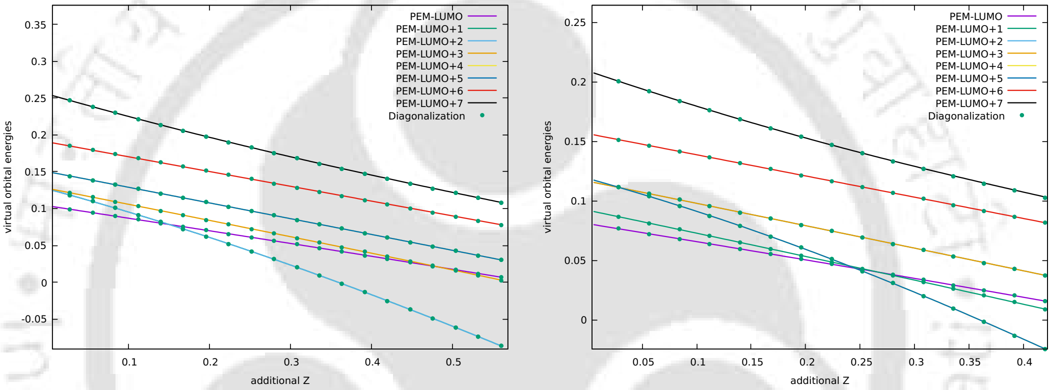

(c) aug-cc-pVDZ (d) aug-cc-pVTZ

FIGURE 2.5: Plot of the few lowest virtual orbital energies in Hartree (on y-axis) as function of additional nuclear charge (on x-axis) of neutral N_2 molecule for different basis sets. The degenerate states LUMO and LUMO+1 are getting more stabilized for 6-311G, cc-pVTZ basis sets, while degenerate states(i.e., LUMO+1 and LUMO+2) and degenerate states (i.e., LUMO+4 and LUMO+5) are getting stabilized in the case of aug-cc-pVDZ and aug-cc-pVTZ basis sets respectively as the nuclear charge increases. The PEM solution agrees well with diagonalization results (represented by green dots).

In figure 2.5, it can also be observed that the energy of the LUMO+1 and LUMO+4 orbitals in the case of aug-cc-pVDZ and aug-cc-pVTZ basis sets, respectively, experience a greater degree of stabilization as a result of variations in z compared to the energies of the remaining virtual orbitals. The reason behind the enhanced stabilization of the LUMO+N orbital, in comparison to the other virtual orbitals, lies in the fact that the $\pi^\star$ antibonding is more localized in close proximity to the two N nuclei, as opposed to the other virtual orbitals which are situated at a greater distance from the nuclei. This localization effect contributes significantly to the overall stabilization of the LUMO+N orbital, thus explaining its comparatively stronger stabilization as a function of z.

In order to compare orbitals and orbital energies, basis sets are selected in a way that allows for a comparison between compact and diffuse basis sets. The LUMO obtained from compact basis sets may appear to be decent, but this is not always the case. Additionally, the LUMO orbital energies differ between compact and diffuse basis sets, which can be confirmed by referring to table 2.1.

Table 2.1: Tabular data for orbital energies(in Hartree) of neutral N_2 molecule for different basis sets. The identified LUMO energies are marked in bold.

6-311G	cc-pVTZ	aug-cc-pVDZ	aug-cc-pVTZ
-15.7066	-15.6801	-15.6941	-15.6813
-15.7029	-15.6764	-15.6905	-15.6776
-1.5299	-1.4763	-1.4850	-1.4776
-0.7728	-0.7758	-0.7786	-0.7768
-0.6306	-0.6338	-0.6346	-0.6350
-0.6255	-0.6162	-0.6185	-0.6175
-0.6255	-0.6162	-0.6185	-0.6175
0.1532	**0.1641**	0.1038	0.0808
0.1532	**0.1641**	**0.1267**	0.0921
0.5585	0.4025	**0.1267**	0.1165
0.6747	0.4156	0.1274	0.1165
0.7039	0.5258	0.1501	**0.1188**
0.7039	0.5258	0.1501	**0.1188**
0.8166	0.5393	0.1905	0.1564
0.8892	0.7087	0.2555	0.2091
0.8892	0.7087	0.2555	0.2091

2.2.1.2 Identification of $\pi^\star$ orbital of neutral C_2H_4 and neutral C_2H_2 molecule

The equilibrium geometry structure of the neutral C_2H_4 molecule features a C–C bond distance of 1.339 $\AA$ and a C–H bond distance of 1.086 $\AA$ and the bond angle for $\angle HCH$ is 117.6°, and for $\angle HCC$ is 121.2°, respectively, while the neutral C_2H_2 molecule has a C–C bond distance of 1.203 $\AA$ and a C–H bond distance of 1.063 $\AA$. Corresponding virtual orbitals to different basis sets were plotted in figures 2.6-2.9 for neutral C_2H_4 and in figures 2.10-2.13 for neutral C_2H_4 , and it is clearly seen that the lowest unoccupied orbitals don't resemble the shape of $\pi^\star$ antibonding. Upon observation of the orbital plots for neutral C_2H_4, it becomes apparent that in the case of 6-311G and cc-pVTZ basis sets, LUMO orbital resembles antibonding $\pi^\star$ orbital while in the case of aug-cc-pVDZ and aug-cc-pVTZ basis sets LUMO does not closely resemble the antibonding $\pi^\star$ orbital. Instead, the LUMO+4 (for aug-cc-pVDZ and aug-cc-pVTZ basis sets) orbital appears to be a more suitable candidate for the $\pi^\star$ orbital. Similarly upon observation of the orbital plots for neutral C_2H_2, the LUMO+3 using 6-311G, cc-pVTZ and aug-cc-pVDZ basis sets while LUMO+4 in case of aug-cc-pVTZ orbital appear to be a more suitable candidate for the $\pi^\star$ orbital. So, it is really important to identify the true LUMO so that the true LUMO is taking part in calculations to get precise and expected results.

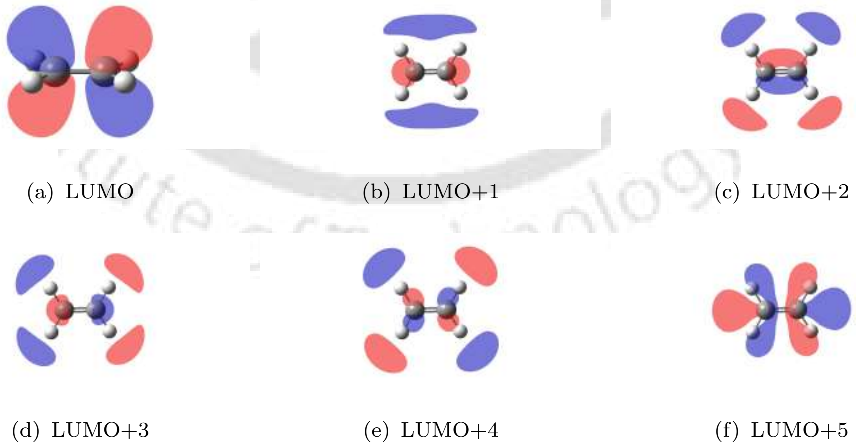
(a) LUMO (b) LUMO+1 (c) LUMO+2
(d) LUMO+3 (e) LUMO+4 (f) LUMO+5

FIGURE 2.6: Plots of few virtual orbitals of neutral C_2H_4 molecule for 6-311G basis set. LUMO is perfect candidate for $\pi^\star$ antibonding orbital.

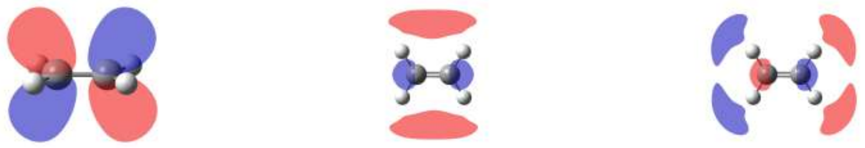

(a) LUMO (b) LUMO+1 (c) LUMO+2

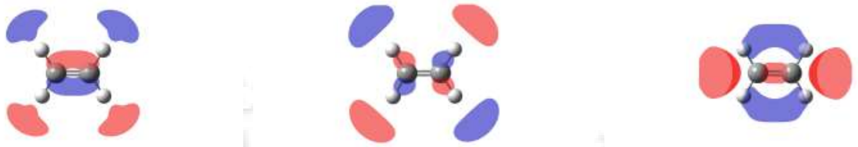

(d) LUMO+3 (e) LUMO+4 (f) LUMO+5

FIGURE 2.7: Plots of few virtual orbitals of neutral C_2H_4 molecule for cc-pVTZ basis set. LUMO is perfect candidate for $\pi^\star$ antibonding orbital.

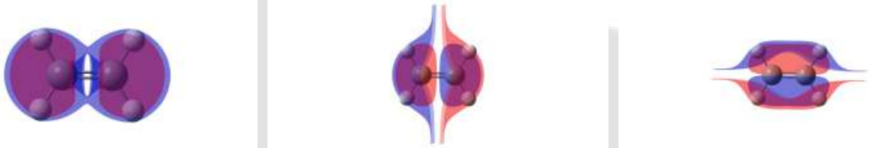

(a) LUMO (b) LUMO+1 (c) LUMO+2

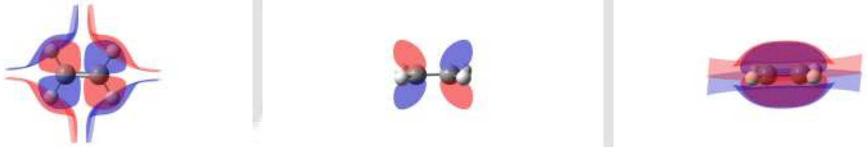

(d) LUMO+3 (e) LUMO+4 (f) LUMO+5

FIGURE 2.8: Plots of few virtual orbitals of neutral C_2H_4 molecule for aug-cc-pVDZ basis set. LUMO+4 is perfect candidate for $\pi^\star$ antibonding orbital.

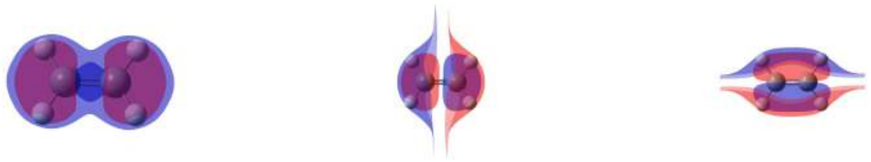

(a) LUMO (b) LUMO+1 (c) LUMO+2

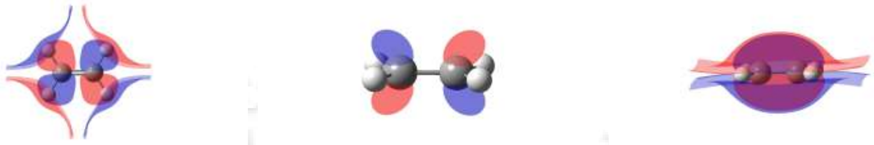

(d) LUMO+3 (e) LUMO+4 (f) LUMO+5

FIGURE 2.9: Plots of few virtual orbitals of neutral C_2H_4 molecule for aug-cc-pVTZ basis set. LUMO+4 is perfect candidate for $\pi^\star$ antibonding orbital.

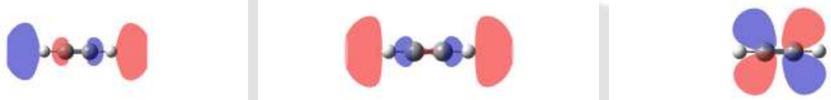

(a) LUMO (b) LUMO+1 (c) LUMO+2

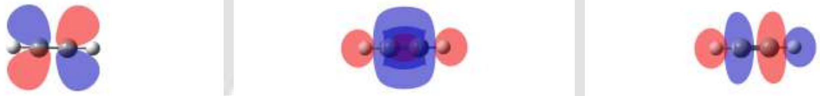

(d) LUMO+3 (e) LUMO+4 (f) LUMO+5

FIGURE 2.10: Plots of few virtual orbitals of neutral C_2H_2 molecule for 6-311G basis set. The degenerate states LUMO+2 and LUMO+3 are clearly identified as $\pi^\star$ antibonding orbitals.

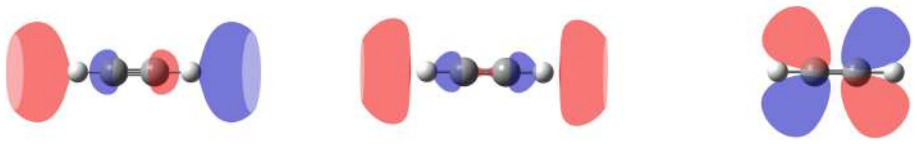

(a) LUMO (b) LUMO+1 (c) LUMO+2

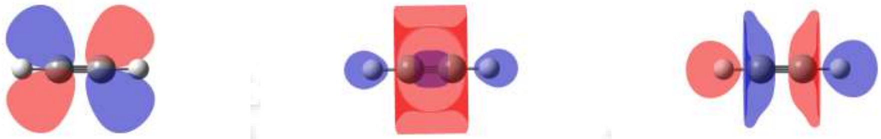

(d) LUMO+3 (e) LUMO+4 (f) LUMO+5

FIGURE 2.11: Plots of few virtual orbitals of neutral C_2H_2 molecule for cc-pVTZ basis set. The degenerate states LUMO+2 and LUMO+3 are clearly identified as $\pi^\star$ antibonding orbitals.

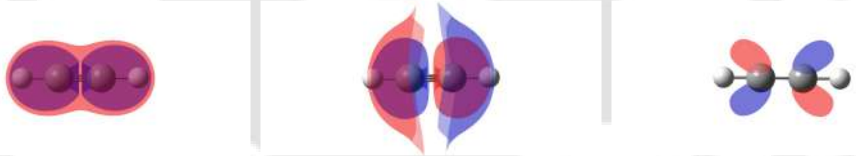

(a) LUMO (b) LUMO+1 (c) LUMO+2

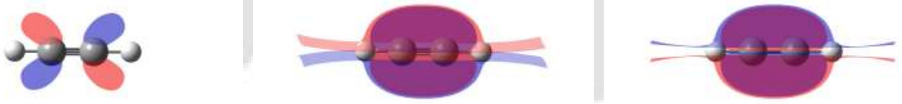

(d) LUMO+3 (e) LUMO+4 (f) LUMO+5

FIGURE 2.12: Plots of few virtual orbitals of neutral C_2H_2 molecule for aug-cc-pVDZ basis set. The degenerate states LUMO+2 and LUMO+3 are clearly identified as $\pi^\star$ antibonding orbitals.

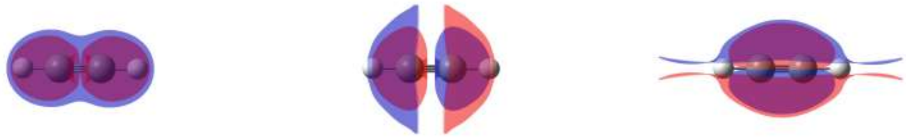

(a) LUMO (b) LUMO+1 (c) LUMO+2

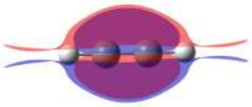

(d) LUMO+3 (e) LUMO+4 (f) LUMO+5

FIGURE 2.13: Plots of few virtual orbitals of neutral C_2H_2 molecule for aug-cc-pVTZ basis set. The degenerate states LUMO+4 and LUMO+5 are clearly identified as $\pi^\star$ antibonding orbitals.

To accurately determine the location of the LUMO, HF calculations with varying the nuclear charge along with PEM for different basis sets are carried out. Additional nuclear charge has been added to C atoms only. As shown in Figure 2.14, it is observed that the energy of the LUMO orbital using 6-311G and cc-pVTZ basis sets, while LUMO+4 in the case of aug-cc-pVDZ and aug-cc-pVTZ basis sets, experienced a greater degree of stabilization as a result of variations in the nuclear charge compared to the energies of the remaining virtual orbitals for neutral C_2H_4. However in figure 2.15 , it can be observed that the energy of the LUMO+3 orbital using 6-311G and cc-pVTZ basis sets while LUMO+4 in the case of aug-cc-pVDZ and aug-cc-pVTZ basis sets experience a greater degree of stabilization as a result of variations in z compared to the energies of the remaining virtual orbitals for neutral C_2H_2. The reason for this enhanced stabilization of the actual LUMO lies in the fact that the $\pi^\star$ antibonding is more localized in close proximity to the two C nuclei. It is noteworthy that even when using compact basis sets, the LUMO orbital of the C_2H_2 molecule does not resemble the shape of the $\pi^\star$ antibonding orbital. Therefore, relying solely on compact basis sets for the LUMO orbital may not always be the best choice.

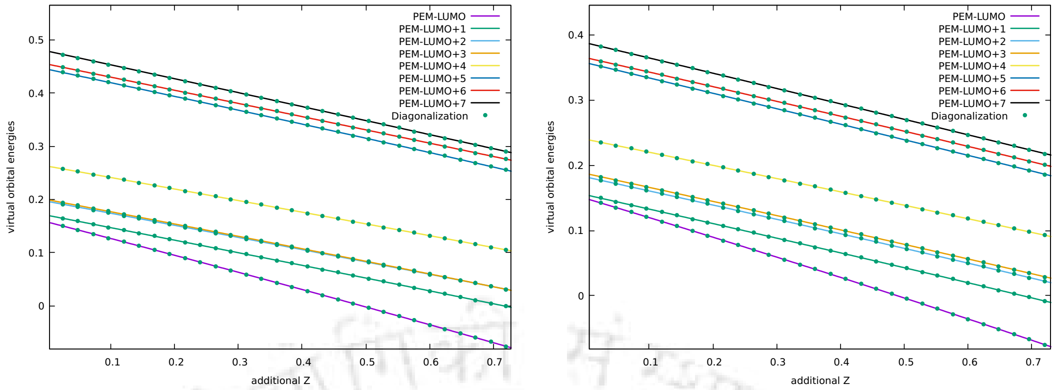

(a) 6-311G

(b) cc-pVTZ

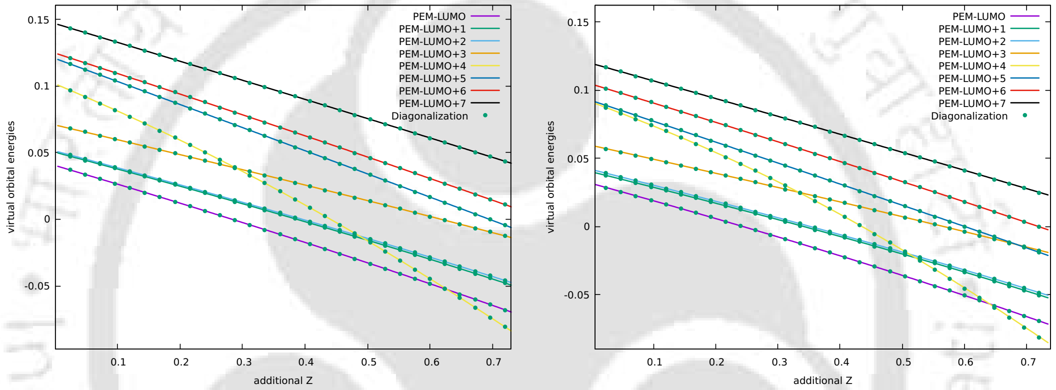

(c) aug-cc-pVDZ

(d) aug-cc-pVTZ

FIGURE 2.14: Plot of the few lowest virtual orbital energies in Hartree (on y-axis) as function of additional nuclear charge (on x-axis) of neutral C_2H_4 molecule for different basis sets. For increasing nuclear charge, the LUMO state is more stabilized for the 6-311G and cc-pVTZ basis sets, while LUMO+4 is more stabilized for the aug-cc-pVDZ and aug-cc-pVTZ basis sets. The PEM solution agrees well with diagonalization results (represented by green dots).

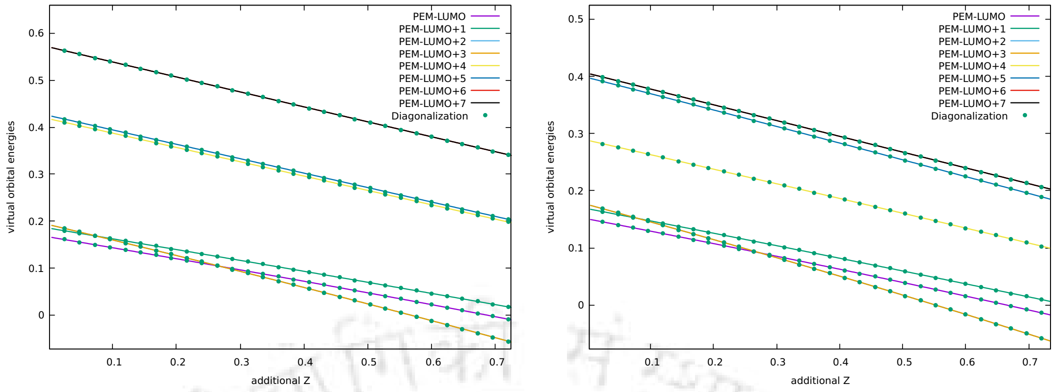

(a) 6-311G (b) cc-pVTZ

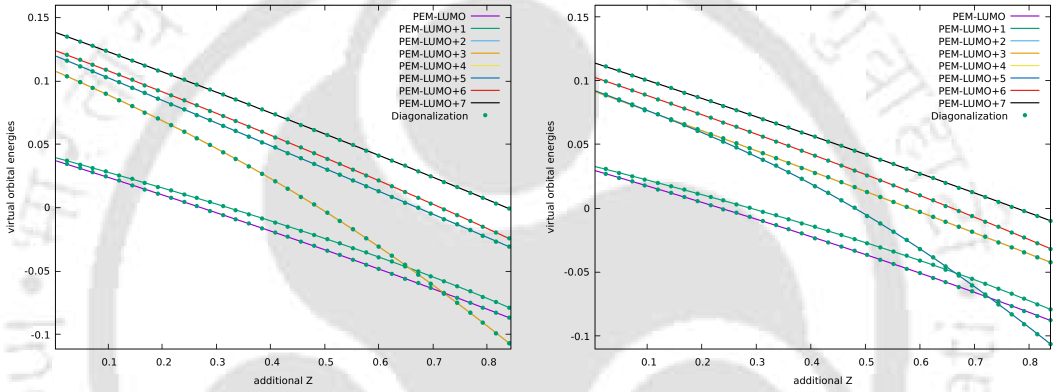

(c) aug-cc-pVDZ (d) aug-cc-pVTZ

FIGURE 2.15: Plot of the few virtual lowest orbital energies in Hartree (on y-axis) as function of additional nuclear charge (on x-axis) of neutral C_2H_2 molecule for different basis sets. The degenerate states (i.e.,LUMO+2 and LUMO+3) are getting more stabilized for 6-311G,cc-pVTZ and aug-cc-pVDZ basis sets, while degenerate states (i.e., LUMO+4 and LUMO+5) are getting stabilized in the case of aug-cc-pVTZ basis set as the nuclear charge increases. The PEM solution agrees well with diagonalization results (represented by green dots).

For comparison, orbital energies have been provided for different basis sets in Table 2.2 for neutral C_2H_4 and in Table 2.3 for neutral C_2H_2.

TABLE 2.2: Tabular data for orbital energies(in Hartree) of neutral C_2H_4 molecule for different basis sets. The identified LUMO energies are marked in bold.

6-311G	cc-pVTZ	aug-cc-pVDZ	aug-cc-pVTZ
-11.2382	-11.2317	-11.2419	-11.2332
-11.2365	-11.2300	-11.2402	-11.2315
-1.0375	-1.0307	-1.0343	-1.0321
-0.7909	-0.7907	-0.7927	-0.7918
-0.6460	-0.6418	-0.6430	-0.6431
-0.5861	-0.5841	-0.5851	-0.5855
-0.5046	-0.5073	-0.5077	-0.5084
-0.3752	-0.3752	-0.3753	-0.3759
0.1573	**0.1492**	0.0404	0.0317
0.1699	0.1547	0.0504	0.0402
0.1962	0.1821	0.0513	0.0419
0.1993	0.1874	0.0708	0.0596
0.2624	0.2399	**0.1017**	**0.0914**
0.4446	0.3573	0.1207	0.0925
0.4542	0.3650	0.1247	0.1045
0.4787	0.3878	0.1469	0.1197

TABLE 2.3: Tabular data for orbital energies(in Hartree) of neutral C_2H_2 for different basis sets. The identified LUMO energies are marked in bold.

6-311G	cc-pVTZ	aug-cc-pVDZ	aug-cc-pVTZ
-11.2511	-11.2418	-11.2540	-11.2432
-11.2473	-11.2380	-11.2502	-11.2393
-1.0409	-1.0290	-1.0341	-1.0307
-0.7616	-0.7662	-0.7678	-0.7673
-0.6815	-0.6799	-0.6807	-0.6812
-0.4120	-0.4100	-0.4111	-0.4111
-0.4120	-0.4100	-0.4111	-0.4111
0.1663	0.1506	0.0374	0.0301
0.1850	0.1685	0.0398	0.0332
0.1924	**0.1757**	**0.1082**	0.0920
0.1924	**0.1757**	**0.1082**	0.0920
0.4179	0.2882	0.1202	**0.0927**
0.4247	0.3979	0.1202	**0.0927**
0.5708	0.4054	0.1244	0.1031
0.5708	0.4054	0.1387	0.1143
0.7171	0.4853	0.1775	0.1366

2.2.2 Effect of additional diffuse basis function

To observe the effect of additional basis function, the PEM in conjunction with the nuclear charge stabilization method is implemented to neutral C_2H_4 and C_2H_2 molecule to identify the true LUMO using cc-pVDZ with different extra augmentations of p-type functions. The additional augmentations of p-type functions are done so that the smallest exponent in the previous basis set is multiplied by $1/2^n$ where n ranges from 1 to 10 for n-p augmentations.

2.2.2.1 $\pi^\star$ orbital of neutral C_2H_4 molecule for different basis sets

In order to accurately determine the location of the LUMO, HF calculation is performed with varying nuclear charges along with PEM using different basis sets and it is observed that there are avoided crossings between some states. The number of states involved in avoided crossing keeps increasing with an increase in additional p-type functions in the basis set as seen in Fig.(2.16(a)-2.16(k)). Separate HF calculations for different nuclear charge values are also conducted to obtain the charge stabilization curve for diagonalization results. In all figures, Fig.(2.16(a)-2.16(k)), the diagonalization results are represented with green dots while the PEM results are plotted as lines and they are on top of each other. The result obtained from PEM is found to be in agreement with the diagonalization results even for the basis set including highly diffuse basis functions. It is important to note that when employing diagonalization, the generation of a line plot for charge stabilization curves becomes exceedingly challenging due to the presence of multiple avoided crossings. Because the states exchange their behavior at these crossings, it's difficult to recognize which state is which, making it impossible to follow the curve even when looking at orbital plots.

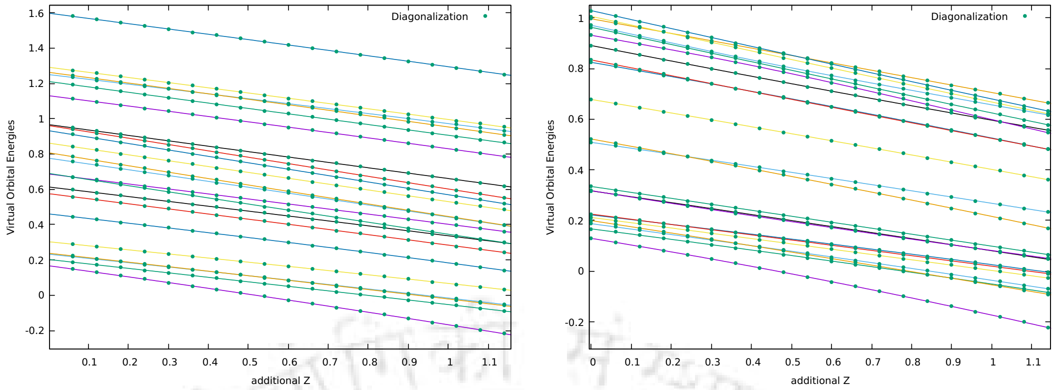

(a) cc-pVDZ (b) cc-pVDZ+1p

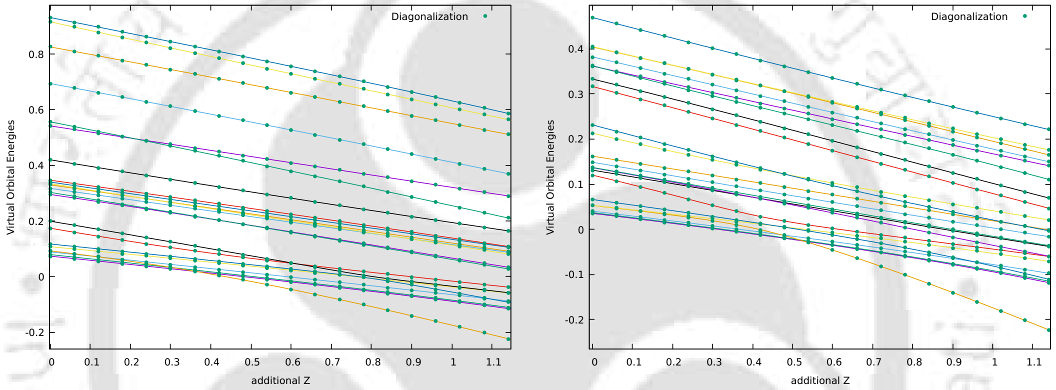

(c) cc-pVDZ+2p (d) cc-pVDZ+3p

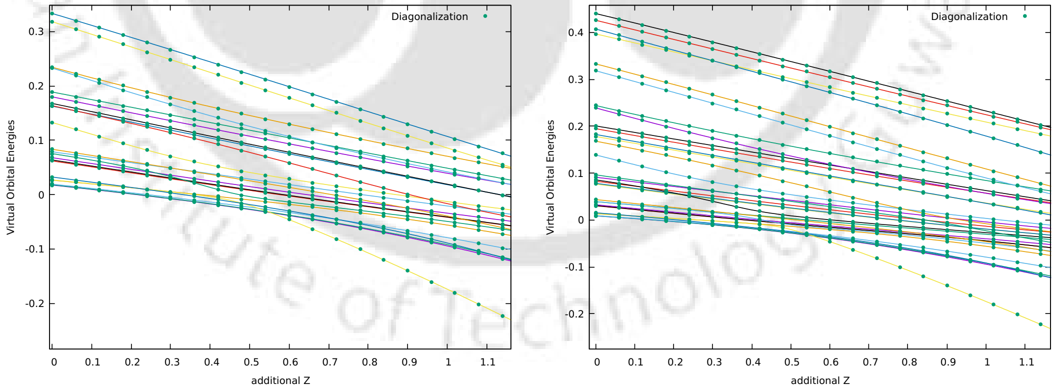

(e) cc-pVDZ+4p (f) cc-pVDZ+5p

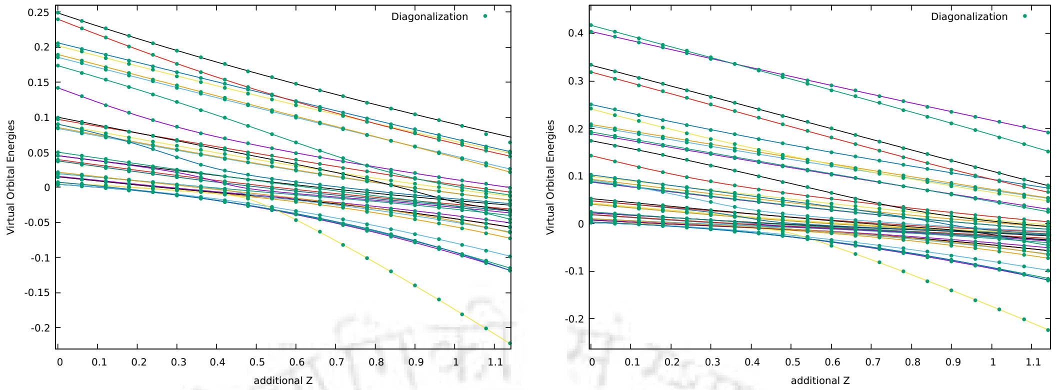

(g) cc-pVDZ+6p (h) cc-pVDZ+7p

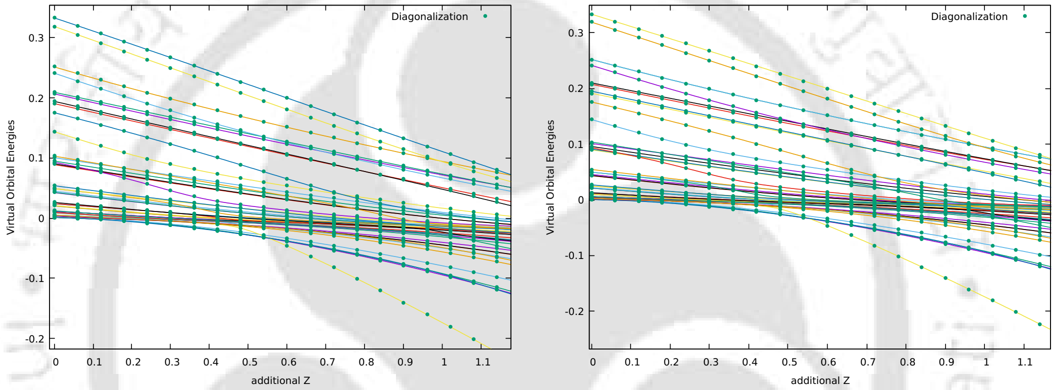

(i) cc-pVDZ+8p (j) cc-pVDZ+9p

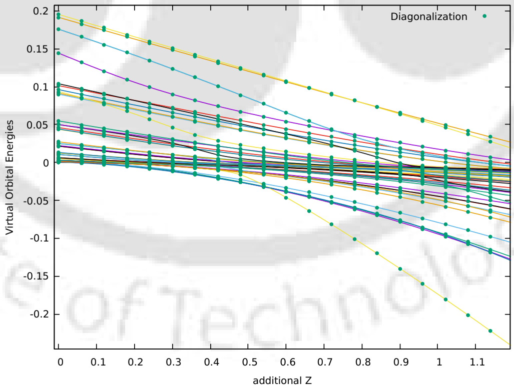

(k) cc-pVDZ+10p

FIGURE 2.16: Plot of the few lowest virtual orbital energies in Hartree (on the y-axis) as function of additional nuclear charge (on the x-axis) of neutral C_2H_4 molecule using cc-pVDZ+np basis set. The PEM solution agrees well with diagonalization results (represented by green dots).

From the stabilization curve, it is expected that the most stabilized state at a higher nuclear charge is the true LUMO state, but this is not the case. To validate this, MOs are plotted. The corresponding MOs involved in avoided crossings with true LUMO using different basis sets are shown in Fig.(2.17-2.27), along with their orbital energy (in Hartree) and iso values. The MOs are arranged in descending order of their orbital energy value. The number of states involved in avoided crossings keeps changing with changes in augmented functions. All the states involved in avoided crossing are found to be of the same symmetry (i.e., $\pi^\star$ antibonding character).

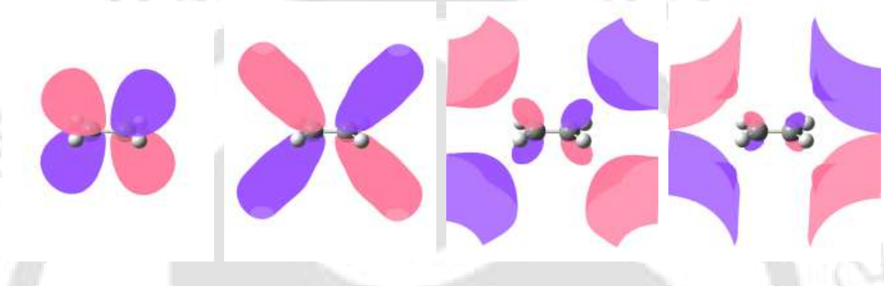

(a) $\epsilon = 0.1443$ Ha isovalue = 0.02

(b) $\epsilon = 0.0935$ Ha isovalue = 0.02

(c) $\epsilon = 0.0499$ Ha isovalue = 0.008

(d) $\epsilon = 0.0250$ Ha isovalue = 0.0025

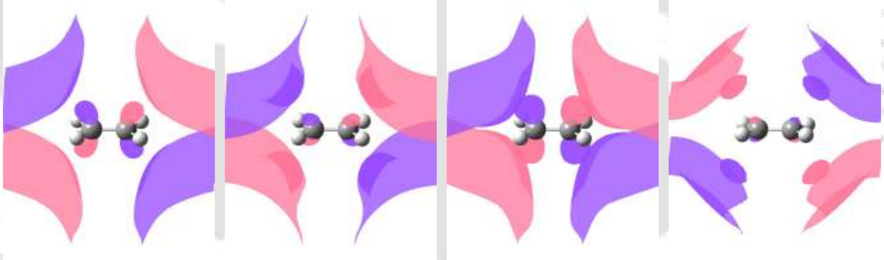

(e) $\epsilon = 0.0124$ Ha isovalue = 0.0007

(f) $\epsilon = 0.0060$ Ha isovalue = 0.0002

(g) $\epsilon = 0.0028$ Ha isovalue = 0.00005

(h) $\epsilon = 0.0012$ Ha isovalue = 0.00002

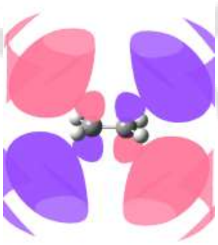

(i) $\epsilon = 0.0004$ Ha isovalue = 0.000005

FIGURE 2.17: Plot of the virtual orbitals having $\pi^\star$ antibonding character involved in avoided crossings with true LUMO using cc-pVDZ+10p basis set of neutral C_2H_4 molecule.

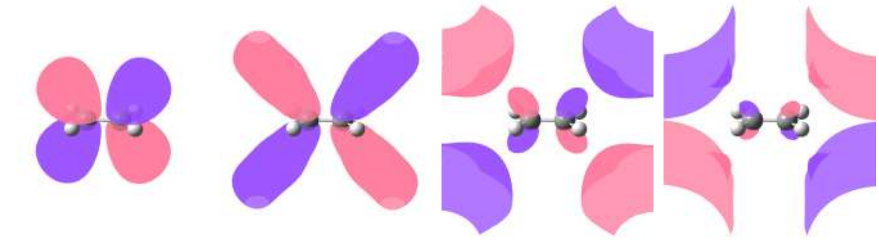

(a) $\epsilon = 0.1442$ Ha isovalue = 0.02

(b) $\epsilon = 0.0933$ Ha isovalue = 0.02

(c) $\epsilon = 0.0497$ Ha isovalue = 0.008

(d) $\epsilon = 0.0248$ Ha isovalue = 0.0025

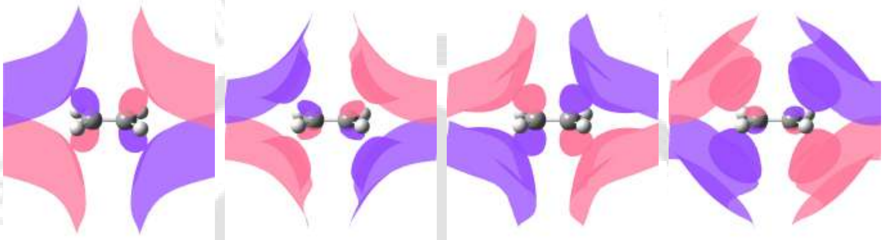

(e) $\epsilon = 0.0121$ Ha isovalue = 0.0006

(f) $\epsilon = 0.0057$ Ha isovalue = 0.00015

(g) $\epsilon = 0.0024$ Ha isovalue = 0.00004

(h) $\epsilon = 0.0008$ Ha isovalue = 0.000009

FIGURE 2.18: Same as Figure 2.17 using cc-pVDZ+9p basis set.

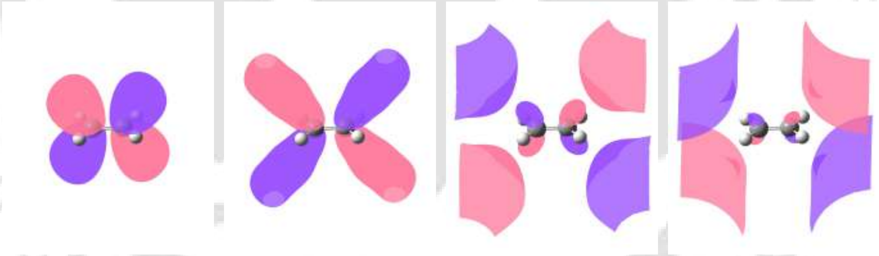

(a) $\epsilon = 0.1439$ Ha isovalue = 0.02

(b) $\epsilon = 0.0930$ Ha isovalue = 0.02

(c) $\epsilon = 0.0492$ Ha isovalue = 0.008

(d) $\epsilon = 0.0242$ Ha isovalue = 0.0025

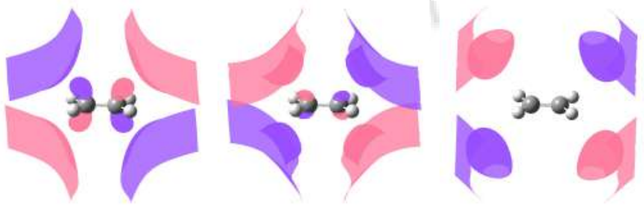

(e) $\epsilon = 0.0114$ Ha isovalue = 0.0006

(f) $\epsilon = 0.0050$ Ha isovalue = 0.00015

(g) $\epsilon = 0.0017$ Ha isovalue = 0.00006

FIGURE 2.19: Same as Figure 2.17 using cc-pVDZ+8p basis set.

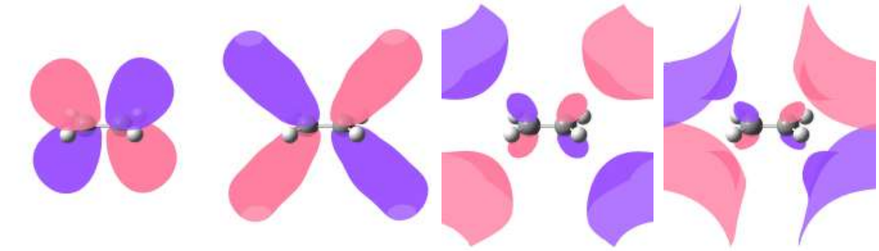

(a) $\epsilon = 0.1433$ Ha
isovalue = 0.02

(b) $\epsilon = 0.0922$ Ha
isovalue = 0.02

(c) $\epsilon = 0.0480$ Ha
isovalue = 0.008

(d) $\epsilon = 0.0228$ Ha
isovalue = 0.002

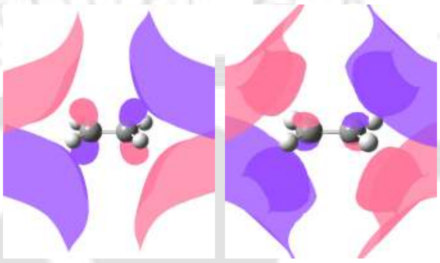

(e) $\epsilon = 0.0099$ Ha
isovalue = 0.0005

(f) $\epsilon = 0.0034$ Ha
isovalue = 0.00009

FIGURE 2.20: Same as Figure 2.17 using cc-pVDZ+7p basis set.

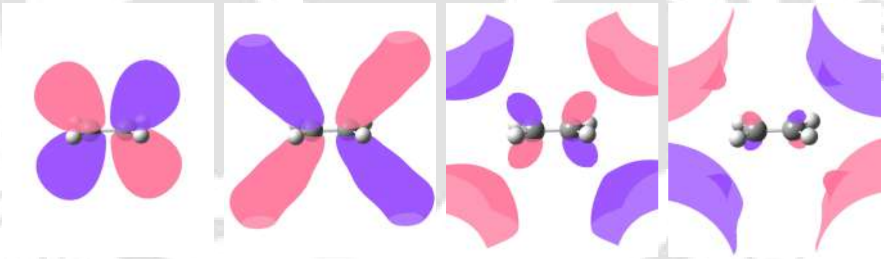

(a) $\epsilon = 0.1419$ Ha
isovalue = 0.02

(b) $\epsilon = 0.0902$ Ha
isovalue = 0.02

(c) $\epsilon = 0.0453$ Ha
isovalue = 0.007

(d) $\epsilon = 0.0198$ Ha
isovalue = 0.002

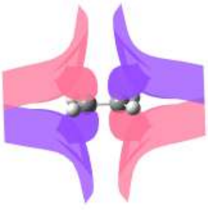

(e) $\epsilon = 0.0068$ Ha
isovalue = 0.0002

FIGURE 2.21: Same as Figure 2.17 using cc-pVDZ+6p basis set.

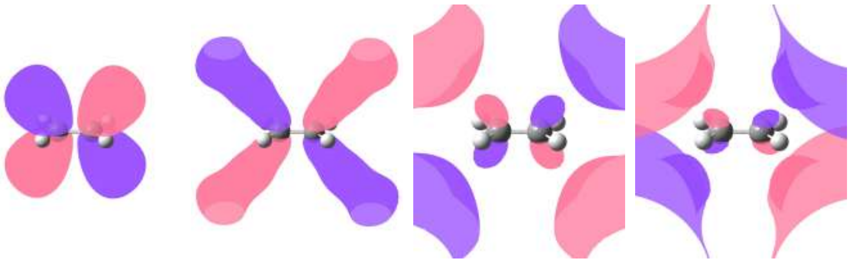

(a) $\epsilon = 0.1389$ Ha isovalue = 0.02 (b) $\epsilon = 0.0856$ Ha isovalue = 0.02 (c) $\epsilon = 0.0393$ Ha isovalue = 0.006 (d) $\epsilon = 0.0135$ Ha isovalue = 0.001

FIGURE 2.22: Same as Figure 2.17 using cc-pVDZ+5p basis set.

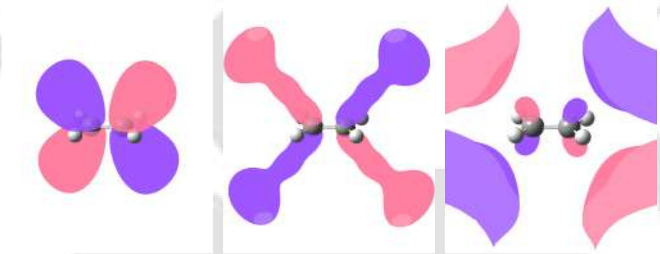

(a) $\epsilon = 0.1326$ Ha isovalue = 0.02 (b) $\epsilon = 0.0753$ Ha isovalue = 0.02 (c) $\epsilon = 0.0269$ Ha isovalue = 0.004

FIGURE 2.23: Same as Figure 2.17 using cc-pVDZ+4p basis set.

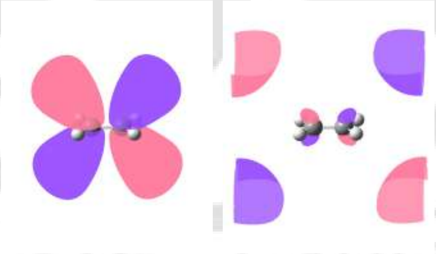

(a) $\epsilon = 0.1201$ Ha isovalue = 0.02 (b) $\epsilon = 0.0528$ Ha isovalue = 0.015

FIGURE 2.24: Same as Figure 2.17 using cc-pVDZ+3p basis set.

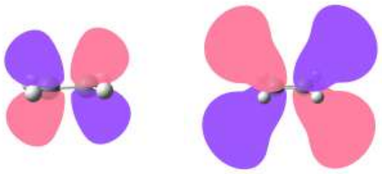

(a) $\epsilon = 0.1744$ Ha
isovalue = 0.03

(b) $\epsilon = 0.0929$ Ha
isovalue = 0.02

FIGURE 2.25: Same as Figure 2.17 using cc-pVDZ+2p basis set.

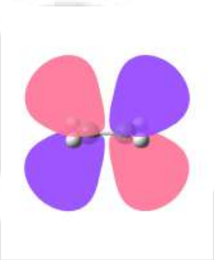

(a) $\epsilon = 0.1293$ Ha
isovalue = 0.02

FIGURE 2.26: Same as Figure 2.17 using cc-pVDZ+1p basis set.

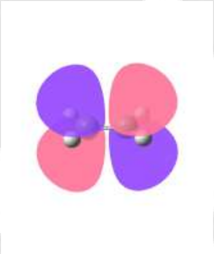

(a) $\epsilon = 0.1669$ Ha
isovalue = 0.02

FIGURE 2.27: Same as Figure 2.17 using cc-pVDZ basis set.

It is observed that the most stabilized state from the stabilization curve is the most diffused $\pi^\star$ antibonding state at z = 0 and approaches to zero orbital energy with an increase in additional p-type functions in the basis set. The most stabilized state is the most diffused $\pi^\star$ antibonding at z = 0 and the same state at higher nuclear charge has well localized $\pi^\star$ antibonding charge due to exchange of behaviour after the avoided crossing. To visualize the avoided crossings clearly a separate plot for states involved in avoided crossings with true LUMO is shown in Fig.2.28. For example, in case of cc-pVDZ+5p (see Fig.2.28(c)), the state with higher energy shows localized $\pi^\star$ antibonding character (Fig. 2.22(a)) at z = 0. As the nuclear charge increases, this state switches behavior with the low-energy states at each avoided crossing, which exhibit diffuse $\pi^\star$ antibonding character (i.e., plotted at a low iso value). A similar behavior is observed for all basis sets with different numbers of extra augmentations. As there is an increase in the extra p-type function, there is an increase in the number of avoided crossings, and the state that is lowest in energy at z = 0 is getting stabilized at higher z due to the mixing of the same symmetry of $\pi^\star$ antibonding.

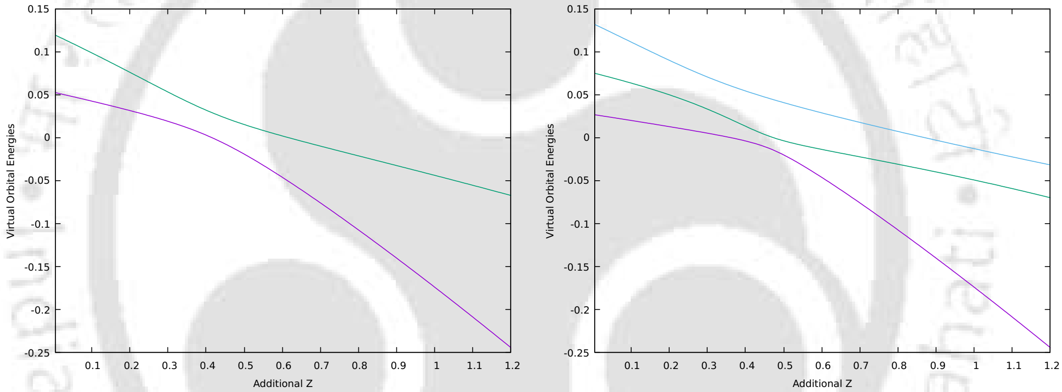

(a) cc-pVDZ+3p

(b) cc-pVDZ+4p

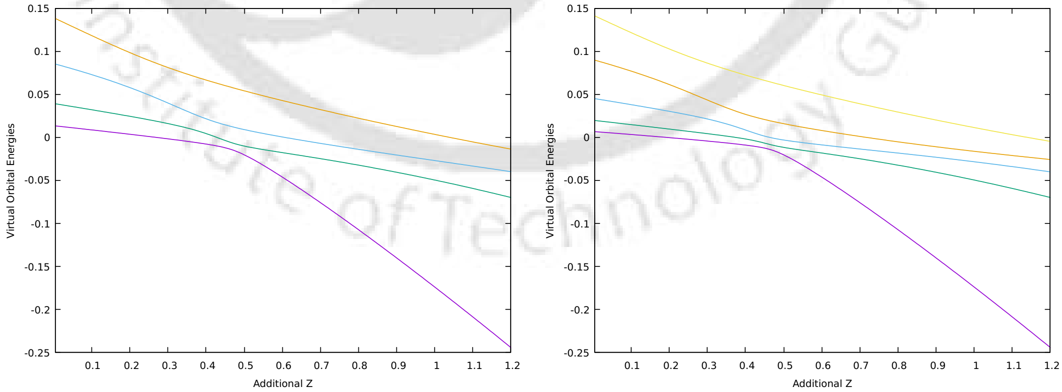

(c) cc-pVDZ+5p

(d) cc-pVDZ+6p

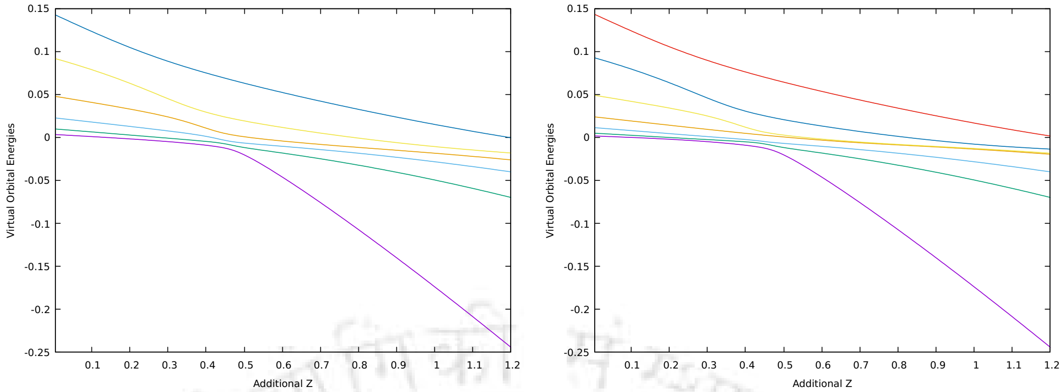

(e) cc-pVDZ+7p (f) cc-pVDZ+8p

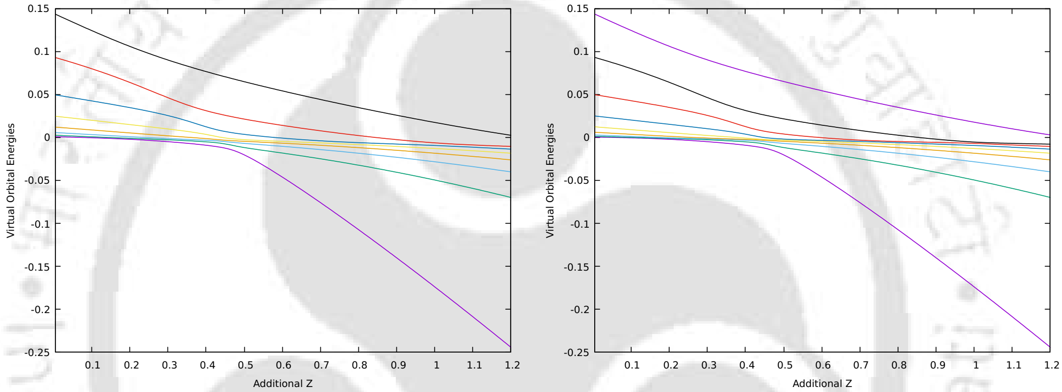

(g) cc-pVDZ+9p (h) cc-pVDZ+10p

FIGURE 2.28: Plot of the virtual orbital energies in Hartree (on y-axis) of $\pi^\star$ antibonding type orbitals involved in avoided crossing as function of additional nuclear charge (on x-axis) of neutral C_2H_4 molecule for cc-pVDZ+np basis set.

In such cases, the identification of the LUMO can not be carried by usual PEM. The modification of PEM is necessary to precisely identify the true LUMO by preventing the stabilization of states involved in avoided crossings. This modification of PEM is executed in the following two manners:

Case I) Ignoring the z dependency of c-matrix in PEM equations

Case II) Removing interaction between the states involved in avoided crossing from the c-matrix equation in PEM equation

Case I is achieved by solving only the change in orbital energy equation (i.e., Eq. 1.25) in PEM calculations and ignoring the Eq. 1.26 altogether. In contrast, case II is achieved by removing the interaction of the states involved in avoided crossing from Eq. 1.26, which means index j is not equal to those states, which leads to avoided crossing when index i represents the LUMO state. In practice, to achieve case II, the first step is identifying those states involved in avoided crossings with true LUMO by performing PEM, and the second step is to remove interaction from the Eq. 1.26 of the nearby states involved in avoided crossing with true LUMO manually.

When performing calculations with case I, a true LUMO state among all avoided crossing states is observed to stabilize in all cases with different p-type extra augmentation. In all calculations, there are no avoided crossings, as confirmed by Fig.(2.29(a)-2.29(k)). The similar results are obtained in case II, with no avoided crossings observed between the true LUMO state and other nearby states with the same symmetries (see Fig.(2.30(a)-2.30(k)). However, the curvature in case II is due to the interaction of the true LUMO state with the other $\pi^\star$ states for which the interactions have not been removed. The interactions have been removed for only nearby states involved in the avoided crossings. In case I, only N number of equations are solved, while in case II, N+N^2 equations are being solved in truncated PEM. Both cases are able to accurately determine the location of the LUMO state, but case I is advantageous due to its lower computational cost and reduced human effort. This is unlike case II, where states have to be removed manually. As outlined earlier, the PEM results are approximately ten times faster than those obtained through diagonalization. Therefore, modified PEM case I will be significantly faster than the results obtained through diagonalization as virtually all the computation time is taken by SCF calculation to get initial condition for PEM.

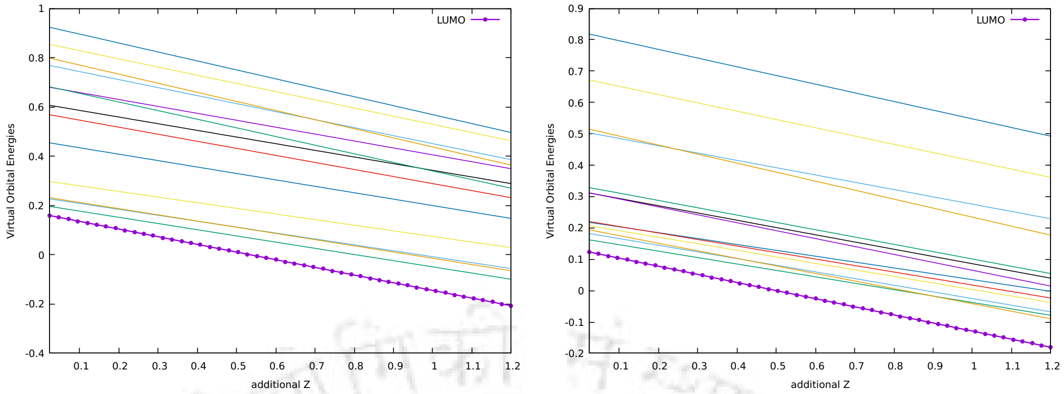

(a) cc-pVDZ (b) cc-pVDZ+1p

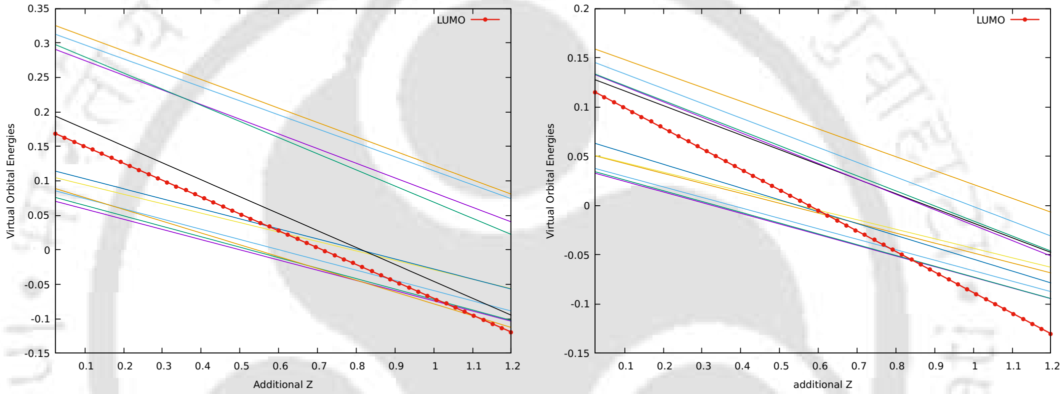

(c) cc-pVDZ+2p (d) cc-pVDZ+3p

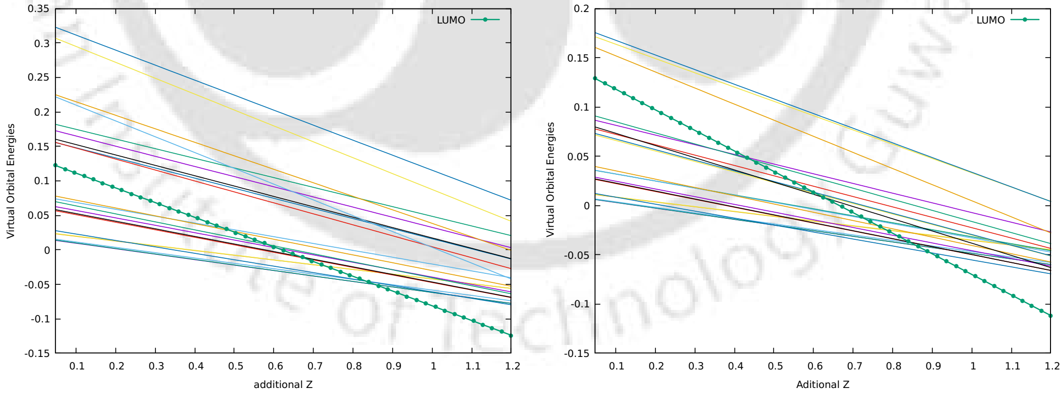

(e) cc-pVDZ+4p (f) cc-pVDZ+5p

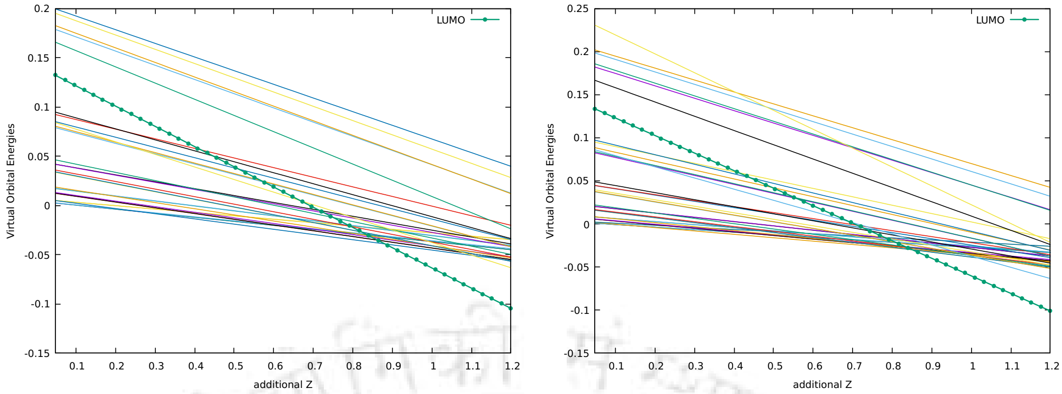

(g) cc-pVDZ+6p (h) cc-pVDZ+7p

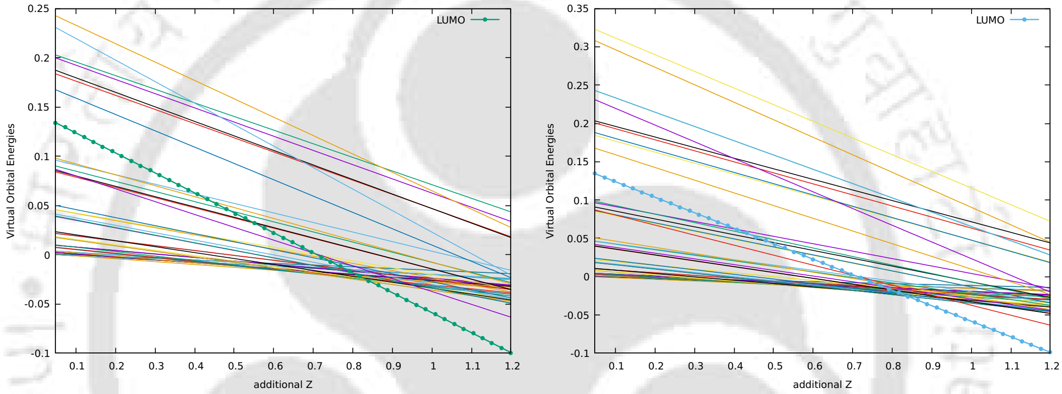

(i) cc-pVDZ+8p (j) cc-pVDZ+9p

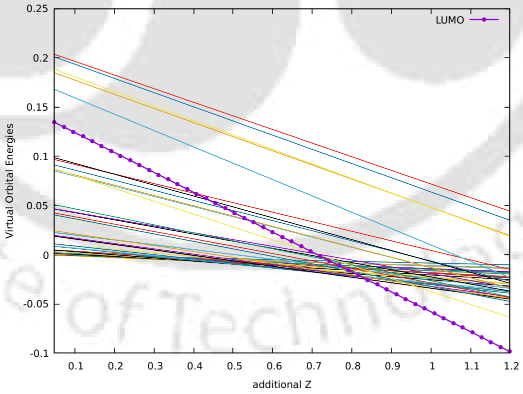

(k) cc-pVDZ+10p

FIGURE 2.29: Plot of the few lowest virtual orbital energies in Hartree (on the y-axis) as function of additional nuclear charge (on the x-axis) of neutral C_2H_4 molecule using cc-pVDZ+np basis set. The plot corresponds to modified PEM case I.

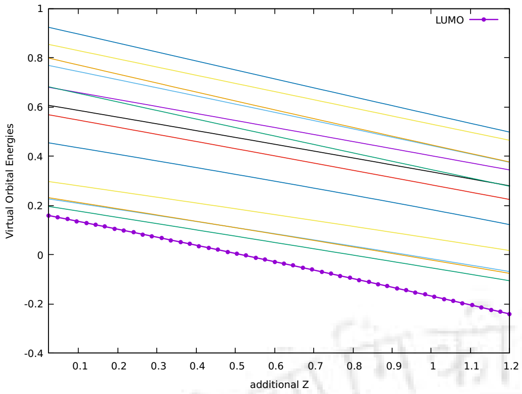

(a) cc-pVDZ

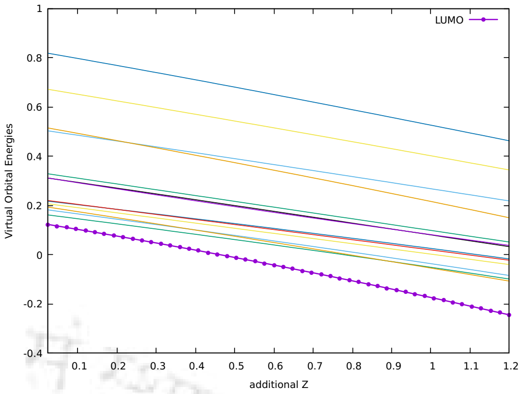

(b) cc-pVDZ+1p

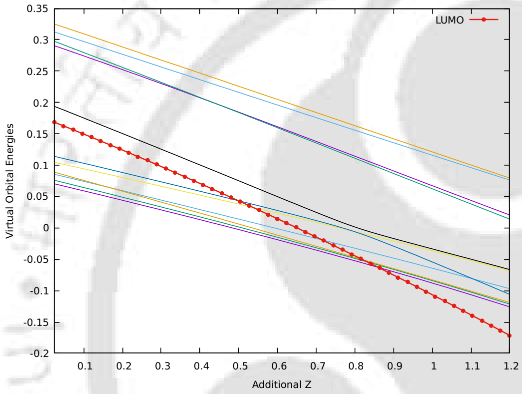

(c) cc-pVDZ+2p

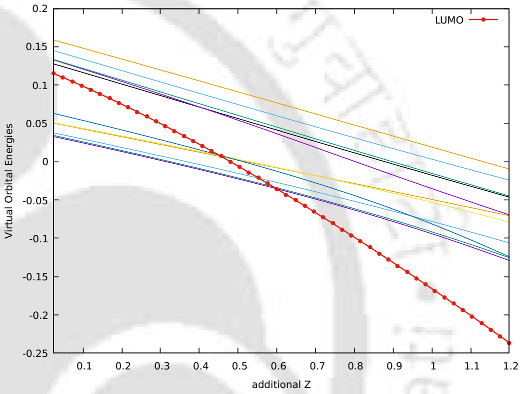

(d) cc-pVDZ+3p

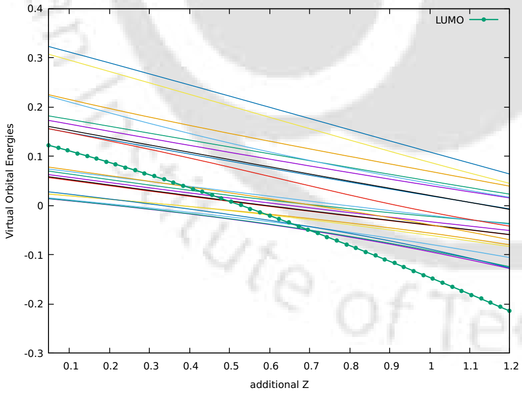

(e) cc-pVDZ+4p

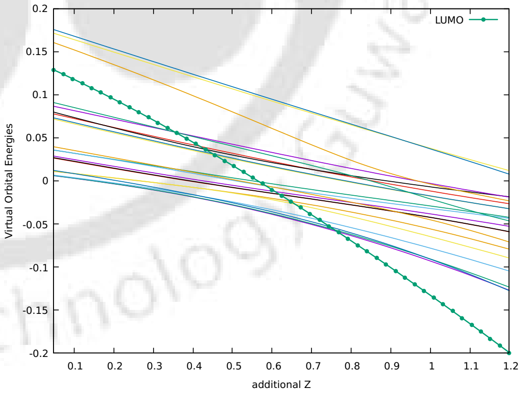

(f) cc-pVDZ+5p

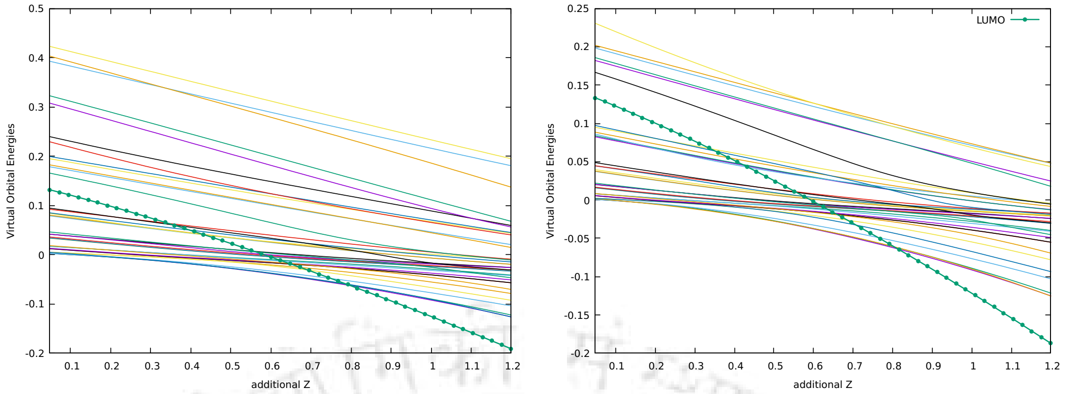

(g) cc-pVDZ+6p (h) cc-pVDZ+7p

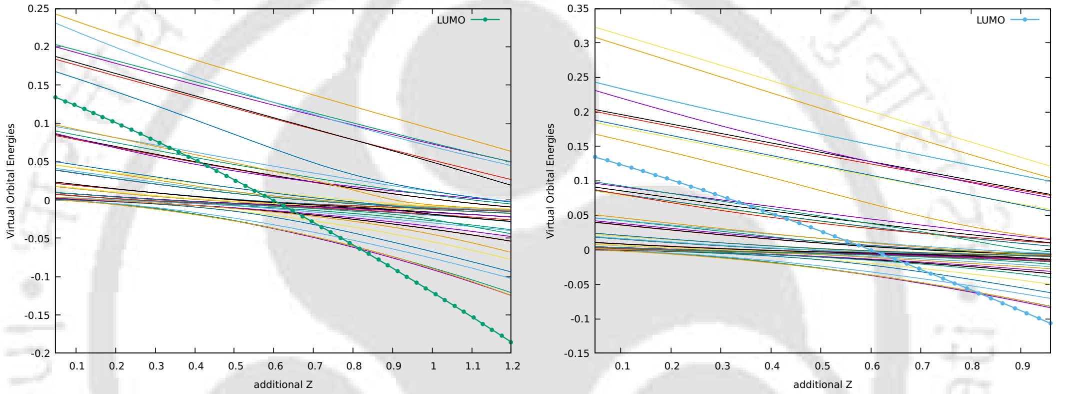

(i) cc-pVDZ+8p (j) cc-pVDZ+9p

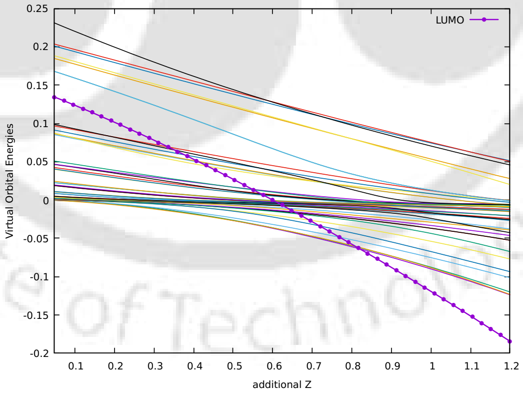

(k) cc-pVDZ+10p

FIGURE 2.30: Plot of the few lowest virtual orbital energies in Hartree (on the y-axis) as function of additional nuclear charge (on the x-axis) of neutral C_2H_4 molecule using cc-pVDZ+np basis set. The plot corresponds to modified PEM case II.

Orbital probability densities (i.e., $4\pi^2r^2\rho(r)$ vs r) are plotted (in Fig. 2.31) for the states involved in avoided crossing with the true LUMO using Multiwfn software[145]. For comparison, Figure 2.31 contains orbital probability densities corresponding to a particular state with similar orbital profile in different basis sets (i.e., cc-pVDZ+np). Fig.2.31(a) corresponds to the true LUMO identified with modified PEM having $\pi^\star$ antibonding character, and it is seen that this state is very well localized near the nucleus. With the extra augmentation of p-type functions, there is the appearance of several other peaks with low probability values due to the mixing of higher energy $\pi^\star$ MO's[146]. Figure 2.31(b) corresponds to the state with the lowest energy (i.e., close to zero) among all the states involved in avoided crossing. It is clear that with the increase in the extra p-type function, this state becomes more and more localized away from the nucleus and becomes more diffuse. For all other states, there is a major peak located far from the nucleus. So, it is also evident from orbital probability densities that the most stabilized state obtained from modified PEM is the most localized state near the nucleus.

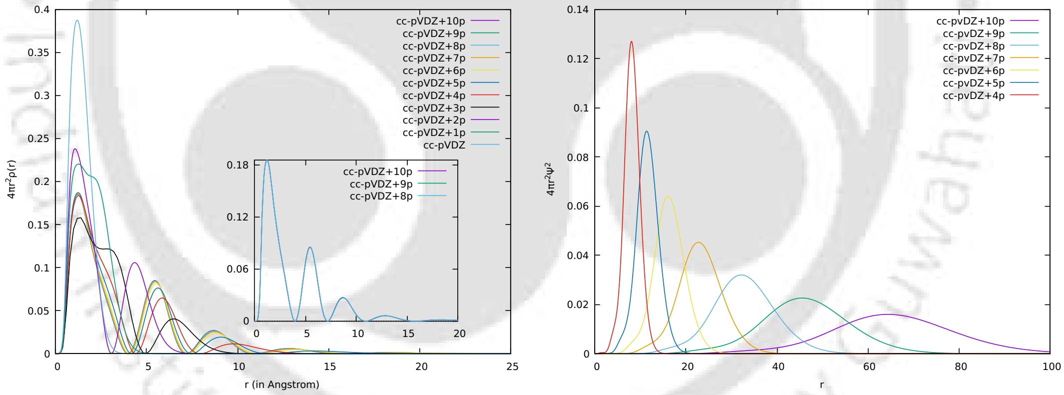

(a) (b)

FIGURE 2.31: Plot of Orbital probability density (on the y-axis) vs r in angstrom (on the the x-axis) for true LUMO and the most diffuse state involved in avoided crossing of C_2H_4 using cc-pVDZ+np basis set.

To analyze the impact of the p-type function on the true LUMO energy of C_2H_4, the successive augmentation of p-type functions is done up to 10p-type functions using various basis sets (i.e., 6-311G, cc-pVDZ, aug-cc-pVDZ, and aug-cc-pVTZ). The additional p-type function is added in the same way in all cases by taking half of the smallest exponent of p-type in the previous basis set. It is observed that the true LUMO orbital energies converged with the increase in additional p-type functions across all basis sets. This finding is significant for the scientific community, especially those working in the field of resonances and phenomena that involve the use of additional diffuse functions. For cc-pVDZ+8p/9p/10p, true LUMO orbital energies are almost the same (see Table 2.4), and their orbital densities plots also overlap with each other (see inset of Fig. 2.31(a)). True LUMO orbital energies are reported in Table 2.4. Reported energies correspond to z = 0 (i.e., without additional nuclear charge).

TABLE 2.4: Orbital energies of identified LUMOs (in Hartree) of neutral C_2H_4 molecule using different basis sets upto extra augmentation of 10 p-type functions.

C_2H_4				
Augmentation	6-311G	cc-pVDZ	aug-cc-pVDZ	aug-cc-pVTZ
0p	0.1573	0.1669	0.1069	0.0914
1p	0.12676	0.1293	0.1270	0.1177
2p	0.0895	0.0929	0.1401	0.1295
3p	0.1161	0.1201	0.1470	0.1353
4p	0.1280	0.1326	0.1504	0.1380
5p	0.1340	0.1389	0.1519	0.1392
6p	0.1368	0.1419	0.1526	0.1398
7p	0.1380	0.1432	0.1529	0.1400
8p	0.1386	0.1438	0.1531	0.1401
9p	0.1388	0.1442	0.1531	0.1402
10p	0.1389	0.1443	0.1531	0.1402

2.2.2.2 $\pi^\star$ orbital of neutral C_2H_2 molecule for different basis sets

Similar calculations are performed to C_2H_2 molecule with different basis sets upto augmentation of 10 p-type functions. Similar observation are made regarding avoided crossings and relevant charge stabilization plots corresponding to cc-pVDZ+np basis sets are shown in figure 2.32. The orbital pictures of all the states involved in avoided crossings using cc-pVDZ+np basis sets are shown in figures 2.33-2.43. To prevent the stabilization of these avoided crossing states, the modified PEM calculations are carried out for both the cases and relevant plots for the cc-pVDZ basis set with up to 10 p-type functions are shown in figures 2.44-2.45.

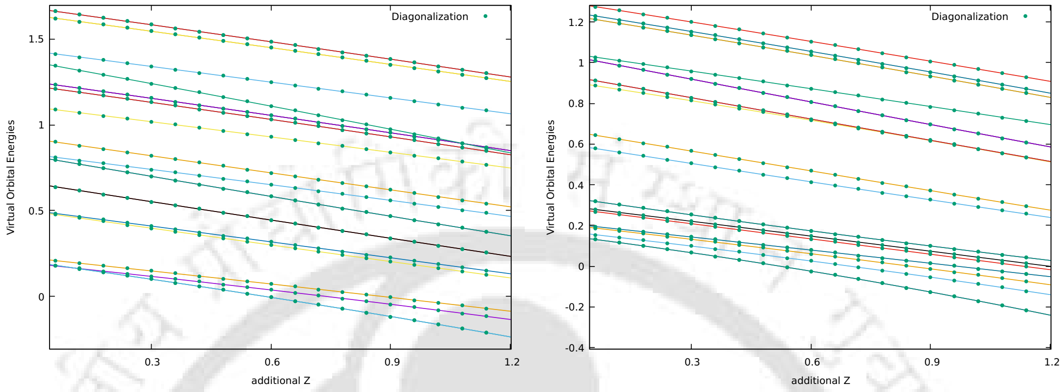

(a) cc-pVDZ (b) cc-pVDZ+1p

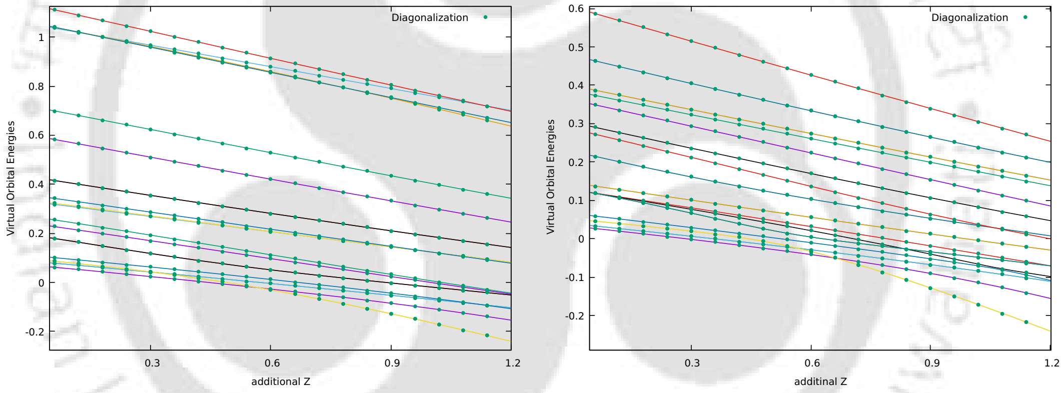

(c) cc-pVDZ+2p (d) cc-pVDZ+3p

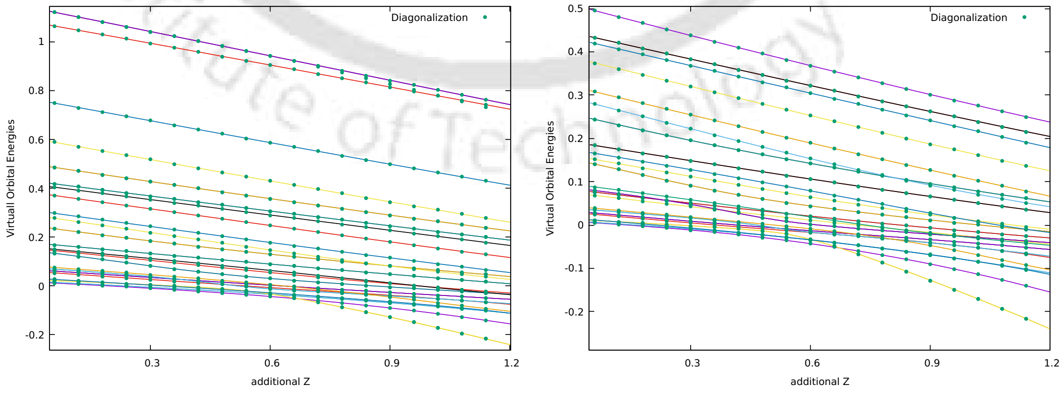

(e) cc-pVDZ+4p (f) cc-pVDZ+5p

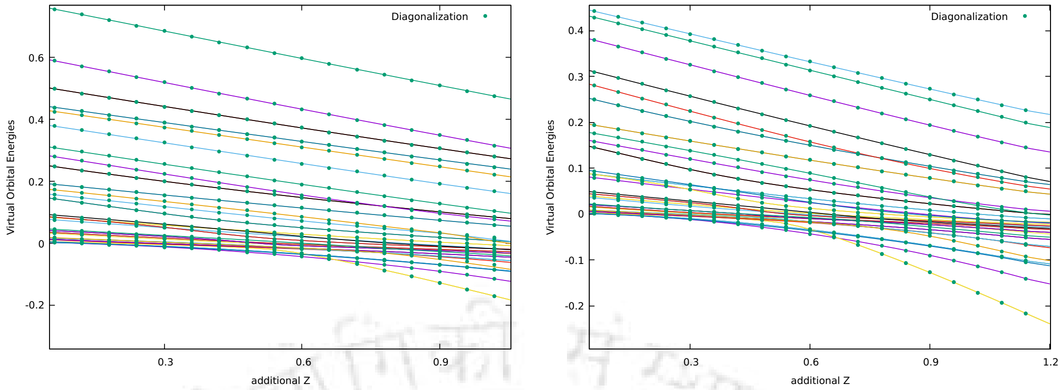

(g) cc-pVDZ+6p (h) cc-pVDZ+7p

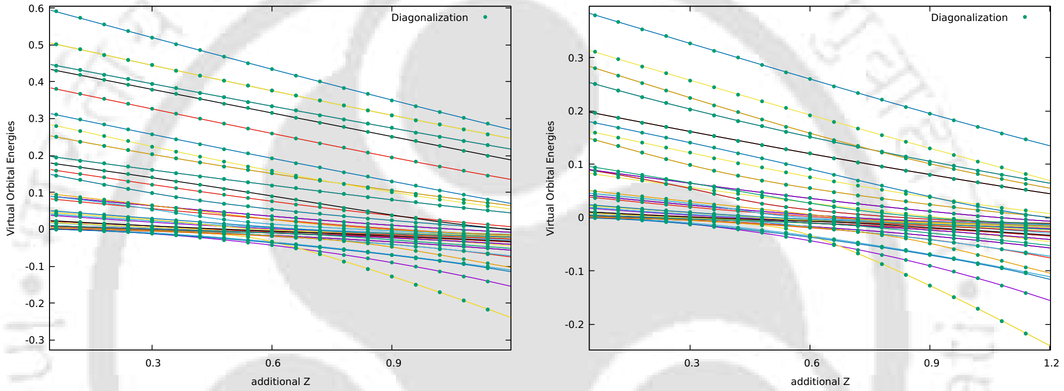

(i) cc-pVDZ+8p (j) cc-pVDZ+9p

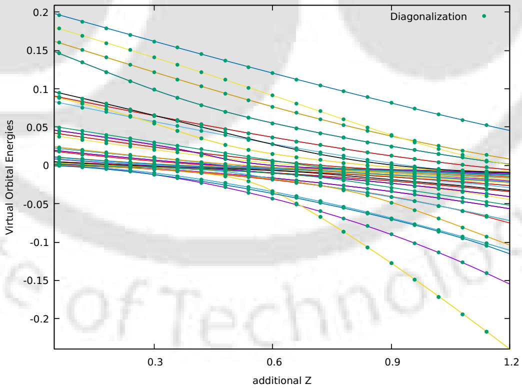

(k) cc-pVDZ+10p

Figure 2.32: Plot of the few lowest virtual orbital energies in Hartree (on the y-axis) as function of additional nuclear charge (on the x-axis) of neutral C_2H_2 molecule using cc-pVDZ+np basis set. The PEM solution agrees well with diagonalization results (represented by green dots).

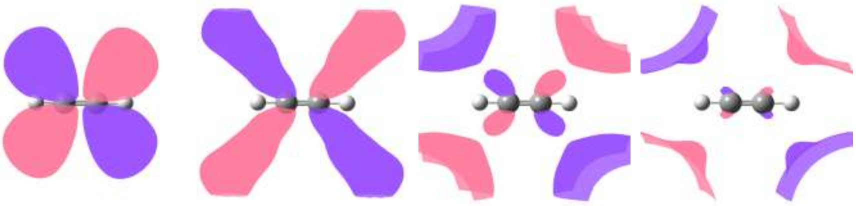

(a) $\epsilon = 0.1583$ Ha isovalue = 0.02

(b) $\epsilon = 0.0951$ Ha isovalue = 0.02

(c) $\epsilon = 0.0496$ Ha isovalue = 0.007

(d) $\epsilon = 0.0241$ Ha isovalue = 0.0025

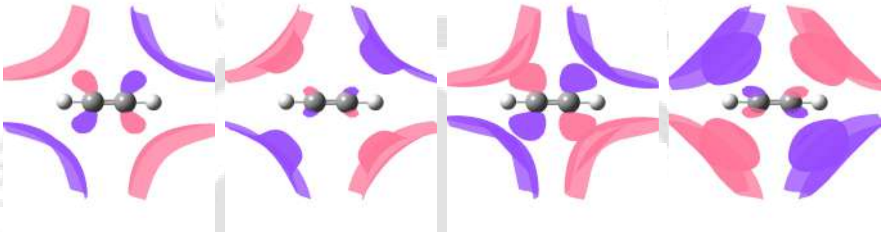

(e) $\epsilon = 0.0124$ Ha isovalue = 0.0006

(f) $\epsilon = 0.0060$ Ha isovalue = 0.0002

(g) $\epsilon = 0.0028$ Ha isovalue = 0.00004

(h) $\epsilon = 0.0012$ Ha isovalue = 0.000012

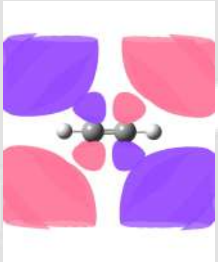

(i) $\epsilon = 0.0004$ Ha isovalue = 0.000003

Figure 2.33: Plot of the virtual orbitals having $\pi^\star$ antibonding character involved in avoided crossings with true LUMO using cc-pVDZ+10p basis set for neutral C_2H_2 molecule.

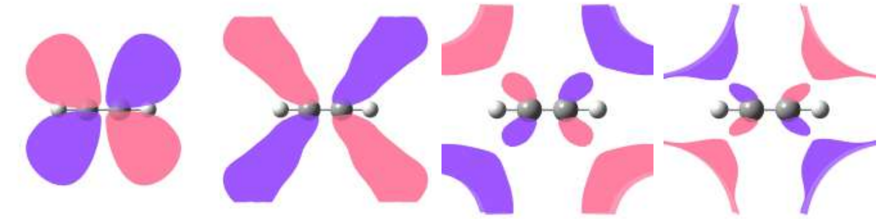

(a) $\epsilon = 0.1582$ Ha isovalue = 0.02
(b) $\epsilon = 0.0949$ Ha isovalue = 0.02
(c) $\epsilon = 0.0493$ Ha isovalue = 0.007
(d) $\epsilon = 0.0246$ Ha isovalue = 0.002

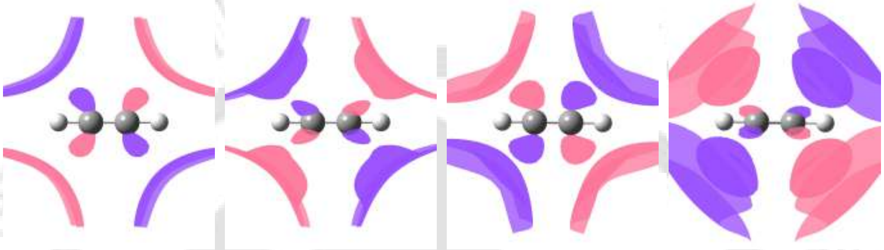

(e) $\epsilon = 0.0120$ Ha isovalue = 0.0006
(f) $\epsilon = 0.0057$ Ha isovalue = 0.00015
(g) $\epsilon = 0.0025$ Ha isovalue = 0.00004
(h) $\epsilon = 0.0008$ Ha isovalue = 0.000009

FIGURE 2.34: Same as Figure 2.33 using cc-pVDZ+9p basis set.

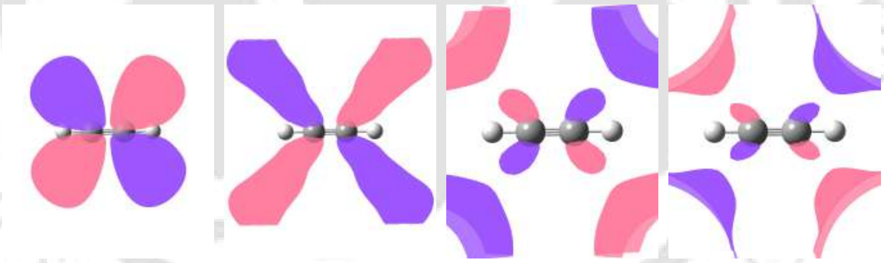

(a) $\epsilon = 0.1579$ Ha isovalue = 0.02
(b) $\epsilon = 0.0945$ Ha isovalue = 0.02
(c) $\epsilon = 0.0488$ Ha isovalue = 0.007
(d) $\epsilon = 0.0240$ Ha isovalue = 0.002

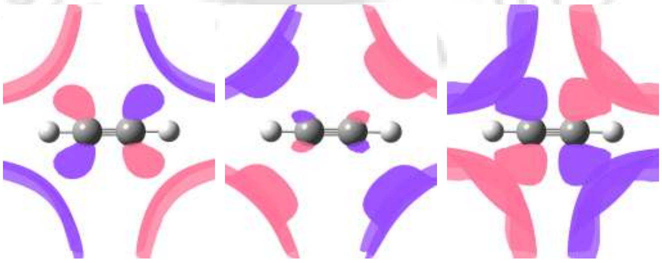

(e) $\epsilon = 0.0113$ Ha isovalue = 0.0005
(f) $\epsilon = 0.0049$ Ha isovalue = 0.00015
(g) $\epsilon = 0.0017$ Ha isovalue = 0.00002

FIGURE 2.35: Same as Figure 2.33 using cc-pVDZ+8p basis set.

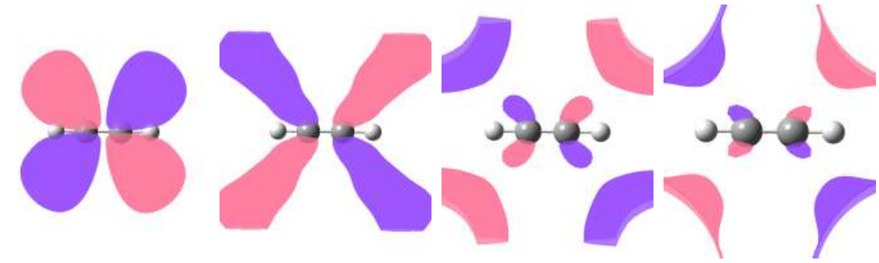

(a) $\epsilon = 0.1573$ Ha isovalue = 0.02

(b) $\epsilon = 0.0936$ Ha isovalue = 0.02

(c) $\epsilon = 0.0476$ Ha isovalue = 0.007

(d) $\epsilon = 0.0226$ Ha isovalue = 0.002

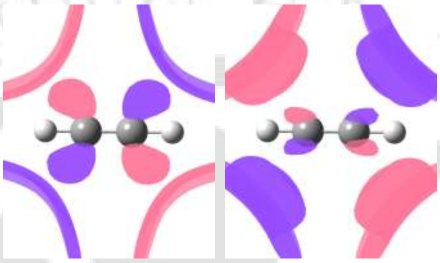

(e) $\epsilon = 0.0098$ Ha isovalue = 0.0004

(f) $\epsilon = 0.0034$ Ha isovalue = 0.00008

FIGURE 2.36: Same as Figure 2.33 using cc-pVDZ+7p basis set.

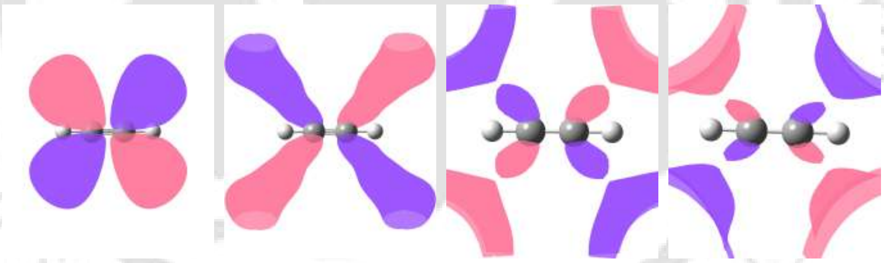

(a) $\epsilon = 0.1559$ Ha isovalue = 0.02

(b) $\epsilon = 0.0914$ Ha isovalue = 0.02

(c) $\epsilon = 0.0449$ Ha isovalue = 0.006

(d) $\epsilon = 0.0196$ Ha isovalue = 0.0015

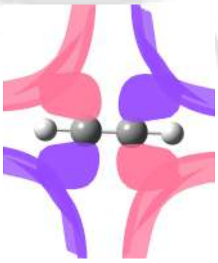

(e) $\epsilon = 0.0067$ Ha isovalue = 0.0002

FIGURE 2.37: Same as Figure 2.33 using cc-pVDZ+6p basis set.

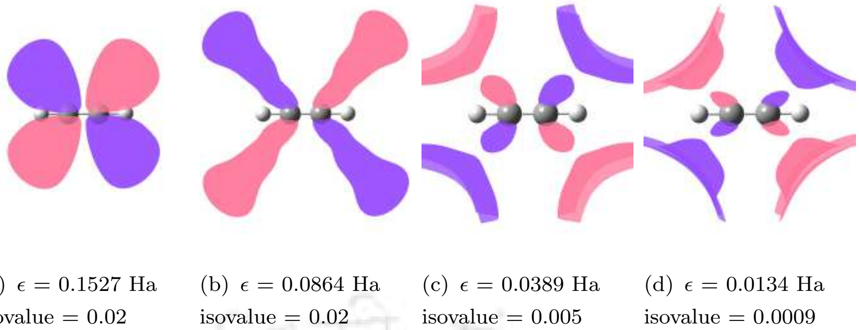
(a) $\epsilon = 0.1527$ Ha
isovalue = 0.02
(b) $\epsilon = 0.0864$ Ha
isovalue = 0.02
(c) $\epsilon = 0.0389$ Ha
isovalue = 0.005
(d) $\epsilon = 0.0134$ Ha
isovalue = 0.0009

FIGURE 2.38: Same as Figure 2.33 using cc-pVDZ+5p basis set.

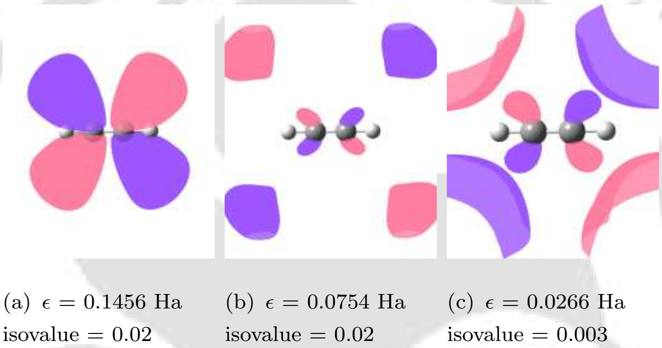
(a) $\epsilon = 0.1456$ Ha
isovalue = 0.02
(b) $\epsilon = 0.0754$ Ha
isovalue = 0.02
(c) $\epsilon = 0.0266$ Ha
isovalue = 0.003

FIGURE 2.39: Same as Figure 2.33 using cc-pVDZ+4p basis set.

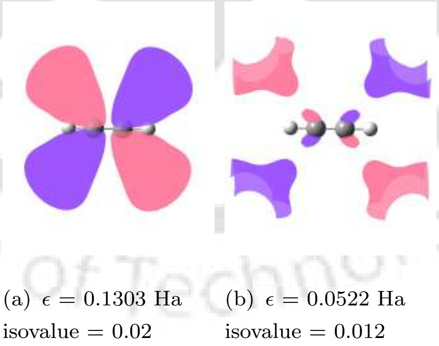
(a) $\epsilon = 0.1303$ Ha
isovalue = 0.02
(b) $\epsilon = 0.0522$ Ha
isovalue = 0.012

FIGURE 2.40: Same as Figure 2.33 using cc-pVDZ+3p basis set.

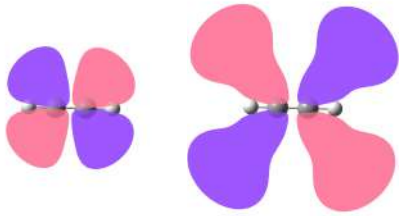

(a) $\epsilon = 0.1949$ Ha
isovalue = 0.02

(b) $\epsilon = 0.0961$ Ha
isovalue = 0.02

FIGURE 2.41: Same as Figure 2.33 using cc-pVDZ+2p basis set.

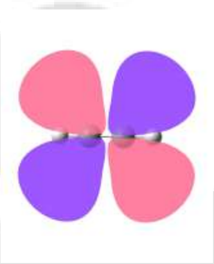

(a) $\epsilon = 0.1469$ Ha
isovalue = 0.02

FIGURE 2.42: Same as Figure 2 using cc-pVDZ+1p basis set.

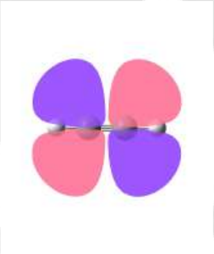

(a) $\epsilon = 0.2000$ Ha
isovalue = 0.02

FIGURE 2.43: Same as Figure 2.33 using cc-pVDZ basis set.

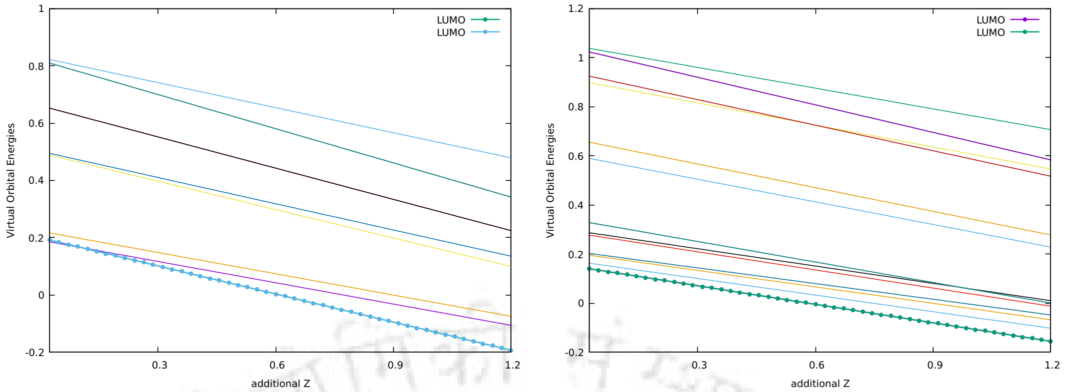

(a) cc-pVDZ (b) cc-pVDZ+1p

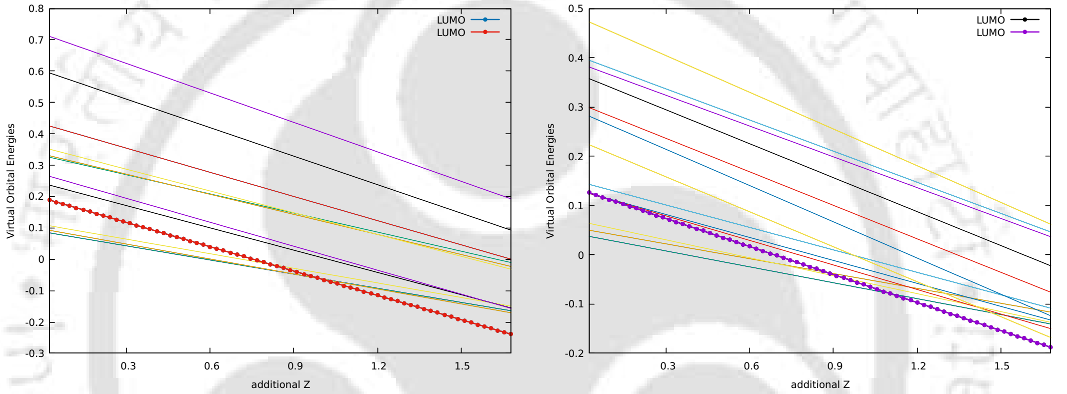

(c) cc-pVDZ+2p (d) cc-pVDZ+3p

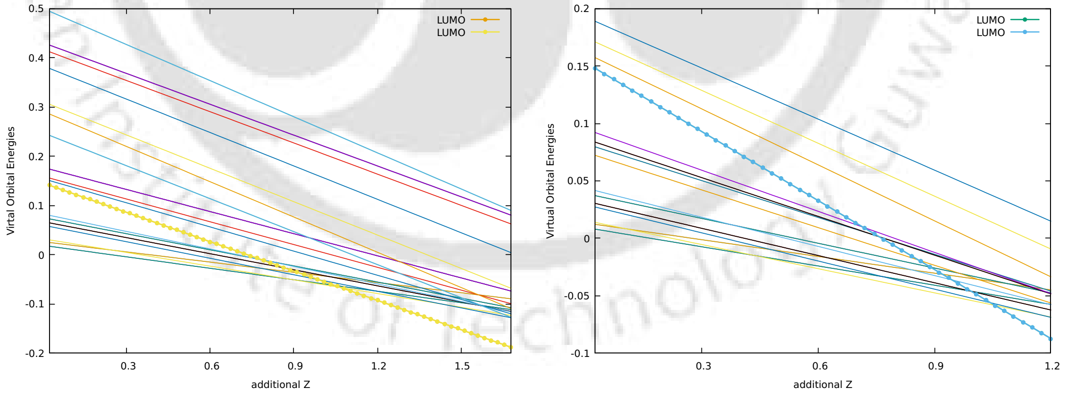

(e) cc-pVDZ+4p (f) cc-pVDZ+5p

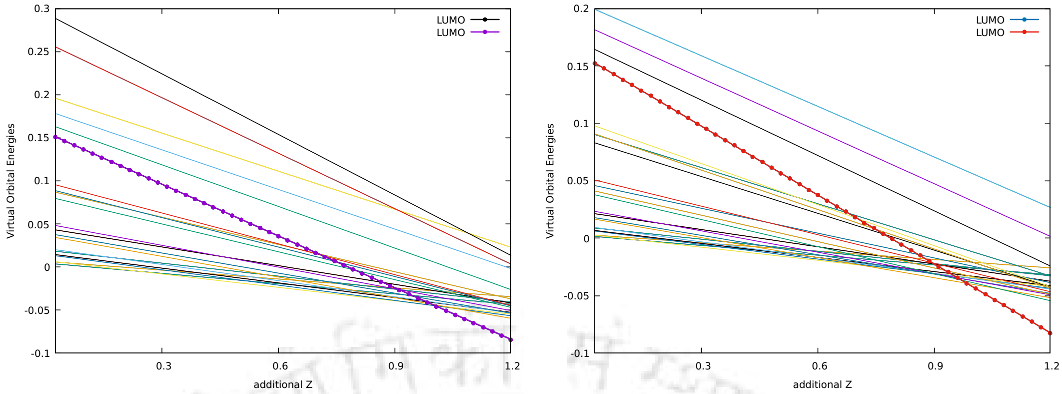

(g) cc-pVDZ+6p (h) cc-pVDZ+7p

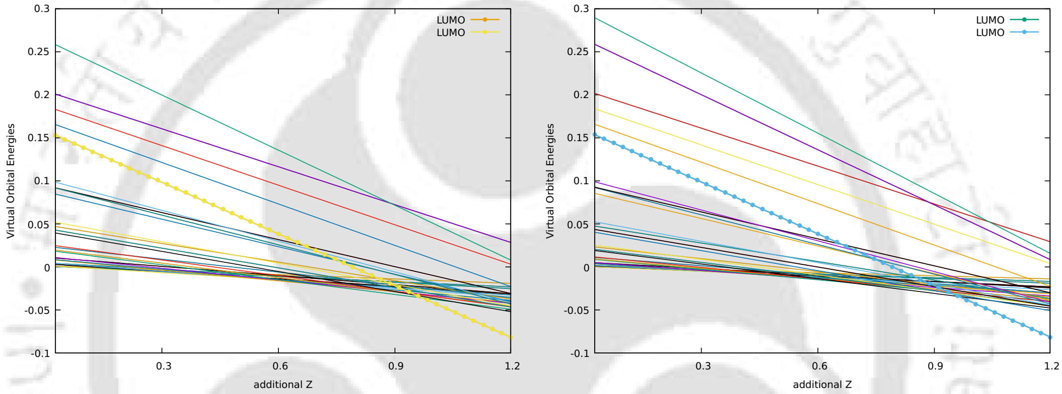

(i) cc-pVDZ+8p (j) cc-pVDZ+9p

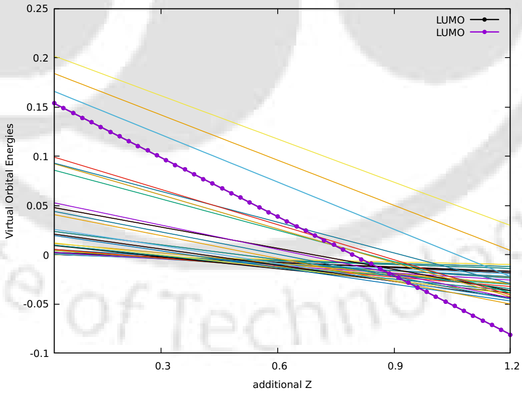

(k) cc-pVDZ+10p

Figure 2.44: Plot of the few lowest virtual orbital energies in Hartree (on the y-axis) as function of additional nuclear charge (on the x-axis) of neutral C_2H_2 molecule using cc-pVDZ+np basis set. The plot corresponds to modified PEM case I.

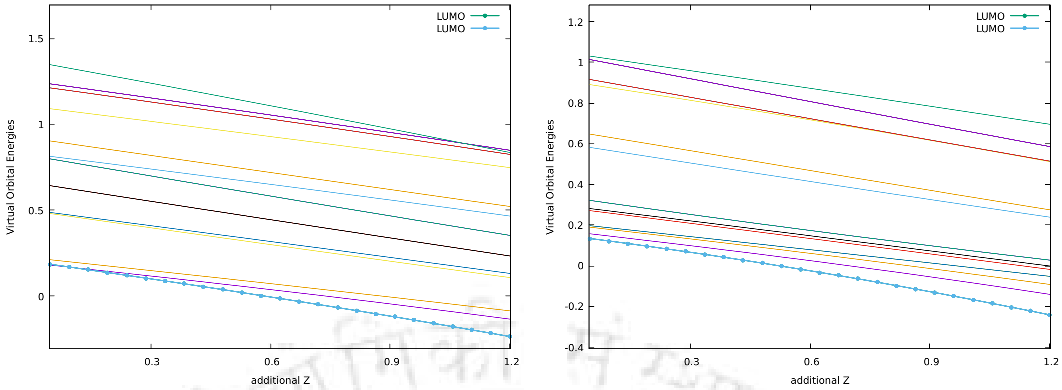

(a) cc-pVDZ (b) cc-pVDZ+1p

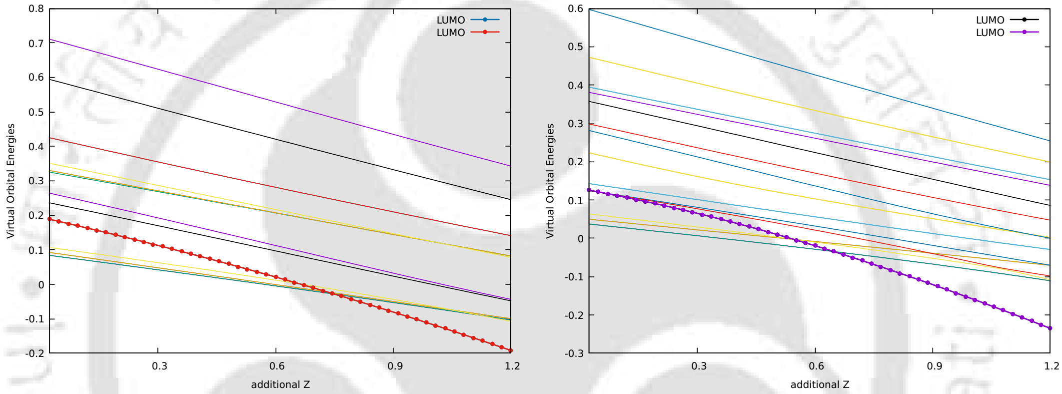

(c) cc-pVDZ+2p (d) cc-pVDZ+3p

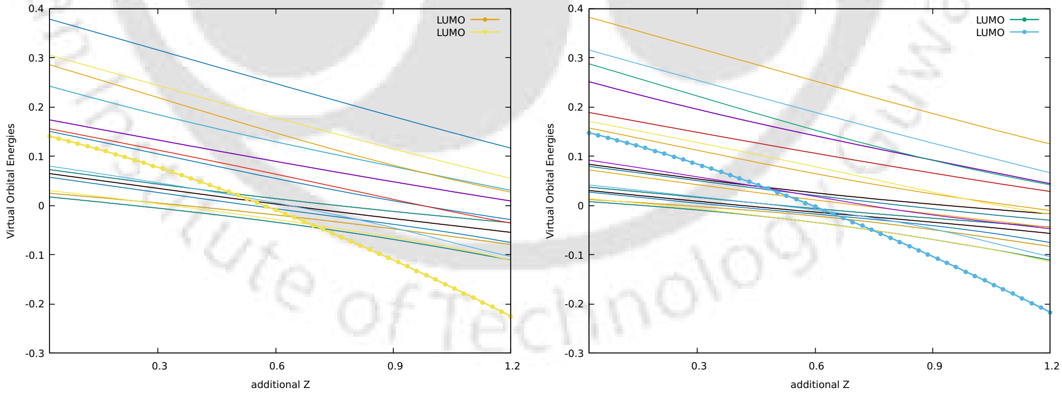

(e) cc-pVDZ+4p (f) cc-pVDZ+5p

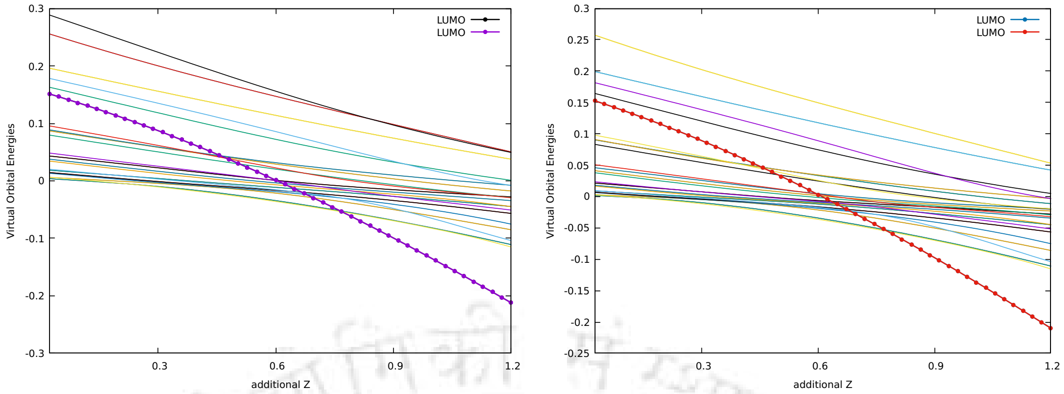

(g) cc-pVDZ+6p

(h) cc-pVDZ+7p

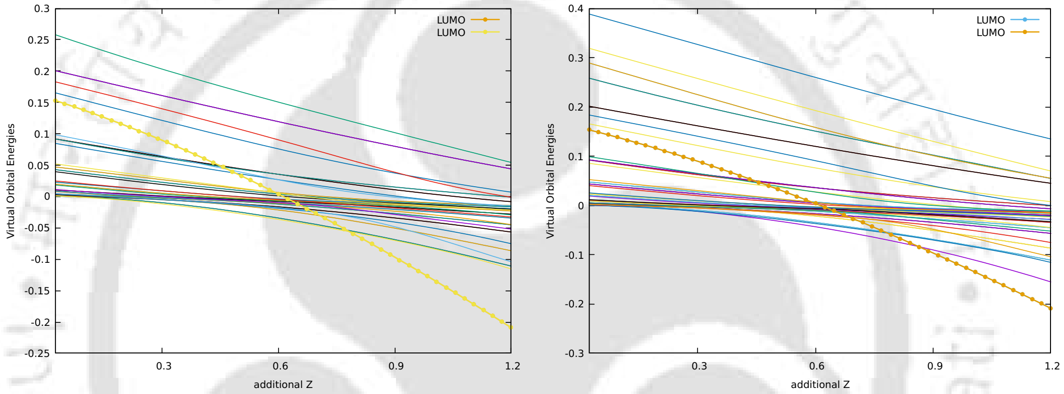

(i) cc-pVDZ+8p

(j) cc-pVDZ+9p

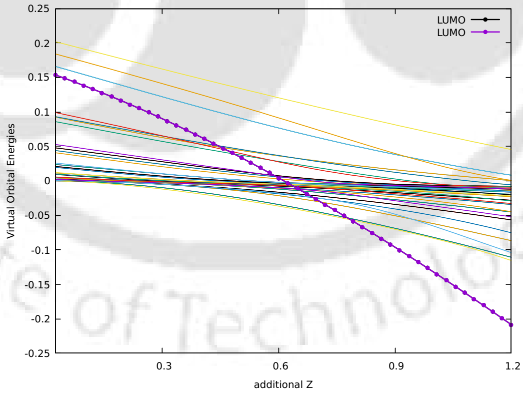

(k) cc-pVDZ+10p

FIGURE 2.45: Plot of the few lowest virtual orbital energies in Hartree (on the y-axis) as function of additional nuclear charge (on the x-axis) of neutral C_2H_2 molecule using cc-pVDZ+np basis set. The plot corresponds to modified PEM case II.

The LUMO orbital energies demonstrate convergence as additional p-type functions are introduced in the cc-pVDZ basis set. For cc-pVDZ+8p/9p/10p, the LUMO orbital energies are nearly identical (see table 2.5), and their orbital density plots also overlap (see fig 2.46). Lastly, calculations using different basis sets (i.e., 6-311G, cc-pVDZ, aug-cc-pVDZ, and aug-cc-pVTZ) with additional augmentation up to 10 p-type functions are performed. The true LUMO orbital energies are found to converge and are reported in Table 2.5.

TABLE 2.5: Orbital energies of identified LUMOs (in Hartree) of neutral C_2H_2 molecule using different basis sets upto extra augmentation of 10 p-type functions.

C_2H_2				
Augmentation	6-311G	cc-pVDZ	aug-cc-pVDZ	aug-cc-pVTZ
0p	0.1924	0.2001	0.1082	0.09274
1p	0.1463	0.1469	0.1401	0.1255
2p	0.0930	0.0961	0.1550	0.1401
3p	0.1270	0.1303	0.1621	0.1468
4p	0.1422	0.1456	0.1654	0.1498
5p	0.1490	0.1527	0.1669	0.1511
6p	0.1521	0.1559	0.1676	0.1517
7p	0.1535	0.1573	0.1678	0.1520
8p	0.1541	0.1579	0.1680	0.1521
9p	0.1543	0.1582	0.1680	0.1521
10p	0.1544	0.1583	0.1680	0.1521

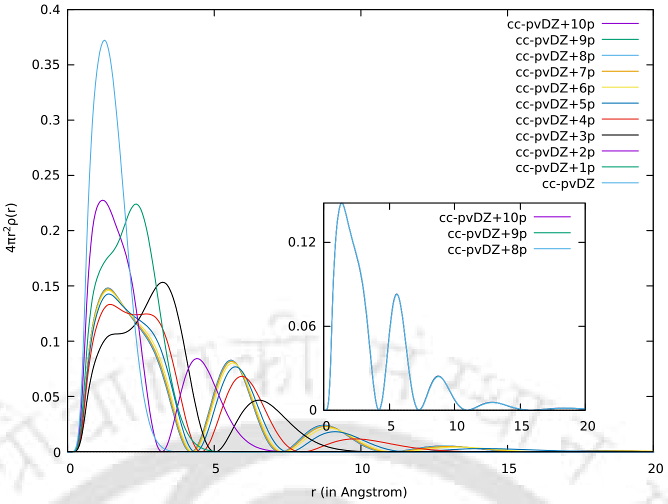

(a)

FIGURE 2.46: Plot of Orbital probability density (on the y-axis) vs r in angstrom (on the the x-axis) for true LUMO state of C_2H_2 using cc-pVDZ+np basis set.

2.3 Concluding Remarks

This chapter focuses on identifying the LUMO state accurately, which is crucial for electronic structure calculations to study electron-attached or electron-excited states. In most neutral molecule SCF calculations, the lowest empty MO undergoes changes in shape and becomes spatially large with the increase of diffuse basis functions in the basis set, making it unsuitable for the LUMO concept in chemistry. Therefore, when dealing with LUMO in calculations that involve diffuse basis functions, it is essential to be cautious and properly identify the desired orbitals to avoid any inaccuracies in further calculations. To identify the LUMO accurately, the PEM method, in conjunction with the nuclear charge stabilization method, is a reliable approach. The PEM approach is an innovative and accurate way to identify the LUMO state precisely as with this approach it becomes really easy to keep the track of every orbital. The inclusion of diffuse functions is essential for studying significant chemical phenomena, such as electron-attached or electron-excited states. The augmentation of extra basis functions introduces the same symmetry MOs, leading to avoided crossings in the charge stabilization curve, which makes it difficult to identify the true LUMO. With diagonalization approach, it is almost impossible to visualise avoiding crossings and to obtain the charge stabilization curve due to exchange of their behavior at these avoided crossings. However, with the help of PEM, it becomes achievable. The modified PEM is implemented in conjunction with nuclear charge stabilization to prevent the stabilization of the same symmetry MOs that are located far from the nucleus and precise identification of true LUMO is achieved. This modification of PEM is implemented in two scenarios, and both are effective at dealing with avoided crossings.

Chapter 3

Self-Consistent-Field Solution for Metastable Anions using Bound-State Method

3.1 Introduction

Molecules with a positive electron affinity (EA) form stable anions. It is straightforward to calculate the EA for these molecules (i.e., by taking the difference of energies of neutral and anionic species). However, for many molecules, no bound anion exists (i.e., metastable anion); experimentally, they have negative gas-phase EA. These anions are metastable states with a finite lifetime, often formed due to electron-molecule collisions[23, 24, 25, 26, 27]. These anions are also known as temporary anions. The temporary anion then decays by either losing an electron or through DEA [147, 25, 142]. The presence of temporary anions significantly influences chemical reactions by facilitating the formation and breaking of chemical bonds. When low-energy electrons ($E < 10$ eV) attach to specific sites in the DNA chain, they create transient negative ions (TNIs) which then undergo dissociative electron attachment (DEA), resulting in bond cleavage[148, 149].

The wave function of a true metastable state has an oscillating tail that extends to infinity. To accurately describe this tail, it's necessary to include diffuse functions in the basis set. However, quantum chemistry calculations face challenges when studying metastable anions, the conventional SCF calculation may converge to the lowest energy solution, with the excess electron occupying a diffuse molecular orbital present in the basis set. When using a highly diffuse basis set, the SCF solution may lead to the breakdown of the system into a neutral molecule with a free electron. This is known as variational collapse. It is not recommended to use the broken SCF solution for studying anions. If the SCF solution is applied in post-Hartree methods that consider electron correlation, it can result in inaccuracies and unreliable outcomes. This is because the initial approximation, the SCF solution, does not represent an anionic state but rather a neutral molecule plus a free electron. To accurately describe temporary anions or metastable states, an accurate SCF solution that describes the anionic state is necessary. It is suggested to use Green functions[150] or EOM-CCSD[151] theory for studying such states, as they are independent of the accuracy of HF orbitals of anions.

Several advanced methods have been developed to study metastable states. One such method involves the use of non-Hermitian quantum mechanics, which includes complex scaling[30, 31, 32, 33], Modified Smooth Exterior Scaling (MSES)[41, 42, 43], and complex-absorbing potential[36, 35, 34]. Another type of method involves the use of bound state calculations, i.e., conventional Hermitian quantum mechanics. This includes artificially binding an extra electron, which can be accomplished by using a compact basis set or introducing a potential wall[81, 82] to capture the electron inside. Additionally, it also includes stabilization methods and extrapolation methods are used to describe the metastable states.

Here, the nuclear charge stabilization technique has been combined with the PEM method. The PEM method is efficient in keeping track of the order of orbitals and orbital energies, as the line number of a particular state remains fixed. In this method, the process starts with the nuclear charge value where the anion is bound, and then decrease the nuclear charge to zero using PEM, which keeps the Singly Occupied Molecular Orbital (SOMO) fixed at each nuclear charge value. However, increasing the number of diffuse basis functions in the basis set results in the presence of the MOs as same symmetry of SOMO, leading to the introduction of avoided crossings of such states with SOMO. There is an exchange of behavior at these avoided crossings, which will result in the extra electron being placed into the lowest energy diffuse MO of the same symmetry as SOMO, leading to a break in the SCF solution. To avoid such situations and to obtain an accurate SCF solution for metastable anions, the interaction of these states is ignored in the PEM equation, as discussed in detail in this chapter. Using this technique, an SCF solution for anions, where the excess electron is in a valence state rather than in a diffuse state, is achieved. The solution obtained using the modified PEM is checked for being self-consistent-field solution, confirming the accuracy of the method. In this chapter, efforts have been made to obtain the SCF solution for the $C_2H_4^-$, N_2^-, $C_2H_2^-$ and $HCHO^-$ anionic species using the PEM in conjunction with nuclear charge stabilization method.

3.1.1 Results and Discussion

All quantum chemistry calculations are performed using the Molgw[143] package with modification, including the PEM subroutine. All calculations are performed using Cartesian Gaussian functions. As to generate the wfn file from Molgw software, it is necessary to use Cartesian Gaussian functions. Additionally, all orbital probability density plots are obtained using the Multiwfn software[145]. In this chapter, all the calculations are carried out using the UHF approach.

3.1.2 Ethylene anion ($C_2H_4^-$)

It's important to note that for metastable anions, only compact basis sets yield a reliable SCF solution; otherwise, the system may converge to a neutral molecule and a electron in the most diffuse MO present in the basis set. In the 6-311G and cc-pVDZ basis sets, the analysis showed that the SOMO looks like a $\pi^\star$ antibonding character and well localized near the nucleus as seen in their orbital probability density plot (see Figure 3.1). While, in aug-cc-pVDZ and higher basis sets, the SOMO appears as having a $\pi^\star$ antibonding character but a major peak lies far from the nucleus in their orbital probability density plot (see Figure 3.1). This is possible due to the mixing of higher energy $\pi^\star$ states. The corresponding orbital pictures

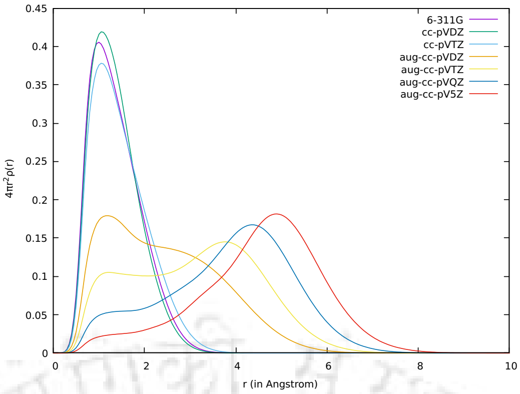

FIGURE 3.1: Plot of Orbital probability density (on the y-axis) vs r in angstrom (on the the x-axis) for SOMO of $C_2H_4^-$ using different basis sets.

for SOMO using different basis sets (i.e. 6-311G, cc-pVDZ, cc-pVTZ, aug-cc-pVDZ, aug-cc-pVTZ, aug-cc-pVQZ and aug-cc-pV5Z) are shown in Fig 3.2.

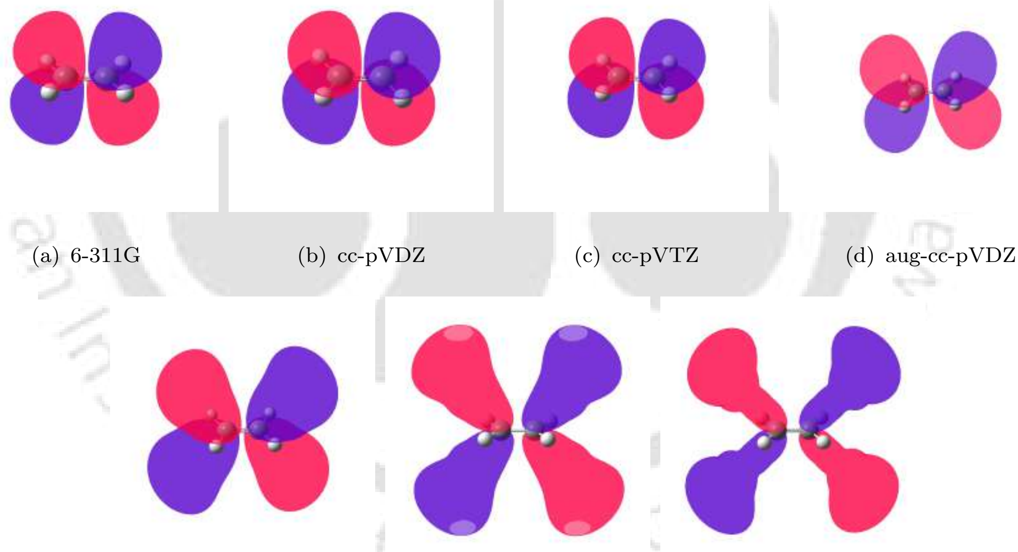

(a) 6-311G (b) cc-pVDZ (c) cc-pVTZ (d) aug-cc-pVDZ

(e) aug-cc-pVTZ (f) aug-cc-pVQZ (g) aug-cc-pV5Z

FIGURE 3.2: SOMO's orbital picture for different basis sets (i.e. 6-311G, cc-pVDZ, aug-cc-pVDZ, aug-cc-pVTZ and aug-cc-pVQZ) for $C_2H_4^-$. These orbital pictures corresponds to SCF solution at z = 0 without implementing PEM.

The total HF and MP2 energies obtained using these different basis sets are provided in Table 3.1. The vertical electron affinity is calculated at both HF and MP2 level

Table 3.1: HF and MP2 energies of neutral and anionic C_2H_4 using different basis sets. Vertical electron affinities at HF and MP2 level are represented as Δ^{HF} and Δ^{MP2} respectively in eV.

Basis Set	HF-Anion(a.u.)	HF-neutral(a.u.)	MP2-Anion(a.u.)	MP2-Neutral(a.u.)	Δ^{HF}(eV)	Δ^{MP2}(eV)
6-311G	-77.8928	-78.0184	-78.1133	-78.2442	-3.42	-3.56
cc-pVDZ	-77.9079	-78.0398	-78.2018	-78.3260	-3.59	-3.38
cc-pVTZ	-77.9457	-78.0635	-78.3384	-78.4374	-3.21	-2.69
aug-cc-pVDZ	-77.9488	-78.0434	-78.2705	-78.3438	-2.58	-1.99
aug-cc-pVTZ	-77.9761	-78.0644	-78.3875	-78.4537	-2.40	-1.89
aug-cc-pVQZ	-77.9880	-78.0690	-78.4374	-78.5060	-2.20	-1.86

of theory (see Table 3.1), where, Vertical electron affinity is defined as

$$\Delta = E_{Neutral} - E_{anion} \tag{3.1}$$

The difficulty arises when heavily diffuse basis set is used to study the metastable anion; in that case, the SCF solution for the corresponding anion collapses into a neutral molecule, and an electron in the most diffuse MO present in the basis set. This difficulty is overcome by using the PEM in conjunction with the nuclear charge stabilization method to obtain meaningful SCF solution for metastable anionic species. By increasing the nuclear charge beyond a certain value, a metastable anion becomes a bound anion for which the SCF solution does not collapse. Therefore, this approach begins with the bound anion and utilizes the PEM method to achieve the corresponding SCF solution at z = 0. A fixed occupation number for the orbital corresponding to the SOMO is maintained throughout the PEM calculation, which means once the electron at a higher nuclear charge is in a bound state, the same state will remain occupied at z = 0. This way, the corresponding meaningful SCF solutions for temporary anions can be obtained using the PEM calculation. Previous research[152, 153] has demonstrated that the results obtained from the PEM and via diagonalization are in excellent agreement. This has been confirmed by studying the $C_2H_4^-$ with compact basis sets and higher basis sets such as aug-cc-pVDZ, aug-cc-pVTZ, and aug-cc-pVQZ, revealing that the solutions at z = 0 using PEM and SCF calculation at z = 0 are exactly the same to an accuracy of the 5th decimal place. The corresponding charge stabilization plots of comparison between diagonalization and PEM are shown in Fig 3.3.

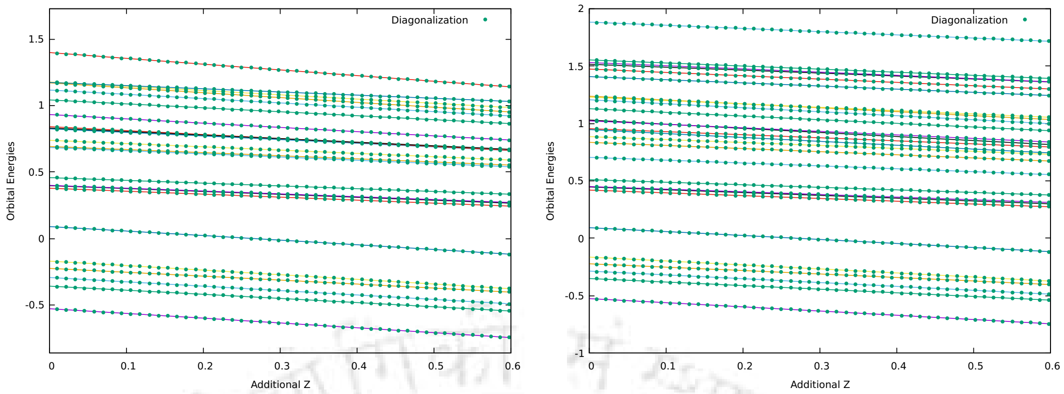

(a) 6-311G (b) cc-pVDZ

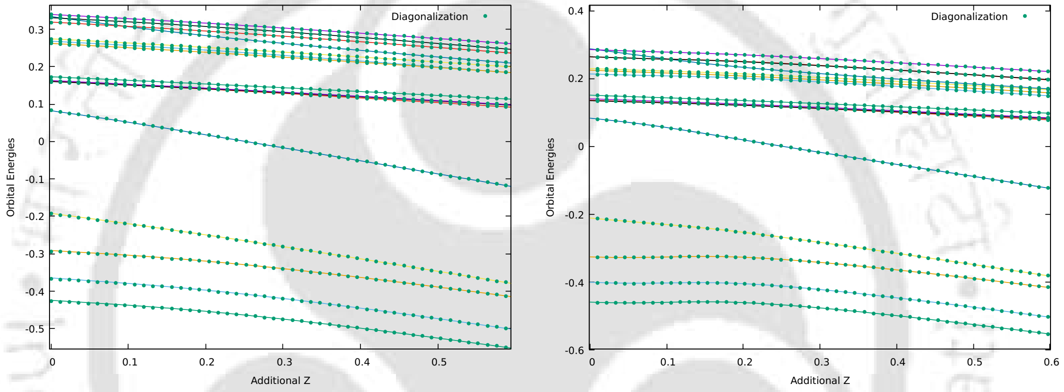

(c) aug-cc-pVDZ (d) aug-cc-pVTZ

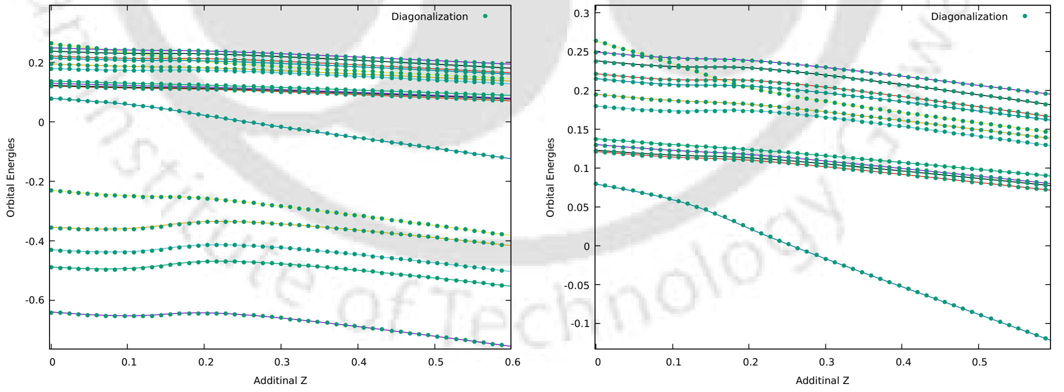

(e) aug-cc-pVQZ (f) aug-cc-pVQZ

FIGURE 3.3: Plot of the orbital energies in Hartree (on y-axis) as function of additional nuclear charge (on x-axis) of $C_2H_4^-$ using diffrent basis sets (i.e. 6-311G, cc-pVDZ, aug-cc-pVDZ, aug-cc-pVTZ and aug-cc-pVQZ). f) Zoom in on the aug-cc-pVDZ results to clearly see the avoided crossing. The PEM solution agrees well with diagonalization results (represented by green dots). These solutions correspond to the SCF solution for anions obtained by diagonalization and the PEM-based approach.

It is essential to include diffuse basis functions when studying metastable anions. In this research, cc-pVDZ+np basis set is employed, where p-type functions are added incrementally by multiplying them with half the smallest exponent present in the already prepared basis set. The PEM in conjunction with charge stabilization method is performed to obtain a meaningful SCF solution for the anion at z = 0. Increasing the number of diffuse basis functions leads to an increase in the same symmetry MOs, leading to more states involved in avoided crossings with SOMO. At each avoided crossing, there is an exchange of behavior taking place. This means that starting with the correct orbital at a higher z value, at the avoided crossing, the extra electron moves into a different orbital (i.e., the most diffuse orbital) but with the same symmetry as SOMO. The charge stabilization plots, in Figure 3.4, clearly show that two different paths are followed with the increase in additional p-type functions. One path occurs when the anion is in the bound region, and at the avoided crossing, there is sudden change (i.e., a downward bump) leading to a different path with respect to variation in z. This change in the path happens because the electron is present in a diffuse molecular orbital now, even though it starts from the correct SOMO, due to the exchange of behavior. Also, it's interesting to note that the orbital energies of the occupied orbitals also follow two distinct paths with respect to variations in z. In the region where the anion is bound, the electron is in the correct orbital. In the region where the anion is unbound, the solution collapses into a neutral molecule, and an extra electron occupies a diffuse molecular orbital, leading to a separate path even for the occupied orbital energies with respect to variation in z. The corresponding charge stabilization plot for cc-pVDZ-0p to cc-pVDZ+10p basis sets are shown in Figure 3.4.

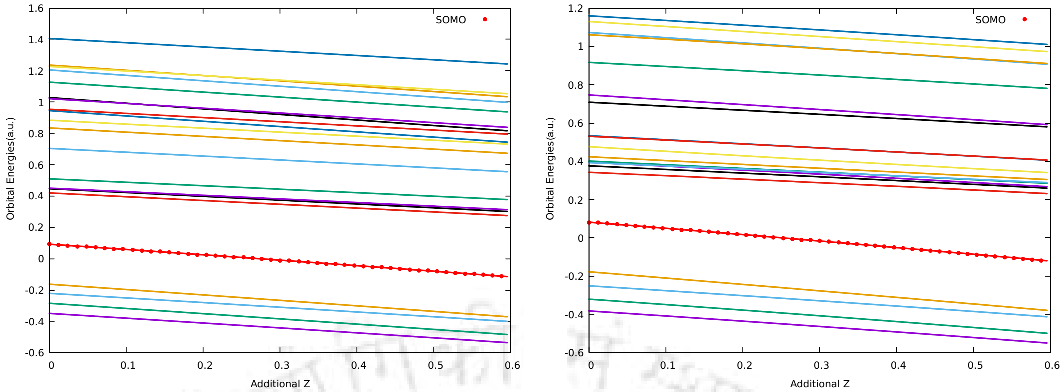

(a) cc-pVDZ (b) cc-pVDZ+1p

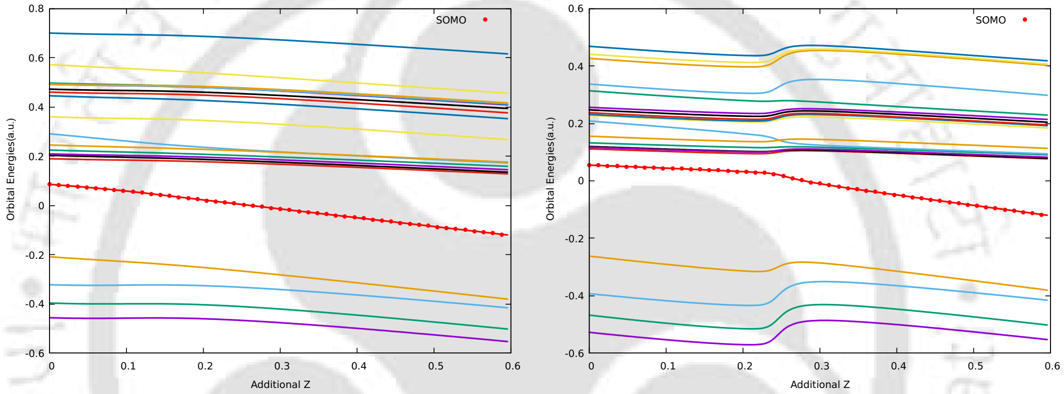

(c) cc-pVDZ+2p (d) cc-pVDZ+3p

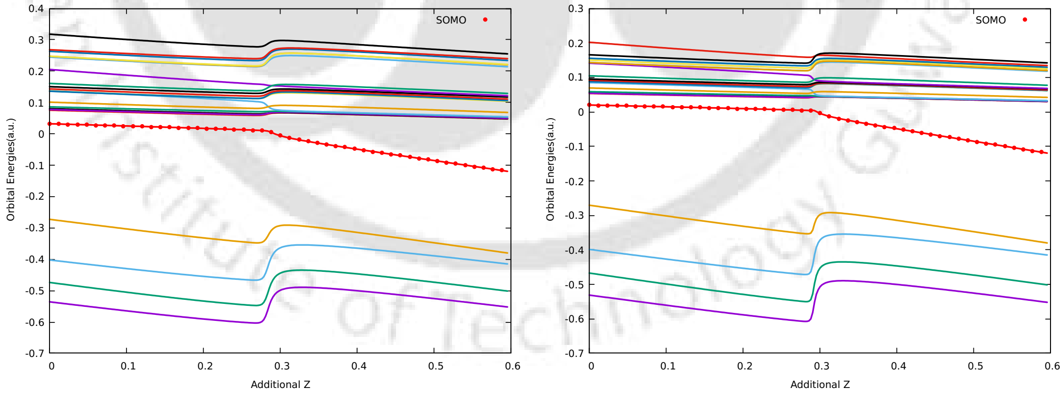

(e) cc-pVDZ+4p (f) cc-pVDZ+5p

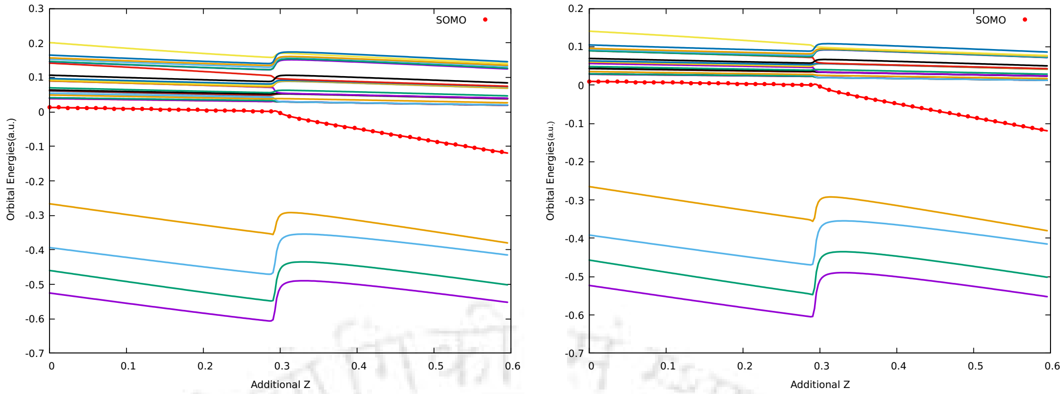

(g) cc-pVDZ+6p

(h) cc-pVDZ+7p

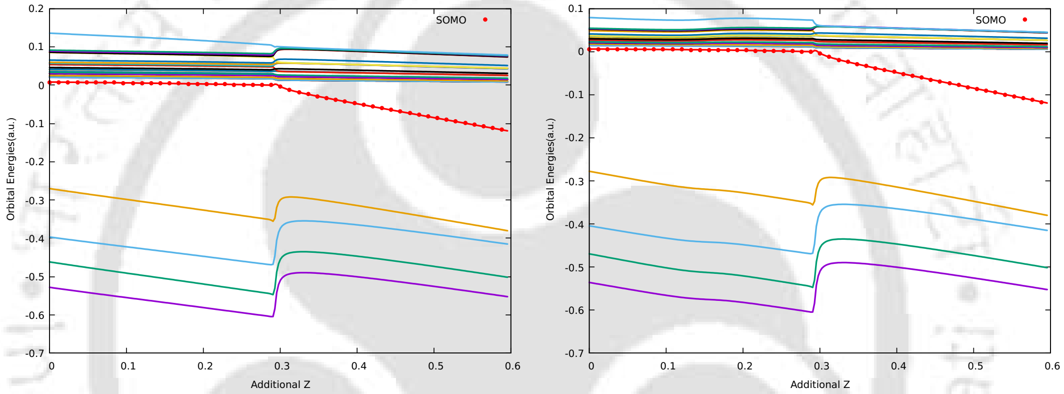

(i) cc-pVDZ+8p

(j) cc-pVDZ+9p

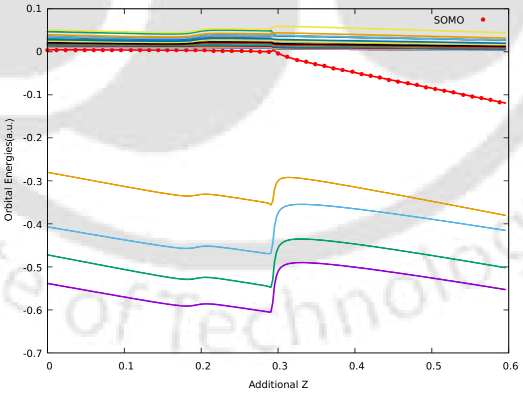

(k) cc-pVDZ+10p

FIGURE 3.4: Plot of the orbital energies in Hartree (on the y-axis) as function of additional nuclear charge (on the x-axis) of $C_2H_4^-$ molecule using cc-pVDZ+np basis set. These charge stabilization plots are obtained by using the PEM calculations without modification.

The probability densities for the corresponding SOMOs are plotted using cc-pVDZ+np basis set and are shown in Figure 3.5. Upon examining the plot, it becomes clear that the increase in the p-type function in the basis set SOMO is localized farther and farther from the nucleus. For cc-pVDZ+9p/10p, the position of the peak is at more than 50 Å and has a very low amplitude. Therefore, it won't be visible in Figure 3.5 and hence not included in the figure. Therefore, this anionic solution cannot be taken into account, and modification of the PEM is necessary to obtain a stable solution for the metastable anion, which can be further used in post-SCF calculations.

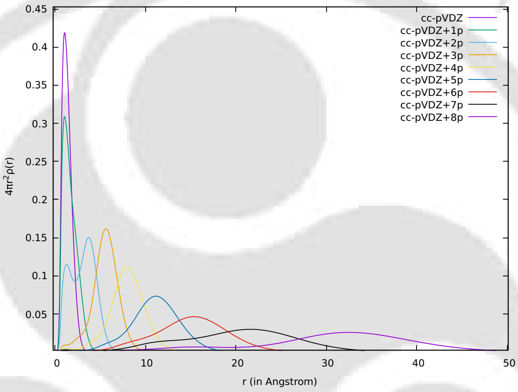

FIGURE 3.5: Plot of Orbital probability density (on the y-axis) vs r in angstrom (on the the x-axis) for SOMO of $C_2H_4^-$ using cc-pVDZ+np basis set, with the additional nuclear charge set to zero.

The modification involves the removing of the interaction between the states involved in avoided crossing from the c-matrix in PEM equation. It is achieved by removing of the interaction between the states involved in avoided crossing from Eq. 1.26, which means index j is not equal to those nearby states, which leads to avoided crossing when index i represents the SOMO state. Initially normal PEM calculations (i.e. without any modifications) are carried out for a series of additional Z value and some exchange of behavior with true SOMO state is observed. Looking at their orbital character, these states are found to have same character as true SOMO. So, these states are removed from eq 1.26 manually throughout the calculations.

In this study, the modified PEM calculations for several basis sets from cc-pVDZ to cc-pVDZ+10p is performed by removing the interaction among states involved in avoided crossing with SOMO. For example, cc-pVDZ+7p, normal PEM calculation(i.e., without modifications) shows that there is a break in the SCF solution due to the exchange of behavior with the true SOMO. Upon plotting the orbitals pictures of these states involved in the exchange of behavior are found to be diffuse states with $\pi^\star$ antibonding character. So, the interaction of these states are now removed from the PEM equation as described earlier, and the modified PEM calculation is performed. The first step is to identify the diffuse states having the same symmetry as true SOMO at a higher nuclear charge value, and the second step is to remove the interaction of these states with true SOMO in Eq. 1.26. The second step is done manually at higher Z where anion is bound, and then the PEM calculation is performed till the value of additional Z reaches 0. Now, the SCF solution is not breaking due to the exchange of behavior as the exchange of behavior is not taking place, and the meaningful SCF solution at z = 0 is achieved with the extra electron being present in the localized state rather than in the diffuse state. The corresponding charge stabilization plot for cc-pVDZ-0p to cc-pVDZ+10p basis sets are shown in Figure 3.6.

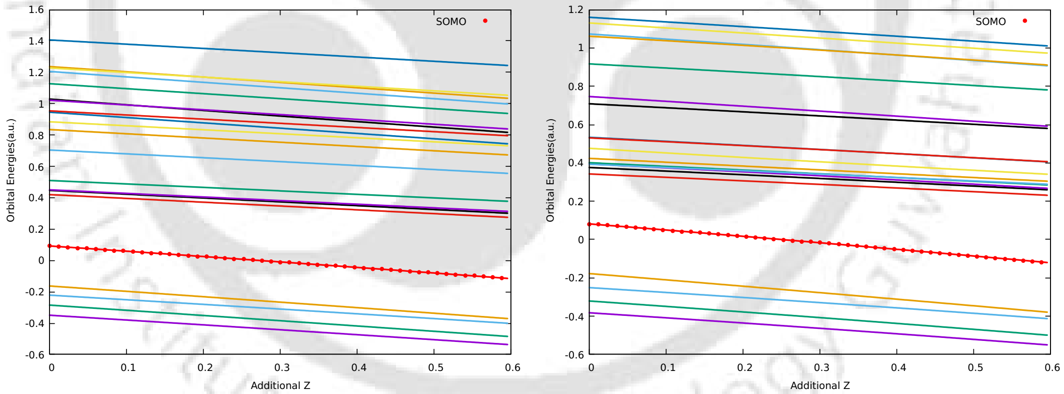

(a) cc-pVDZ (b) cc-pVDZ+1p

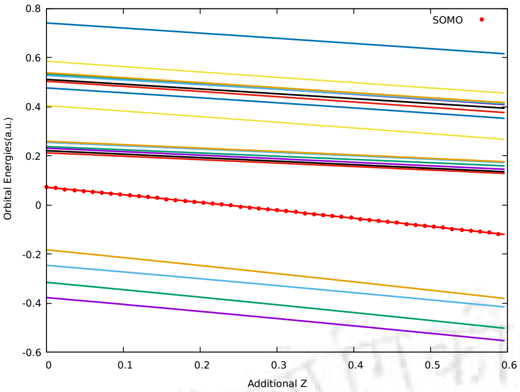

(c) cc-pVDZ+2p

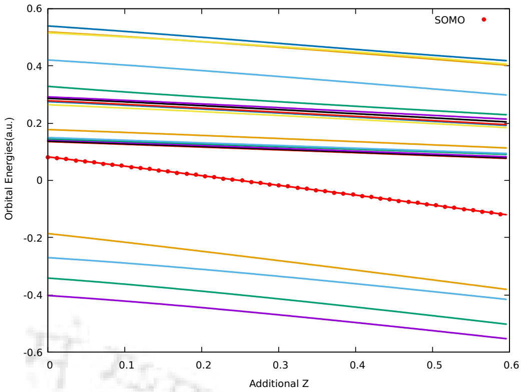

(d) cc-pVDZ+3p

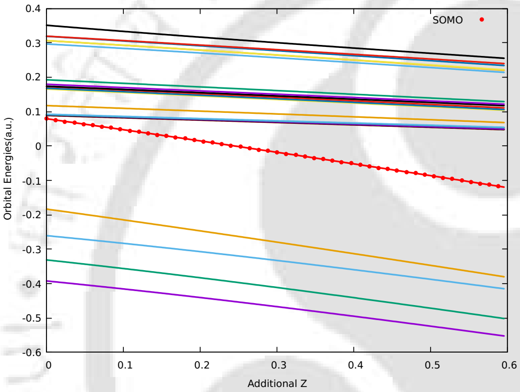

(e) cc-pVDZ+4p

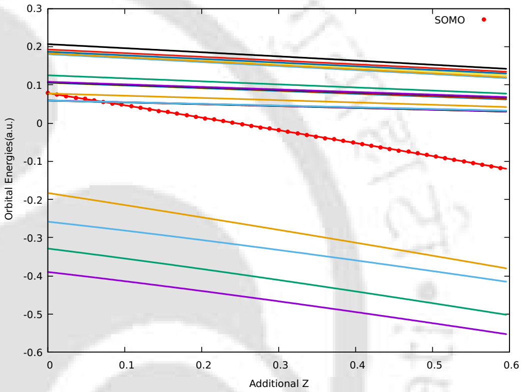

(f) cc-pVDZ+5p

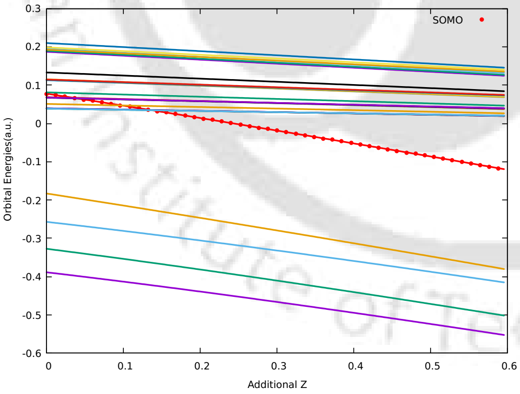

(g) cc-pVDZ+6p

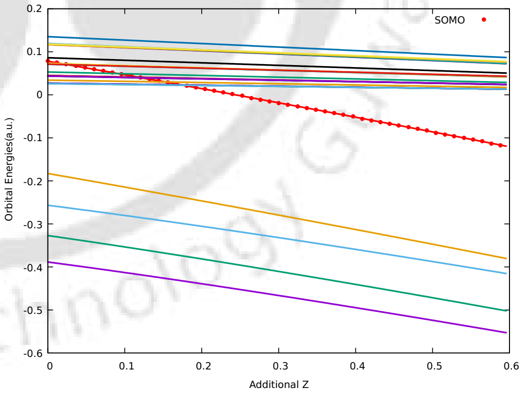

(h) cc-pVDZ+7p

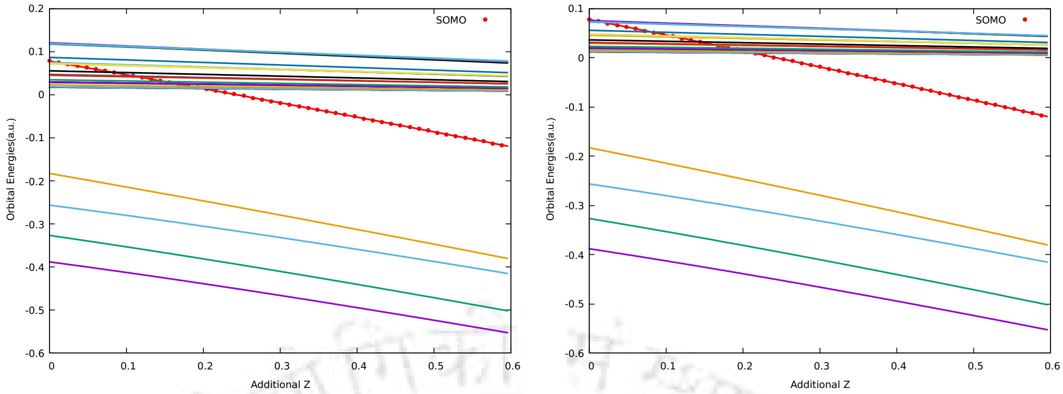

(i) cc-pVDZ+8p

(j) cc-pVDZ+9p

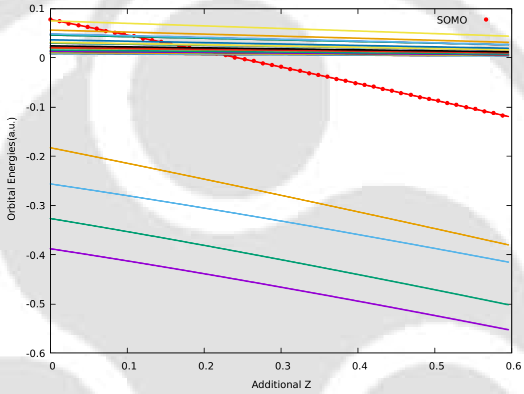

(k) cc-pVDZ+10p

FIGURE 3.6: Plot of the orbital energies in Hartree (on the y-axis) as function of additional nuclear charge (on the x-axis) of $C_2H_4^-$ using cc-pVDZ+np basis set. These charge stabilization plots are obtained by applying modified PEM.

To validate the accuracy of the solution obtained from the modified PEM calculation, the Fock matrix is constructed using C' obtained from the PEM and the ϵ matrix is calculated as

$$\epsilon = (C')^T F' C'. \tag{3.2}$$

The obtained ϵ matrix is "nearly" diagonal, and on diagonal elements, it contains the orbital energies the same as obtained by the PEM calculation, hence confirming the self-consistent-field solution at each value of the additional nuclear charge. In Figure 3.7(a)-3.7(d), orbital energies obtained using PEM and the corresponding diagonal value of ϵ matrix are plotted and found to be indistinguishable. The off diagonal terms of ϵ-matrix are in order of 10^{-4}. The value of off diagonal elements can be interpreted as the error in the PEM calculations for obtaining SCF results. In all cases, orbital corresponds to SOMO is found to have $\pi^\star$ character, which is well localized near the nucleus and can also be confirmed by orbital probability density (i.e. shown in Figure 3.8).

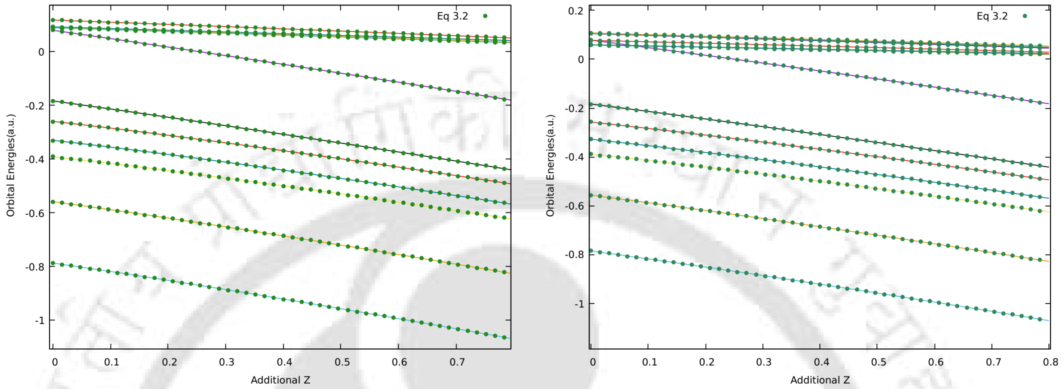

(a) cc-pVDZ+4p

(b) cc-pVDZ+5p

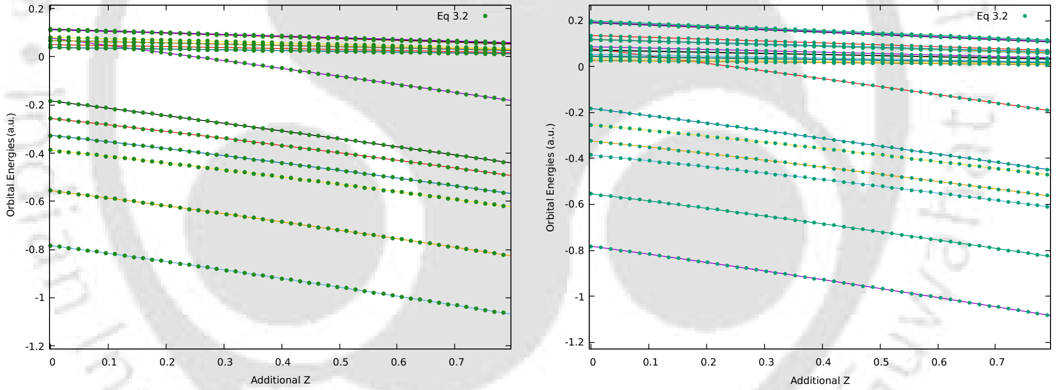

(c) cc-pVDZ+6p

(d) cc-pVDZ+7p

FIGURE 3.7: Plot of the orbital energies in Hartree (on the y-axis) as function of additional nuclear charge (on the x-axis) of $C_2H_4^-$ using cc-pVDZ+4p/5p/6p/7p basis sets. These charge stabilization plots are obtained by applying modified PEM. Figures a-d shows that results obtained from modified PEM and from the ϵ-matrix (i.e. from equation 3.2) are indistinguishable

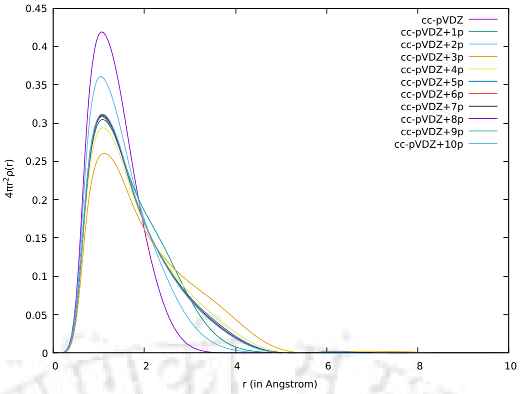

FIGURE 3.8: Plot of Orbital probability density (on the y-axis) vs r in angstrom (on the the x-axis) for SOMO of $C_2H_4^-$ using cc-pVDZ+np basis set. These plots are obtained after applying the modified PEM. In all cases electron density is much localized near to the nucleus.

Once the meaningful SCF solution for metastable anion is obtained, to incorporate the electron correlation, MP2 calculations are performed and the results are included in Table 3.2. Their vertical electron affinity is calculated and is also included in Table 3.2. It is found that the results are getting converged with increase in the number of diffuse functions (i.e., p-type functions).

TABLE 3.2: HF and MP2 energies for neutral and anionic C_2H_4 using cc-pVDZ+np sets. Vertical electron affinities at HF and MP2 level are represented as Δ^{HF} and Δ^{MP2} respectively in eV.

Basis Set	HF-Anion(a.u.)	HF-neutral(a.u.)	MP2-Anion(a.u.)	MP2-Neutral(a.u.)	Δ^{HF}(eV)	Δ^{MP2}(eV)
cc-pVDZ	-77.9076	-78.0398	-78.2015	-78.3260	-3.59	-3.38
cc-pVDZ+1p	-77.9317	-78.0413	-78.2341	-78.329	-2.98	-2.58
cc-pVDZ+2p	-77.9315	-78.0418	-78.2337	-78.3306	-3.00	-2.63
cc-pVDZ+3p	-77.9394	-78.0419	-78.2450	-78.3310	-2.78	-2.34
cc-pVDZ+4p	-77.9371	-78.0419	-78.2424	-78.3313	-2.85	-2.42
cc-pVDZ+5p	-77.9363	-78.0419	-78.2415	-78.3313	-2.87	-2.44
cc-pVDZ+6p	-77.9360	-78.0419	-78.2411	-78.3314	-2.88	-2.45
cc-pVDZ+7p	-77.9359	-78.0419	-78.2409	-78.3314	-2.88	-2.46
cc-pVDZ+8p	-77.9358	-78.0419	-78.2408	-78.3314	-2.88	-2.46
cc-pVDZ+9p	-77.9358	-78.0419	-78.2408	-78.3314	-2.88	-2.46
cc-pVDZ+10p	-77.9358	-78.0419	-78.2408	-78.3314	-2.88	-2.46

As mentioned earlier in the discussion that, SOMO corresponding to aug-ccpVDZ, aug-cc-pVTZ, aug-cc-pVQZ, and higher basis sets calculation have mixed characters, and a major peak is located far from the nucleus in their orbital probability density plot. So, the modified PEM calculations are performed by ignoring the interaction between avoided crossing states to get a meaningful SCF solution corresponding to these basis sets. The orbital probability densities for their corresponding SOMOs that they are now well localized near the nucleus, as evident from their orbital probability plot shown in Figure 3.9 and corresponding SOMOs shown in Figure 3.10. Their total HF and MP2 energies are recorded, and the vertical electron affinity is calculated and tabulated in Table 3.3.

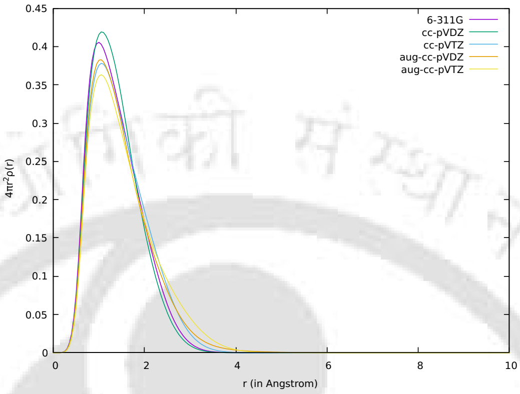

FIGURE 3.9: Plot of Orbital probability density (on the y-axis) vs r in angstrom (on the the x-axis) for SOMO of $C_2H_4^-$ using different basis sets. These plots are obtained after applying the modified PEM.

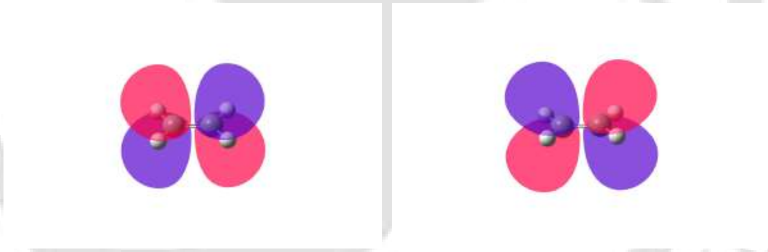

(a) aug-cc-pVDZ (b) aug-cc-pVTZ

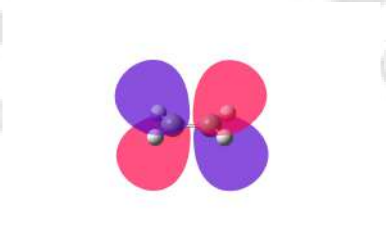

(c) aug-cc-pVQZ

FIGURE 3.10: SOMO's orbital picture for different basis sets (i.e. aug-cc-pVDZ, aug-cc-pVTZ and aug-cc-pVQZ) for $C_2H_4^-$. These orbital pictures corresponds to SCF solution obtained by applying the modified PEM.

Table 3.3: HF and MP2 energies of neutral and anionic C_2H_4 using aug-cc-pVDZ, aug-cc-pVTZ, and aug-cc-pVQZ basis sets. Vertical electron affinities at HF and MP2 level are represented as Δ^{HF} and Δ^{MP2} respectively in eV. The results correspond to the SCF solution after applying modified PEM.

Basis Set	HF-Anion(a.u.)	HF-neutral(a.u.)	MP2-Anion(a.u.)	MP2-Neutral(a.u.)	Δ^{HF}(eV)	Δ^{MP2}(eV)
aug-cc-pVDZ	-77.9331	-78.0434	-78.2518	-78.3438	-3.00	-2.50
aug-cc-pVTZ	-77.9567	-78.0644	-78.3731	-78.4537	-2.93	-2.29
aug-cc-pVQZ	-77.9629	-78.0690	-78.4247	-78.5060	-2.88	-2.21

Now that a meaningful SCF solution for metastable anions has been achieved, several additional calculations were performed using different basis sets with extra augmentation to obtain a meaningful SCF solution by applying the modified PEM and the vertical electron affinities are calculated. The MP2 (post-SCF) calculations are performed to incorporate the electron correlation effect. The value of S^2 was found to be in the range of 0.76-0.77 in all cases, which is close to the expected value of 0.75 for one unpaired electron. The results obtained from different basis sets are reported in Table 3.4 and are found to be in agreement with experimental result.

Table 3.4: HF and MP2 energies of neutral and anionic C_2H_4 for different basis sets. Experimental result is included for comparison of calculated vertical electron affinities.

Basis Set	HF-Anion(a.u.)	HF-neutral(a.u.)	MP2-Anion(a.u.)	MP2-Neutral(a.u.)	Δ^{HF}(eV)	Δ^{MP2}(eV)
cc-pVDZ+8p	-77.9358	-78.0419	-78.2408	-78.3314	-2.88	-2.46
aug-cc-pVDZ+5p	-77.9371	-78.0434	-78.2599	-78.3445	-2.88	-2.30
aug-cc-pVDZ+7p	77.9378	-78.0434	-78.2598	-78.3445	-2.87	-2.30
aug-cc-pVDZ+5s5p	-77.9376	-78.0435	-78.2602	-78.3448	-2.88	-2.30
aug-cc-pVTZ+5p	-77.9610	-78.0645	-78.3794	-78.4576	-2.81	-2.13
aug-cc-pVQZ+5p	-77.9670	-78.0689	-78.4247	-78.5005	-2.77	-2.06
aug-cc-pV5Z+4p	-77.9692	-78.0681	-78.4467	-78.5190	-2.69	-1.97
Experimental Result[154]	-1.80 eV					

3.1.3 Acetylene anion ($C_2H_2^-$), Dinitrogen anion (N_2^-) and Formaldehyde anion ($HCHO^-$)

Similar methodology is also employed to study N_2^-, $C_2H_2^-$ and $HCHO^-$ anionic species. For these species, three basis sets (aug-cc-pVDZ+5p, aug-cc-pVTZ+5p, and aug-cc-pVQZ+5p) are employed, and the modified PEM calculation, in conjunction with nuclear charge, is performed in each case. The value of S^2, is found to be in the range of 0.76-0.78 in all cases, which is close to 0.75 corresponding to one unpaired electron. MP2 calculations are performed in each case to incorporate electron correlation. The corresponding vertical electron affinities are calculated and are tabulated in Table 3.5. The results obtained are in good agreement with the experimental results.

TABLE 3.5: HF and MP2 energies of neutral and anionic C_2H_2, N_2, and HCHO for different basis sets. Experimental results are included for comparison of calculated vertical electron affinities.

Basis Set	HF-Anion(a.u.)	HF-neutral(a.u.)	MP2-Anion(a.u.)	MP2-Neutral(a.u.)	Δ^{HF}(eV)	Δ^{MP2}(eV)
$C_2H_2^-$						
aug-cc-pVDZ+5p	-76.7023	-76.8299	-76.9962	-77.1077	-3.44	-3.03
aug-cc-pVTZ+5p	-76.7287	-76.8508	-77.1149	-77.2181	-3.32	-2.80
aug-cc-pVQZ+5p	-76.7381	-76.8547	-77.1658	-77.2647	-3.17	-2.69
Experimental Result						
Experiment vib. excit.[155]	-2.6 eV					
Experiment vib. excit.[156]	-2.5 eV					
Experiment transmission[157]	-2.6 eV					
Experiment DEA[158]	-2.95 eV					
N_2^-						
aug-cc-pVDZ+5p	-108.8537	-108.9620	-109.1879	-109.2936	-2.95	-2.87
aug-cc-pVTZ+5p	-108.8804	-108.9870	-109.3127	-109.4089	-2.90	-2.62
aug-cc-pVQZ+5p	-108.8889	-108.9932	-109.3844	-109.4740	-2.84	-2.44
Experimental Result[159]	-2.32 eV					
$HCHO^-$						
aug-cc-pVDZ+5p	-113.8230	-113.8856	-114.1888	-114.2365	-1.70	-1.29
aug-cc-pVTZ+5p	-113.8536	-113.9142	-114.3236	-114.3659	-1.65	-1.15
aug-cc-pVQZ+5p	-113.8621	-113.9212	-114.3898	-114.4296	-1.61	-1.08
Experimental Result						
Electron transmission[160, 161]	-1.0/-0.86					
Vibrational excitation[162]	-0.87					

3.2 Concluding Remarks

This chapter focuses on providing a reliable SCF solution for temporary or metastable anions. As it is observed that in most SCF calculations for anionic molecules, SCF often leads to a minimum energy solution where the additional electron is typically present in the most diffuse state. When using a highly diffuse basis set, the SCF calculation will collapse into a neutral molecule and a free electron, making these SCF solutions unsuitable for further post-SCF calculations. Earlier, the charge stabilization method used extrapolation techniques to determine the energy, but this process resulted in the loss of information about the orbital wave function. In this chapter the modified PEM in conjunction with nuclear charge stabilization is implemented to obtain meaningful SCF solutions for metastable anions. These solutions can then be used for post-SCF calculations to include electron correlation. At higher nuclear charge values, the metastable anion becomes a bound anion, making the SCF solution more reliable. The basic idea is to utilize the solution at higher nuclear charges, where the electron occupies the correct orbital, and to obtain the SCF solution in the unbound region by reducing the additional nuclear charge to zero via PEM approach. A crucial aspect of obtaining meaningful SCF solutions for metastable anions is the fixed occupation number corresponding to the SOMO throughout the PEM calculation. The modified PEM method in conjunction with the nuclear charge stabilization method successfully provides SCF solutions for metastable anions. The solution obtained using the modified PEM is checked for being self-consistent-field solution, confirming the accuracy of the method. Notably, with this innovative approach, a meaningful SCF solution for metastable anions has been achieved using Hermitian quantum mechanics. Various anionic species (i.e., $C_2H_4^-$, $C_2H_2^-$, N_2^-, and $HCHO^-$) have been studied using this method, and their vertical electron affinities have been found to be in good agreement with experimental results.

Chapter 4

Application of Parametric Equations of Motion in non-Hermitian Domain using Complex Absorbing Potential

4.1 Introduction

This chapter explores the application of PEM in the non-Hermitian domain, with a special focus on studying resonances in the uracil molecule. In recent years, one of the primary focuses of studies on electron-molecule collisions has been the interaction with nucleobases. These nucleobases have the ability to accept an electron in their empty orbitals, resulting in the formation of anions. These anions are metastable states with a finite lifetime and are often referred to as temporary anions. The temporary anion may decay by either losing an electron or through a process known as DEA [148, 163, 164, 165, 7, 166, 167]. These anions are of significant interest due to their role in biological radiation damage. Experimental evidence shows that single and double DNA strand breaks can occur as a result of DEA [5, 168, 169, 170, 171].

The results of a DEA process are influenced by the energy and lifetime of the attached electron, determining whether fragmentation or non-dissociative relaxation occurs [172, 173, 174]. An ab initio approach is essential to understand how low-energy electrons (LEE) cause DNA damage through DEA and to explore their interactions with nucleobases. The initial step in understanding the DEA process involves identifying and characterizing the resonances that arise during the scattering process. These anionic resonance states of nucleobases are formed by attaching an electron into one of the unoccupied virtual orbitals (specifically, the $\pi^\star$ and $\sigma^\star$ orbitals) of the neutral ground state. While $\pi^\star$ shape-type resonances have been both observed experimentally and calculated theoretically, $\sigma^\star$ shape resonances may also exist if an electron is added to a $\sigma^\star$ orbital. While $\sigma^\star$ shape resonances have not yet been observed experimentally, they have been theoretically calculated[175, 176, 177].

This chapter mainly focuses on the shape resonance in uracil and providing an alternate approach to implement CAP at the SCF level using PEM (i.e., PEM-CAP approach). As the smallest nucleobase, uracil has received considerable attention in theoretical research. The attachment energies of electrons to nucleobases in the gas phase were first measured in 1998 by Aflatooni et al. using electron transmission spectroscopy (ETS) [178], and later extended for halouracils [179]. Numerous theoretical studies on uracil are available in the literature. For scattering calculations, Gianturco and Lucchese identified three low-energy $\pi^\star$ resonances and two $\sigma^\star$ resonances associated with uracil [180]. Additionally, Tonzani and Greene reported low-energy elastic electron scattering cross sections, which included the energies and widths of the $\pi^\star$ resonances for uracil as well as four other DNA nucleobases [181]. Previous studies on the uracil anion have produced a wide range of results. These include the stabilized Koopmans' theorem (S-KT) [176], the R-matrix approach [182, 180], and the Schwinger multi-channel method with pseudopotential (SMCPP) [183]. More recent research has utilized the Generalized Padé Approximation (GPA) along with stabilization graphs [167, 184], as well as the CAP combined with the symmetry-adapted cluster-configuration interaction (SAC-CI) method [185]. For all these methods, it is crucial to identify the desirable molecular orbital (MO) that can be filled by an extra electron, as LUMO depends heavily on the basis sets used in self-consistent field (SCF) calculations. Recently, in our group, the nuclear charge stabilization method has been implemented in conjunction with PEM[152, 153] to accurately identify the desired MO for the extra electron. Previously, this methodology was only applied within the framework of Hermitian quantum mechanics. Here, as CAP is incorporated at the HF level, it will no longer remain in the Hermitian domain. Therefore, the nuclear charge stabilization method has been implemented alongside PEM in the non-Hermitian domain to accurately identify the states filled by the extra electron. The advantage of using this method is that it allows access to multiple resonances in single-shot calculation. The identified states can be used for post-Hartree-Fock calculations, and here, the second-order dilated electron propagator method is applied to account for relaxation and correlation effects. In 1980, Donelly and Simons, applied a second-order electron propagator approach to study a metastable anion[186]. They demonstrated that the Aguilar-Balslev-Combes-Simon coordinate transformation, r-r exp(iθ), to G(E) yield an analytically continued complex propagator G(Z, θ) with complex poles corresponding to the complex electron affinities of atomic or molecular anions. They also presented the equations for the coordinate-rotated propagator, accurate to second order in electron-electron interaction.

4.2 Results and Discussion

This chapter presents an alternative approach to implementing the CAP at the HF level using the PEM method. Initially, the method is applied to the neutral C_2H_4 molecule for test calculations, and subsequently, it is used for uracil. All quantum chemistry calculations are executed using the Molgw package[143] in non-Hermitian domain by modifying the program significantly. The cube files generated from Molgw are used to plot the orbitals using the Gaussian16 package[187].

4.2.1 Ethylene (C_2H_4)

The calculations for C_2H_4 are performed using the cc-pVDZ basis set, with additional p-type function augmentations. These augmentations are done by multiplying the smallest exponent of the previous basis set by $1/2^n$, where n is a positive integer, to achieve n-p augmentations. The resonance energy obtained at HF level via Koopmans' theorem are referred as CAP/KT results and at SoDEP level are referred as CAP/SoDEP results.

The box size for C_2H_4 used in the CAP calculation has been selected based on its prior application in a referenced article[188]. With this optimized box size, the parameter η is varied through PEM, resulting in the corresponding η trajectory. To verify the results and confirm the accuracy of the outcomes from PEM-CAP, separate diagonalization calculations are conducted for different values of η. Both results are plotted, as illustrated in the Figure 4.1, and found to be indistinguishable, matching each other with an accuracy up to the fifth decimal place.

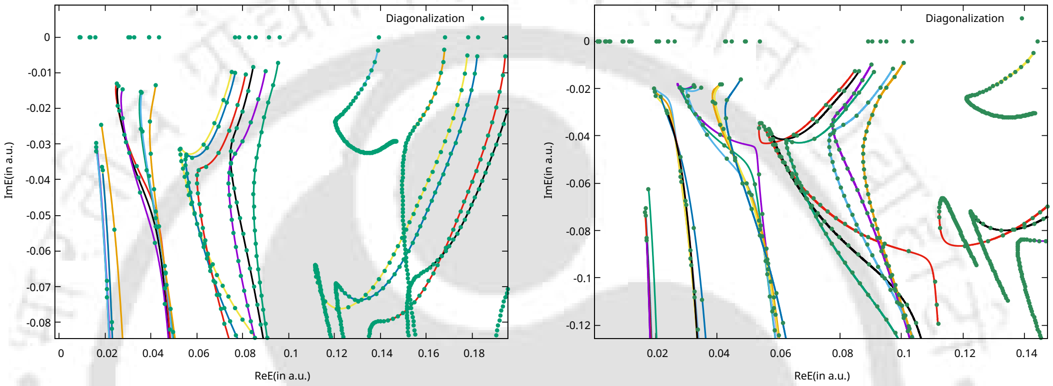

(a) cc-pVDZ+5p (b) cc-pVDZ+8p

FIGURE 4.1: $\eta-$trajectories for C_2H_4 using cc-pVDZ+5p and cc-pVDZ+8p basis sets respectively. Dot represents the results from Diagonalization approach while line plot is obtained via PEM approach.

The line plot is only feasible in the PEM approach, as it keeps track of every state with variations in the η parameter. In contrast, obtaining a line plot is impossible with diagonalization, since states are rearranged and cross each other when the η value changes. When comparing the time taken by the two approaches with the same number of η points, PEM is many order magnitude faster in case of cc-pVDZ+5p basis set. For a larger basis set, PEM calculation basis becomes much faster[152, 153]. The PEM-CAP approach offers the advantage of early convergence, while the diagonalization method converges more slowly as diagonalization results are independent of previous η values, whereas PEM results relies on the solution obtained for previous η value.

Resonance energy is determined from the stationary point or cusp in the η-trajectory. However, based on the η-trajectory depicted in the Figure 4.1, it is challenging to identify which trajectory corresponds to the resonance state. Therefore, an effective approach is needed to facilitate the identification of resonance state among the continuum state cusps. In our previous work, the nuclear charge stabilization method, in conjunction with the PEM, was implemented in our group to identify localized states or true LUMOs embedded within the continuum states. The method is applied here to identify the resonance state accurately. The procedure which is followed is outlined below:

a) Choose an η value by examining the η-trajectory near one of the cusps.

b) Perform calculations for nuclear charge stabilization using PEM at the chosen η. Identify the true LUMO or resonance state from the resulting plot. The most stabilized state at a higher nuclear charge will be considered the true LUMO or resonance state.

c) Plot the identified resonance state energy against the η-trajectory. Follow the curve corresponding to the true LUMO and cusp along that curve will represent the resonance energy.

For both the basis sets, the charge stabilization method calculations are carried out with the PEM approach, and only the real part of the orbital energies is plotted in the charge stabilization plot shown in Figure 4.2, the resonance state is identified as the stabilized state at a higher nuclear charge.

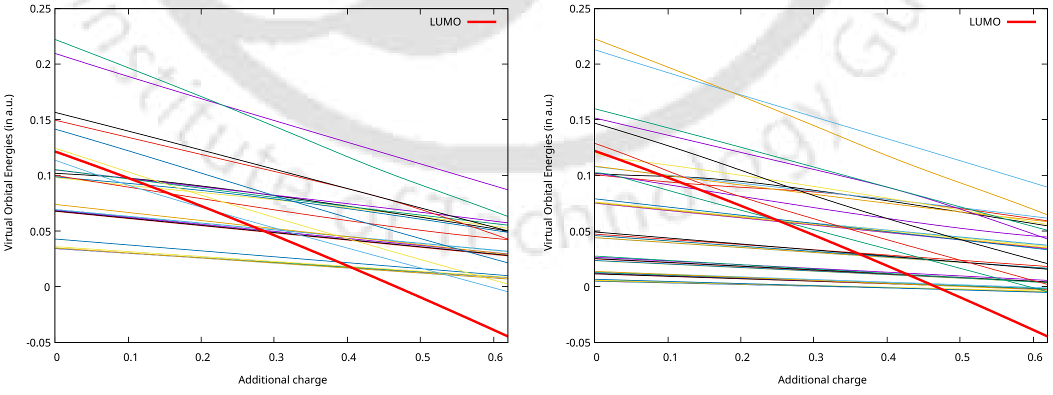

(a) cc-pVDZ+5p (b) cc-pVDZ+8p

FIGURE 4.2: Charge stabilization plot for C_2H_4 at η_{opt} using cc-pVDZ+5p and cc-pVDZ+8p basis sets respectively at CAP/KT level. The red line represents the true resonance state.

Here, the nuclear charge stabilization method, in conjunction with PEM, is implemented in the non-Hermitian Domain. It was observed that in the Hermitian domain, in the nuclear charge stabilization plot, there were avoided crossings between the true LUMO and the same symmetry diffuse states, which made identifying LUMO a little complicated[153]. So, the modified PEM was the solution to avoid such complications. However, in the non-Hermitian domain, there are no avoided crossings observed.

Second-order dilated electron-propagator (SoDEP) calculations are carried out to account for correlation and relaxation effects. The obtained η trajectories for SoDEP indicate that the position of the cusp or stationary point corresponding to the resonance state remains relatively unchanged with respect to η_{opt} from HF. Additionally, the resonance energy exhibits minimal variation for several η values near the cusp. Therefore, to obtain the resonance energies, one can perform calculations using the same η_{opt} values derived from CAP/KT calculations for each basis set, as the positions of the cusp do not differ significantly in SoDEP. The η trajectory plots for CAP/KT and CAP/SoDEP calculations using cc-pVDZ+5p and aug-cc-pVDZ+5p basis sets are shown in Fig 4.3. The resulting resonance energies, reported in Table 4.1, are in good agreement with experimental result.

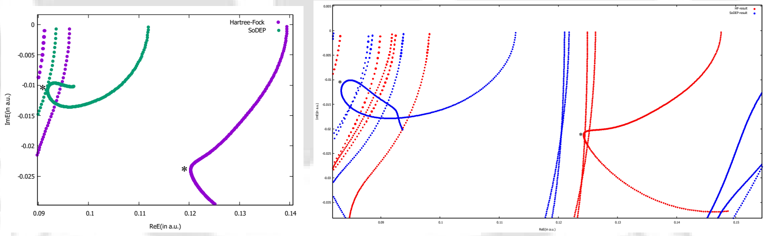

(a) cc-pVDZ+5p (b) aug-ccpVDZ+5p

FIGURE 4.3: $\eta-$trajectories for C_2H_4 using cc-pVDZ+5p and aug-cc-pVDZ+5p basis sets at CAP/KT and CAP/SoDEP level. $\star$ represent the resonance energy at η_{opt} value.

4.2.2 Uracil

The accurate identification of true resonance or a state filled by an extra electron is achieved in the context of the non-Hermitian domain. For C_2H_4, the resonance

Table 4.1: Resonance Energies and widths (in parenthesis) of C_2H_4 obtained in this work at CAP/KT and CAP/SoDEP level using different basis set, and comparisons with experimental result.

Basis set	CAP/KT-results			CAP/SoDEP-results		
	Energy(eV)	Width(eV)	η_{opt} value	Energy(eV)	Width(eV)	η_{opt} value
cc-pVDZ+5p	3.28	1.30	0.0023	2.53	0.52	0.0022
cc-pVDZ+8p	3.30	1.31	0.0023	2.53	0.52	0.0022
aug-cc-pVDZ+5p	3.38	1.16	0.0031	2.31	0.54	0.0030
Experimental Result[189]	1.78 eV (0.7 eV)					

energy corresponding to that identified state is obtained at the HF and SoDEP level. The above-discussed method is now implemented in biological molecules, i.e., uracil. The optimized geometry structure of the neutral uracil molecule is obtained by optimization in Gaussian[187] at the MP2 level using a 6-311G basis set.

Uracil is a polar molecule that exhibits a dipole-bound state. To investigate this dipole-bound state, heavily diffuse functions are required. For the calculations, the cc-pVDZ+nsmplp basis set is employed, which includes augmentations of s-type, p-type, and d-type functions with factors of $1/3^{(n/m/l)}$ instead the factor of $1/2^{(n/m/l)}$ as the calculation will be highly costly with the factor of $1/2^{(n/m/l)}$; where n, m, and l are positive integers. The energy of the associated with the dipole-bound state converges as s-type, p-type, and d-type functions are added. The energy for this dipole-bound state is presented in Table 4.2.

Table 4.2: Energy corresponding to the dipole-bound state of uracil using different basis sets at HF level.

Basis set	Energy (eV)
cc-pVDZ+3p	0.1470
cc-pVDZ+4p	0.0261
cc-pVDZ+5p	-0.0078
cc-pVDZ+6p	-0.0149
cc-pVDZ+7p	-0.0163
cc-pVDZ+3s6p	-0.0249
cc-pVDZ+4s6p	-0.0272
cc-pVDZ+5s6p	-0.0278
cc-pVDZ+6s6p	-0.0278
cc-pVDZ+5s6p3d	-0.0250
cc-pVDZ+5s6p4d	-0.0250

In the gaseous phase, uracil exhibits a metastable state characterized by positive orbital energies associated with its π^* and $\sigma^\star$ states. Previous studies have identified three $\pi^\star$ resonances and one $\sigma^\star$ resonance. The CAP method is employed at the Hartree-Fock level. The obtained solution is then used to perform calculations at SoDEP level which accounts for correlation and relaxation effects. The box size for the CAP calculations is selected based on its application in a referenced article[188]. For the CAP calculations, the additional augmentation is done with with factors of $1/2^n$; where n is a positive integer. CAP calculations are performed in conjunction with PEM by implementing it into the Fock matrix. Diagonalization results are obtained for comparison and are found to indistinguishable when plotted. However, analyzing the η trajectory plot, as shown in Figure 4.4(a), complicates the assignment of the specific resonances for $1\pi^\star$, $2\pi^\star$, and $3\pi^\star$. This complexity arises due to the presence of multiple cusps or kinks that correspond to various continuum states. So, the nuclear charge stabilization method in conjunction with PEM is performed at the chosen η in similar procedure followed for C_2H_4. From the stabilization plot, multiple resonances are identified in a single calculation, as these three states represent the most stabilized state at higher nuclear charges. When plotting the tracked orbital from the PEM calculations, it is observed that they exhibit $\pi^\star$ antibonding character. It is not necessary to perform the charge stabilization plot for extremely high nuclear charges; instead, one can conduct the calculations at a more reasonable value and then compare the slopes. Afterward, plot the corresponding orbital that has a steeper slope for confirmation to save computational time. The charge stabilization plot with real part of the orbital energies at a function of additional nuclear charge is shown in Figure 4.4(b).

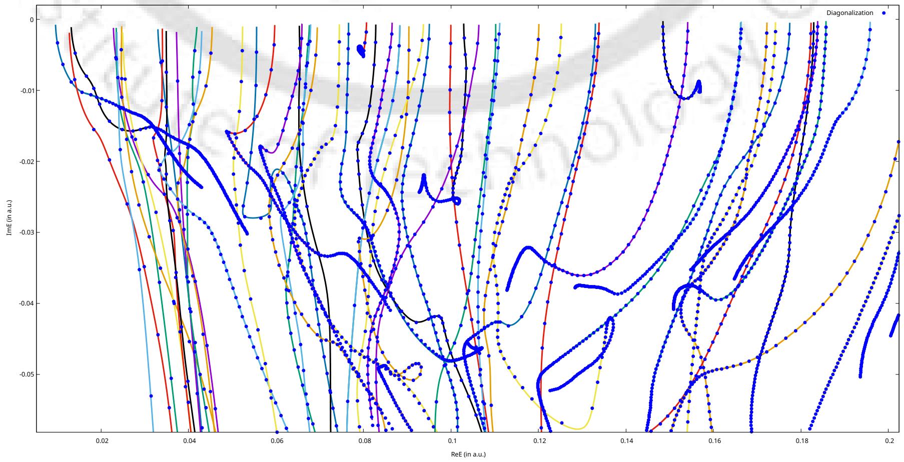

(a) $\eta-$trajectory

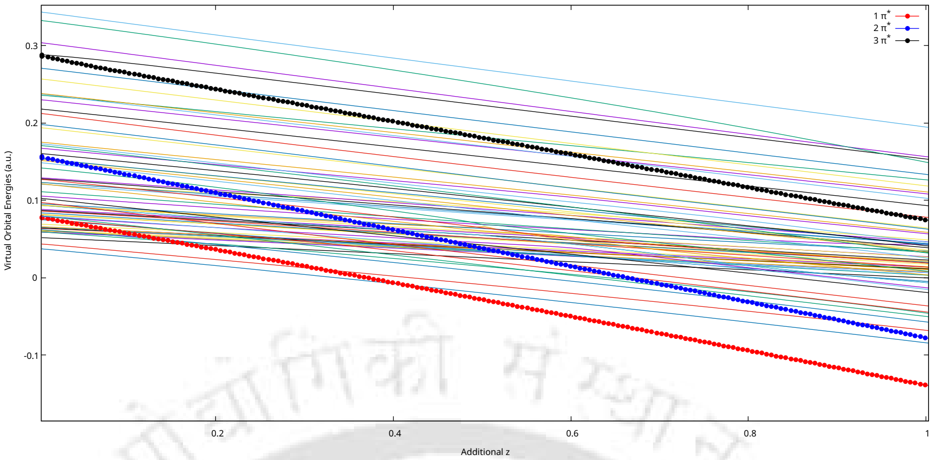

(b) charge stabilization plot

Figure 4.4: (a) $\eta-$trajectories for uracil using cc-pVDZ+4p basis set. Dot represents the results from Diagonalization approach while line plot is obtained via PEM approach. (b) Charge stabilization plot for uracil at η_{opt} using cc-pVDZ+4p basis set at CAP/KT level.

Several calculations are performed with different type of augmentations. It is observed that the inclusion of s-type functions has a little to no impact on the resonance energy, and similarly, the d-type augmentations exhibit negligible effects. In contrast, p-type augmentations have a significant influence, and the calculations are continued until converged values are achieved. Orbital plots for $1\pi^\star$, $2\pi^\star$, and $3\pi^\star$ are provided in Fig 4.5. The corresponding η-trajectory for particular resonance state using different basis sets are shown in Figures 4.6-4.10. The resonance energies corresponding to the identified states are provided in Table 4.3.

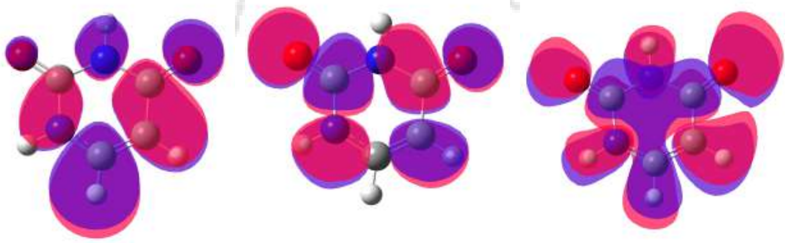

(a) $1\pi^\star$ (b) $2\pi^\star$ (c) $3\pi^\star$

Figure 4.5: Identified LUMO's orbital picture for uracil at η_{opt} value using cc-pVDZ+4p basis set at CAP/KT level. Isovalue is chosen as 0.02.

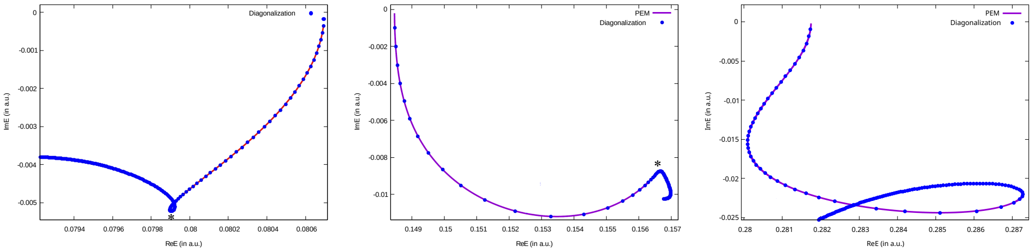

(a) $1\pi^\star$ (b) $2\pi^\star$ (c) $3\pi^\star$

FIGURE 4.6: $\eta-$trajectories for different states of uracil using cc-pVDZ+4p basis set at CAP/KT level. $\star$ represent the resonance energy at η_{opt} value.

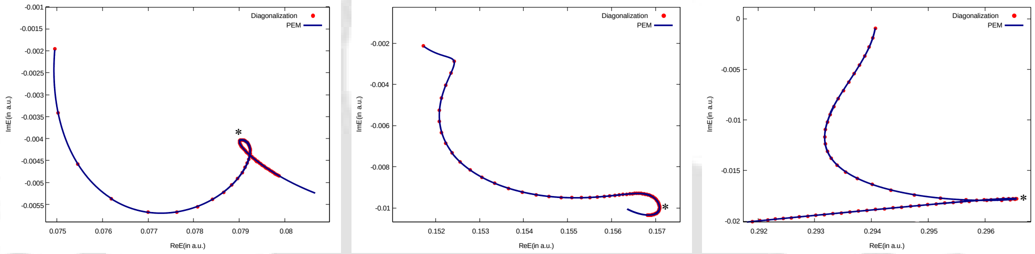

(a) $1\pi^\star$ (b) $2\pi^\star$ (c) $3\pi^\star$

FIGURE 4.7: $\eta-$trajectories for different states of uracil using cc-pVDZ+5p basis set at HF level. $\star$ represent the resonance energy at η_{opt} value.

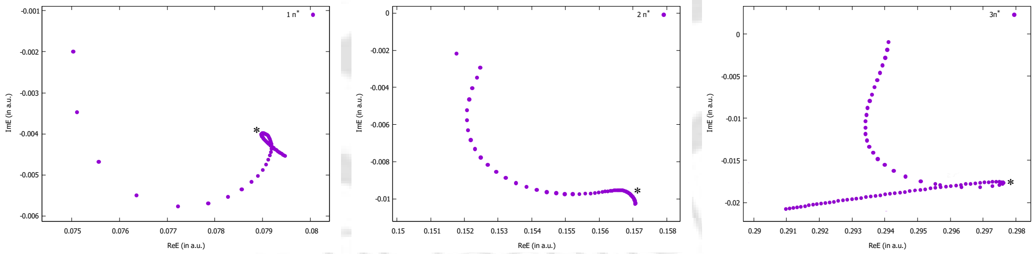

(a) $1\pi^\star$ (b) $2\pi^\star$ (c) $3\pi^\star$

FIGURE 4.8: $\eta-$trajectories for different states of uracil using cc-pVDZ+5s5p basis set at CAP/KT level. $\star$ represent the resonance energy at η_{opt} value.

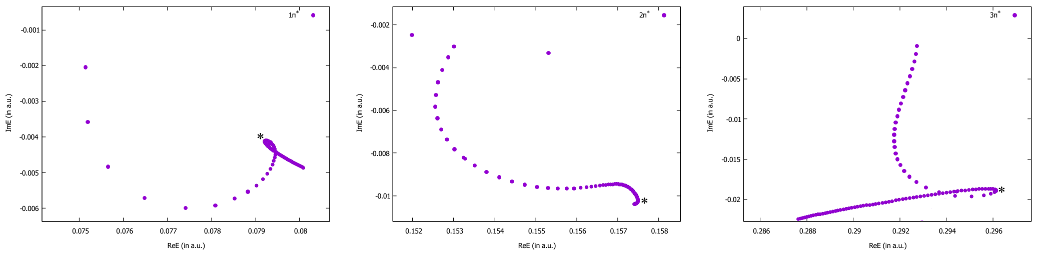

(a) $1\pi^\star$ (b) $2\pi^\star$ (c) $3\pi^\star$

Figure 4.9: $\eta-$trajectories for different states of uracil using cc-pVDZ+5p1d basis set at CAP/KT level. $\star$ represent the resonance energy at η_{opt} value.

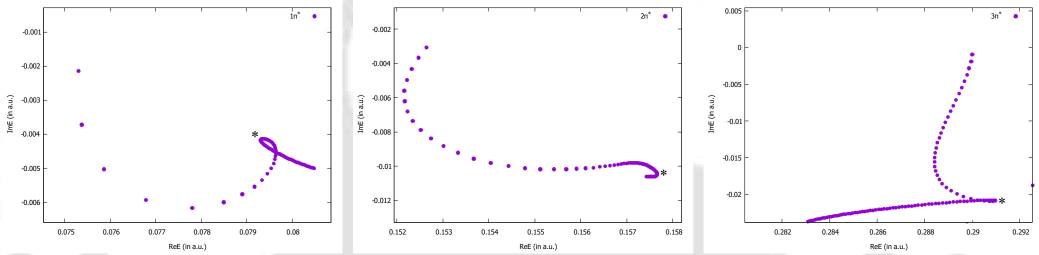

(a) $1\pi^\star$ (b) $2\pi^\star$ (c) $3\pi^\star$

Figure 4.10: $\eta-$trajectories for different states of uracil using cc-pVDZ+5p2d basis set at CAP/KT level. $\star$ represent the resonance energy at η_{opt} value.

Table 4.3: Resonance Energies and widths (in parenthesis) of uracil obtained in this work at the CAP/KT-level using different basis sets

Basis set	CAP/KT result (in eV)		
	$1\pi^\star$	$2\pi^\star$	$3\pi^\star$
cc-pVDZ+4p	2.14 (0.25)	4.26 (0.49)	7.81 (1.10)
cc-pVDZ+5p	2.14 (0.22)	4.26 (0.52)	8.09 (0.96)
cc-pVDZ+5s5p	2.15 (0.22)	4.26 (0.52)	8.10 (0.96)
cc-pVDZ+5p1d	2.15 (0.22)	4.27 (0.52)	8.05 (1.02)
cc-pVDZ+5p2d	2.16 (0.22)	4.27 (0.53)	7.92 (1.13)

Second-order dilated electron-propagator calculations are conducted to account for electron correlation and the effects of relaxation. In the η trajectories, the value of η_{opt}, obtained from the HF calculation, does not change significantly from the η_{opt} in the SoDEP calculations. Therefore, the same η_{opt} can be used to determine the resonance energies. The η trajectory plot for CAP/SoDEP calculation is shown in

Fig 4.11. The resonance energies corresponding to three resonances are obtained and compared with other theoretical and available experimental results. It is found that the obtained results agree well with other theoretical findings and available experimental data. The results are presented in Table 4.4.

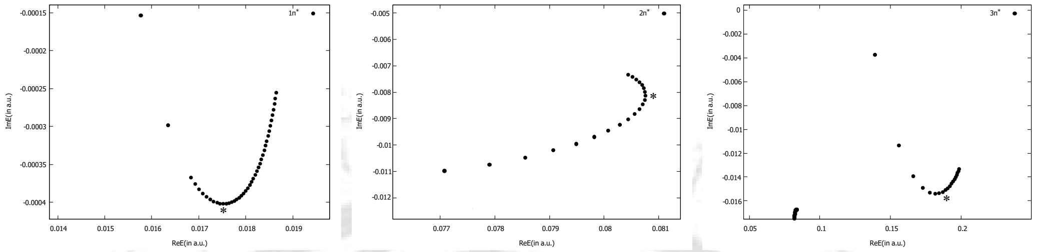

(a) $1\pi^\star$ (b) $2\pi^\star$ (c) $3\pi^\star$

FIGURE 4.11: $\eta-$trajectories for different states of uracil using cc-pVDZ+4p basis set at CAP/SoDEP level. $\star$ represent the resonance energy at η_{opt} value.

TABLE 4.4: Tabular Data for resonance Energies and widths (in parenthesis) of uracil obtained in this work at the CAP/SoDEP level using cc-pVDZ+4p basis set, along with comparisons to previous theoretical and experimental results.

	$1\pi^\star$	$2\pi^\star$	$3\pi^\star$
Exp.[178]	0.22	1.58	3.83
CAP/SAC–CI[185]	0.57 (0.05)	2.21 (0.10)	4.82 (0.58)
Stab-DFT[176]	0.36 (0.05)	1.75 (0.10)	4.52 (0.23)
SMCPP[183]	0.14 (0.005)	1.76 (0.15)	4.83 (0.78)
R matrix (2004)[180]	2.27 (0.21)	3.51 (0.38)	6.50 (1.03)
R matrix (2009)[182]	0.13 (0.003)	1.94 (0.17)	4.95 (0.38)
Winstead and McKoy[190]	0.32(0.018)	1.91(0.168)	4.95(0.38)
Tonzani and Greene[181]	2.16(0.2)	5.16(0.6)	7.8(0.9)
RVP[191]	0.597 (0.014)	2.183 (0.140)	4.858 (0.657)
This work(SoDEP/cc-pVDZ+4p)	0.48 (0.02)	2.19 (0.44)	4.92 (0.82)

4.3 Concluding Remarks

This chapter focuses on two important aspects. Firstly, it provides an alternative approach to implementing the CAP at the HF level. Secondly, it aims to identify the true resonance state that could be occupied by an extra electron. The first aspect is successfully achieved by implementing CAP in conjunction with the PEM, which offers the advantage of tracking every state as the CAP strength parameter varies, which was not possible with previous diagonalization methods. Additionally, using CAP with PEM is faster than diagonalization, and the benefits are particularly significant with larger basis sets. For example, with aug-cc-pVTZ+5p basis set for C_2H_4, PEM calculation is atleast ten times faster than the diagonalization approach. The second goal is particularly important, as identifying the true resonance state can be challenging through traditional methods such as examining the η trajectory or plotting the orbital picture. This challenge was successfully addressed by applying a nuclear charge stabilization technique alongside PEM in the non-Hermitian domain. This method enables us to identify one or multiple resonance states in a single calculation. Both approaches have been successfully applied to C_2H_4 and the uracil molecule, where successful identification of $\pi^\star$ antibonding of ethylene and $1\pi^\star$, $2\pi^\star$ & $3\pi^\star$ resonance states of uracil is achieved. Second-order dilated electron propagator is also applied to include electron correlation and relaxation effects. The results obtained from the second-order dilated electron propagator are in good agreement with previous theoretical and available experimental results.

Chapter 5

Self-Consistent-Field Solution for Metastable Anions after the Removal of Pseudo-Continuum States

5.1 Introduction

During SCF calculations with a heavily diffused basis set, we encounter a sea of pseudo-continuum states alongside the important localised states. These pseudo-continuum states are responsible for the variational collapse happening in the study of metastable anions. This phenomenon has been thoroughly discussed in various studies. For instance, variational collapse occurs in the case of SO_4^{2-}, where the SCF method generates the lowest-energy wave function for the $SO_4^- + e^-$ system instead of the wave function for the metastable SO_4^{2-}[97]. Similar instances of variational collapse have also been noted in the temporary anionic states of N_2, CO[192, 193, 42], CH_3CN, CH_3NC[194, 195], CH_3SCN, CH_3NCS[195], chloromethanes[196], polyatomic hydrocarbons[189, 197], silane & linear silanes[198, 199], biological anions that may lead to DEA such as uracil[176, 167, 191], and various other metastable anions. In chapter 3, an effort has been made to provide a SCF solution for metastable anions while avoiding the variational collapse, and the obtained solution can then be used for post-SCF calculations[200]. However, chapter 3 was limited to a Hermitian framework, which did not provide information about the lifetime of the electron attached states. If these pseudo-continuum states are indeed responsible for variational collapse, and if they can somehow be eliminated from our solution, then variational collapse would not occur in any scenarios, including at the post-SCF level. Eliminating them will not only address the issue of variational collapse in the study of metastable anions but will also save computational time. An important task to consider is how many states are being removed and the criteria for this decision. All the states that exist between the HOMO and the true LUMO are pseudo-continuum states and are responsible for variational collapse. Therefore, these states can be removed from the calculations. The true LUMO represents the actual state that an additional electron will occupy, characterized by a well-defined and localized shape (for example, the $\pi^\star$ antibonding character in the case of C_2H_4). Identifying the true LUMO is a crucial step in this methodology; if the incorrect true LUMO is selected, it can lead to significant inaccuracies in the results. The precise identification the true LUMO even when using heavily diffuse basis sets is successfully achieved using nuclear charge stabilization method in conjunction with PEM[152, 153].

This chapter aims to address variational collapse solutions by removing the pseudo continuum states and implement it in a non-Hermitian domain, where the lifetime of electron attached state can be accessed. Here, CAP is implemented at Hartree-Fock level and the solution obtained at the HF-level is then used to perform the post-SCF calculation. The obtained non-Hermitian SCF solution is used for post-SCF calculation (i.e. MP2) to improve the accuracy of the results obtained from Hartree-Fock method. This chapter also examines how much the continuum states (i.e., those between HOMO and the true LUMO) contribute to the correlation energy for neutral molecules. The correlation energy is calculated at MP2 level of theory and observed that the impact of removal of these pseudo-continuum states on the correlation energy is insignificant. Furthermore, this method should be applicable to excited state calculations and core-excited shape or Feshbach resonances. An electron can attach to an existing excited state configuration, resulting in core-excited shape or Feshbach resonances. In these resonances, the configuration includes a vacancy in an inner filled orbital and two electrons in a virtual orbital[182, 167, 201, 80]. Utilizing diffuse basis functions poses significant challenges, particularly due to the attached electron in the most diffuse states and also the difficulty in generating core-excited states. However, if there are no pseudo-continuum states in the calculations, both of these issues will be resolved easily.

In this Chapter, an effort is made to obtain the SCF solution for the $C_2H_4^-$ and $HCHO^-$ anionic species in non-Hermitian domain after removing the pseudo-continuum states. Additionally, the effect on correlation energies is also observed after removing the pseudo-continuum states for both the species by performing calculations at MP2 level.

5.2 Methodology

The method applied in this work is the modified version of SCF after removing the states. Initially, usual SCF calculation is carried out for neutral species and then the identification of the true LUMO state that is going to be filled by the extra electron. The identification of true LUMO is achieved the nuclear charge stabilization method in conjunction with PEM. All the notations are taken from Szabo[104] and carry same meaning until mentioned explicitly. Following the conventional SCF, After diagonalizing the F' , the orbital energies(ϵ) and C' is obtained,

$$F'C' = C'\epsilon \tag{5.1}$$

,

where F' is defined conventionally as

$$F' = X^T F X \tag{5.2}$$

and matrix elements corresponding to Fock-matrix are;

$$F_{mn} = T_{mn} + V_{mn}^{nucleus} + \sum_{\lambda\sigma} P_{\lambda\sigma}[(mn|\sigma\lambda) - \frac{1}{2}(m\lambda|\sigma n)] \tag{5.3}$$

where

$$P_{\lambda\sigma} = \sum_{a}^{occ} C_{\lambda a} C_{\sigma a}^{\star}, \tag{5.4}$$

and T_{mn} is the matrix elements of kinetic energy whereas $V_{mn}^{nucleus}$ is matrix elements of the electron-nucleus attraction corresponds to all nuclei.

Second step involves reduction of states which are not important. First mark the states between HOMO and true LUMO, and, then remove those many states from C' matrix. The matrix obtained after the removal of states is now referred as C'_{red}. And from this C'_{red} matrix , C$_{red}$-matrix is prepared as

$$C_{red} = XC'_{red} \tag{5.5}$$

Using C$_{red}$, the new Fock-matrix is evaluated for the desired system i.e., for anions or excited states by modifying the occupation number;

And then F$'_{red}$ matrix is generated as

$$F'_{red} = X^T F_{red} X \tag{5.6}$$

Performing unitary transformation on F$'_{red}$ gives;

$$F^{''} = U^T F'_{red} U \tag{5.7}$$

where U $= C'_{red}$.

The obtained F$^{''}$ is then solved for the following eigen-value problem

$$F^{''} C^{''} = C^{''} \epsilon^{''} \tag{5.8}$$

to obtained the orbital energies of the remained states and corresponding $C^{''}$. Now the obtained $C^{''}$ is used to make new C'_{red} by

$$C'_{red} = UC^{''} \tag{5.9}$$

and C$'_{red}$ is used to start the iteration by going back to equation 5.5. This process is followed iteratively until the convergence is achieved.

5.3 Results and Discussion

All quantum chemistry calculations are performed using the Molgw[143] package. The package is modified for the non-Hermitian calculations and for the SCF approach after removal of pseudo-continuum states. The cube files generated from Molgw are used to plot the orbitals using the Gaussian16[144] package. All calculations are performed using Cartesian Gaussian functions. A detailed discussion is provided below on the effect of correlation energy after the removal of pseudo-continuum states and to obtain the meaningful SCF solution for the $C_2H_4^-$ anion and for $HCHO^-$ anionic species.

5.3.1 Ethylene anion ($C_2H_4^-$)

It is important to note that when dealing with metastable anions, using diffuse basis sets does not yield a reliable SCF solution; instead, the system tends to converge to a neutral molecule and a free electron. This chapter presents an approach to obtain the meaningful SCF solution for a metastable anion by performing the SCF calculation after removing pseudo-continuum states. Before proceeding, it is essential to understand the significance of these removed pseudo-continuum states in relation to correlation energy and their impact on it. To illustrate this, a MP2 calculation is performed on a neutral molecule using various diffuse basis sets, including additional augmentations for both scenarios: one where all states are included and another where the pseudo-continuum states are removed. In case of second scenario, identifying the true LUMO accurately before removing the pseudo-continuum states is a crucial step. To achieve this, the nuclear charge stabilization calculations are performed using PEM to accurately identify the true LUMO. All states between HOMO and the true LUMO are excluded to perform modified SCF calculations, as these states are pseudo-continuum. Basis sets are augmented with extra diffuse basis functions so that the effect of adding s-type and p-type diffuse functions on correlation energy is observed. These augmentations are done by multiplying the smallest exponent of the previous basis set by $1/2^n$, where n is a positive integer. After performing MP2 calculations using the cc-pVTZ+nsmp basis sets, it was found that these pseudo-continuum states contribute only 1% to 2.2% of the total correlation energy. The correlation energies for both cases were obtained, and the differences using different basis sets are reported in Table 5.2. For instance, with the cc-pVTZ+8p basis set, the change in correlation energy is approximately 2.2%, with 36 states removed (excluding the true LUMO). However, when the true LUMO is also included in the total number of removed states, the total change in correlation energy is nearly 9%. This indicates that the localized state, or true LUMO, significantly affects the correlation energy. The overall difference in correlation energy when 36 pseudo-continuum states are removed is significantly lower than the contribution from the true LUMO alone in the correlation energy. Therefore, these pseudo-continuum states do not significantly impact the correlation energy. It is also important to note that the computational time remains nearly the same regardless of how many diffuse functions are added compared to the basis set without these additional functions. This is because all the diffuse states that lie between the HOMO and the true LUMO are excluded from the calculations. For comparison,calculation times for the neutral C_2H_4 molecule with all states included versus the times taken after the removal of pseudo-continuum states for the cc-pVTZ+7p/8p basis set are reported. Data for CPU time taken with all the states and after removing pseudo-continuum states using cc-pVTZ+7p/8p basis sets for C_2H_4 is provided in Table 5.1.

TABLE 5.1: Tabular data for CPU time taken with all the states and after removing pseudo-continuum states using cc-pVTZ+7p/8p basis sets for C_2H_4

Basis set	CPU time taken will all the states	CPU time taken with reduced number of states
cc-pVTZ+7p	1702 seconds	904 seconds
cc-pVTZ+8p	2007 seconds	983 seconds

Remaining states can now be employed to study metastable anions and excited states, as the pseudo-continuum states do not significantly affect the correlation energy. In this chapter, the SCF solution for metastable anion is achieved after removing the pseudo-continuum states. The first and the most important step is to accurately identify the true LUMO, as this is the only state that is going to be filled by an extra electron. The SCF solution for the metastable anion after removing the removing the pseudo-continuum states is then achieved by modifying the occupation number, which involves filling the extra electron into the true LUMO state. Choosing

Table 5.2: The table presents the correlation energy obtained using conventional SCF method, as well as the results after removing pseudo-continuum states. It also includes the differences and percentage differences, along with the number of states removed using various basis sets for neutral C_2H_4 molecule.

Basis Set	Correlation Energy (in a.u.)	Correlation Energy with reduced number of states(in a.u.)	Difference in Correlation Energy (in a.u.)	% Difference	Number of states removed
cc-pVTZ+3p	-0.3744	-0.3719	0.0025	0.67	6
cc-pVTZ+4p	-0.3745	-0.3697	0.0048	1.28	12
cc-pVTZ+5p	-0.3745	-0.3680	0.0065	1.73	18
cc-pVTZ+6p	-0.3745	-0.3670	0.0075	2.00	24
cc-pVTZ+7p	-0.3745	-0.3665	0.0080	2.13	30
cc-pVTZ+8p	-0.3745	-0.3663	0.0082	2.18	36
cc-pVTZ+8p	-0.3745	-0.3423	0.0322	8.59	37 (Including true LUMO)
cc-pVTZ+5s	-0.3739	-0.3708	0.0031	0.83	6
cc-pVTZ+5s8p	-0.3746	-0.3649	0.0097	2.58	40

the incorrect true LUMO can lead to a variational collapsed SCF solution again, making the identification of the correct state the most crucial step for obtaining a reliable SCF solution for metastable anions. Even when using heavily diffuse basis set, once the true LUMO is identified accurately, meaningful SCF solution for the metastable anion is obtained by adding the extra electron to the true LUMO (i.e., by modifying the occupation number).

The electron-attached states of metastable anions are associated with a finite lifetime, and, their wavefunctions are not square-integrable. To address this issue and make the wavefunction square-integrable, CAP is added to the Fock matrix. Additionally, the lifetime corresponding to the electron-attached state is also achieved. The box size is optimized in such a way that the resonance energies show minimal variation as the box size changes. The resonance energy is calculated at the HF level of theory for box size optimization (see Table 5.3), where, Resonance Energy is defined as

$$E_{res} = E_{anion} - E_{neutral} \tag{5.10}$$

The η-trajectories at the Hartree-Fock level, for various box sizes using the cc-pVDZ+5p basis set, are illustrated in Figure 5.1. The optimal box size is a cubic box with a length of 7 a.u., where the resonance energy converges and a sharp kink is observed.

TABLE 5.3: Resonance energies for $^2B_{2g}$ resonance in $C_2H_4^-$ at HF-level are tabulated for different box size using cc-pVDZ+5p basis set.

Box-size ($x_0/y_0/z_0$ in a.u.)	Resonance Position (in eV)	Resonance Width (in eV)
5.5/5.5/5.5	2.86	0.69
6.0/6.0/6.0	2.87	0.72
6.5/6.5/6.5	2.87	0.74
7.0/7.0/7.0	2.87	0.75

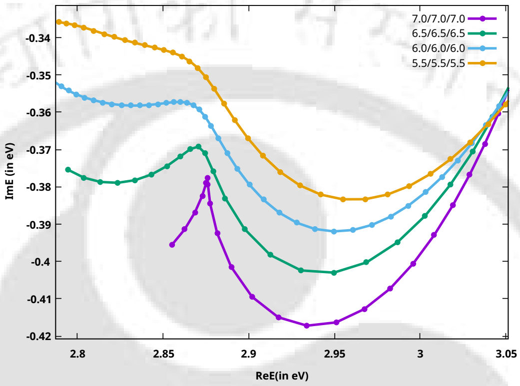

(a) cc-pVDZ+5p

FIGURE 5.1: The $\eta-$trajectories for $^2B_{2g}$ resonance in $C_2H_4{}^-$ corresponding to different box-size parameter using cc-pVDZ+5p basis set.

It is important to understand how the calculations for anions are performed for different η values in order to obtain a complete η trajectory. The calculations for the η trajectory are carried out in two steps:
i) For each η, neutral molecule self-consistent field (SCF) calculations are performed, and the true LUMO is identified.
ii) A SCF calculation is carried out for anions by modifying the occupation number (i.e., by adding an extra electron in true LUMO state) after removing all states between the HOMO and the true LUMO.

Understanding the definition of the true LUMO is crucial since the choice of true LUMO state is a significant step in the process. The true LUMO refers to the state that an additional electron will occupy and is the state that is most stabilized at a higher nuclear charge. To accurately identify the true LUMO, a methodology that combines the nuclear charge stabilization method with PEM is employed, as discussed in previous chapters. When using a heavily diffuse basis set, it is possible to encounter states with the same symmetry as true LUMO. This can lead to avoided crossings in the charge stabilization plot due to mixing of states, which complicates the identification of the true LUMO. To effectively address these avoided crossings, a modified PEM alongside the charge stabilization method is implemented. This approach leads to a precise identification of the true LUMO. An important concern arises regarding the accuracy of the SCF solution obtained for the metastable anion after removing the pseudo-continuum states. Conventional SCF calculations for the metastable anion at a specific η value show reasonable results, suggesting that the singly occupied molecular orbital (SOMO) has a localized $\pi^\star$ character for the C_2H_4 anion at that specific η value. This indicates that the extra electron occupies the correct orbital, rather than a diffuse orbital, which means that variational collapse is not occurring. Therefore, the conventional SCF solution at this η value is considered the standard solution for the metastable anion, serving as a basis for comparison with results from calculations where states are removed. It is important to understand that the SCF calculation for a neutral molecule at that η value still results in pseudo-continuum states between the HOMO and the true LUMO. These pseudo-continuum states have to be removed before performing the SCF calculation for metastable anion and comparing the results. The same procedure described above is followed to obtain the SCF solution for a metastable anion after removing the pseudo-continuum states. Remarkably, it is found that both solutions are identical. Energies obtained at HF level and MP2 level for anionic species and neutral species at that specific η are provided in Table 5.4 and Table 5.5.

TABLE 5.4: Tabular data for HF and MP2 energies obtained with all the states and with removal of states using cc-pVDZ+4p for C_2H_4

Basis set/System	η-value	HF-energy with all states	HF-energy with reduced states	MP2-energy with all states	MP2-energy with reduced states
cc-pVDZ+4p/Anion	0.0280	(-77.93097,-0.01154)	(-77.93097,-0.01154)	(-78.23343,-0.014554)	(-78.23301,-0.01448)
cc-pVDZ+4p/Neutral	0.0280	(-78.04204,-0.00149)	(-78.04204,-0.00149)	(-78.33087,-0.00176)	(-78.33051,-0.00171)

TABLE 5.5: Tabular data for HF and MP2 energies obtained with all the states and with removal of states using cc-pVDZ+5p for HCHO

Basis set/System	η-value	HF-energy with all states	HF-energy with reduced states	MP2-energy with all states	MP2-energy with reduced states
cc-pVDZ+5p/Anion	0.0100	(-113.81900,-0.00422)	(-113.81900,-0.00422)	(-114.16258,-0.00719)	(-114.16203,-0.00723)
cc-pVDZ+5p/Neutral	0.0100	(-113.88349,-0.00024)	(-113.88349,-0.00024)	(-114.21867,-0.00035)	(-114.21824,-0.00038)

It is worth noting that there may be rearrangements of states occurring in step one, which means that the position of the true LUMO at two different η values from the HF calculation might not be the same. This makes it extremely challenging to keep track of the orbital numbers between the HOMO and the true LUMO, as it requires significant human effort to manage. An alternative solution to this problem is to implement the PEM-CAP[202] approach in this step, which simplifies the process of tracking orbitals. With this method, one can easily identify and remove the appropriate number of states at any η value. The solution obtained at the HF level is then used for post-SCF calculations (in this case, employing MP2). At the optimized the box size, the parameter η is varied through the PEM-CAP[202] approach for different basis sets, resulting in the corresponding η trajectories.

The η trajectories at both HF and MP2 levels for various basis sets (i.e., cc-pVDZ+5p, aug-cc-pVDZ+5p, and aug-cc-pVTZ+5p) are illustrated in Figure 5.2. In case of aug-cc-pVTZ+5p, cc-pVDZ basis set is used for H-atom. The stabilization point, or cusp, represents the resonance energy in the η trajectory plot.

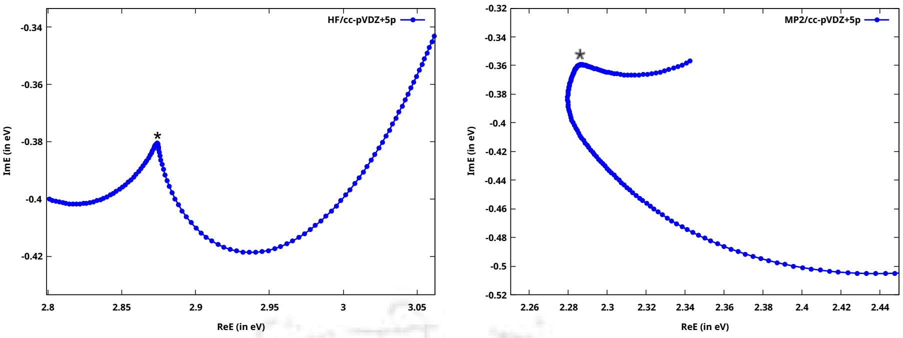

(a) HF/cc-pVDZ+5p (b) MP2/cc-pVDZ+5p

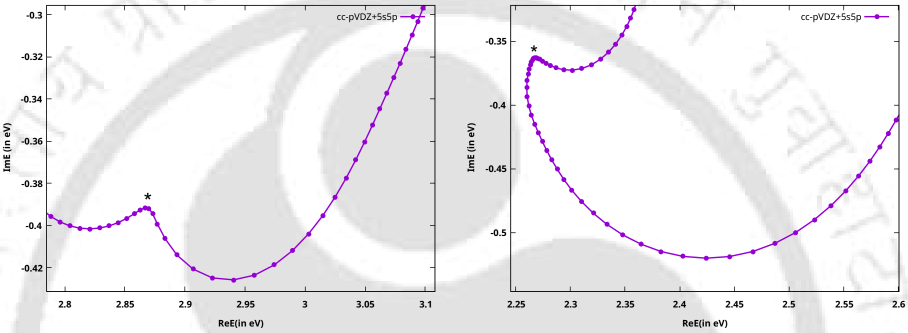

(c) HF/cc-pVDZ+5s5p (d) MP2//cc-pVDZ+5s5p

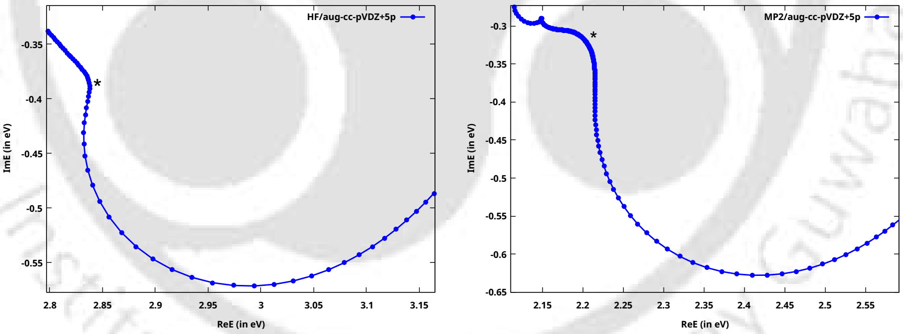

(e) HF/aug-cc-pVDZ+5p (f) MP2/aug-cc-pVDZ+5p

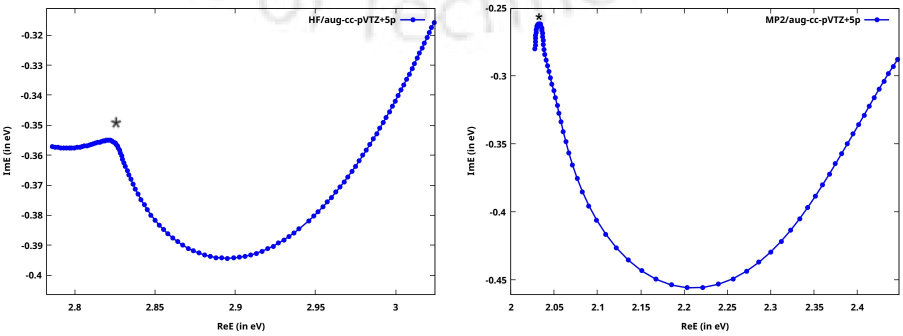

(g) HF/aug-cc-pVTZ+5p (h) MP2/aug-cc-pVTZ+5p

FIGURE 5.2: The η-trajectories corresponding to the $^2B_{2g}$ resonance in $C_2H_4^-$ using various basis sets at both the HF and MP2 levels.

Resonance energies are obtained at both the HF and MP2 levels using various basis sets, as shown in Table 5.6, which also includes the optimal η (η_{opt}) value. The obtained resonance energies are in good agreement with experimental results and previously available theoretical studies. A summary of the resonance energies, along with the experimental results and findings from earlier theoretical studies, is provided in Table 5.7. The value of S^2 was found to be in the range of 0.75–0.77 in all cases, which is close to the expected value of 0.75 for one unpaired electron.

TABLE 5.6: Resonance energies for $^2B_{2g}$ resonance in $C_2H_4^-$ at both HF and MP2 methods are presented using different basis sets.

Basis Set	Resonance Energy at HF level			Resonance Energy at MP2-level		
	Resonance Position (in eV)	Resonance Width (in eV)	η_{opt} value	Resonance Position (in eV)	Resonance Width (in eV)	η_{opt} value
cc-pVDZ+5p	2.87	0.75	0.0117	2.28	0.71	0.0136
cc-pVDZ+5s5p	2.88	0.77	0.0122	2.26	0.72	0.0138
cc-pVDZ+6p	2.87	0.76	0.0116	2.29	0.71	0.0138
cc-pVDZ+7p	2.87	0.76	0.0116	2.29	0.71	0.0138
aug-cc-pVDZ+5p	2.85	0.75	0.0133	2.22	0.62	0.0165
aug-cc-pVTZ+5p	2.84	0.72	0.0120	2.03	0.52	0.0160

TABLE 5.7: Tabular data corresponding to previous theoretical and experimental result for resonance energy and width of the $^2B_{2g}$ resonance in in $C_2H_4{}^-$.

Reference/Method	Resonance Energy(in eV)	Resonance Width(in eV)
Electron transmission[160, 154]	1.80	0.70
Complex Kohn[203]	1.83	0.46
Diagonal 2ph-TDA biorthogonal dilated electron propagator[56]	1.89	0.18
Complex Kohn[204]	1.85	0.50
ACCC[205]	1.86	0.47
Stabilization method/ EOM-CCSD/aug-cc-pVTZ+3p[197]	2.06	0.64
CAP-EOM-EA-CCSD/ aug-cc-pVTZ+3s3p3d (0th order)[192]	2.09	0.430
CAP-EOM-EA-CCSD/ aug-cc-pVTZ+3s3p3d (1st order)[192]	2.03	0.33
CAP/SAC-CI[206]	2.02	0.46
SA-15-CASSCF(3e, 20o)[207]	3.119	0.634
MP2/cc-pVDZ+5p (this work)	2.28	0.71
MP2/aug-cc-pVDZ+5p (this work)	2.22	0.62
MP2/aug-cc-pVTZ+5p (this work)	2.03	0.52

5.3.2 Formaldehyde anion ($HCHO^-$)

As discussed earlier in the case of the ethylene molecule, the effect of removing pseudo-continuum states for the HCHO molecule is also examined. Calculations using the cc-pVTZ+nsmp basis sets reveal that these states contribute only 1-5% to the total correlation energy. The correlation energies for both scenarios (i.e., one with conventional SCF and the second after removal of pseudo-continuum states) are calculated, and the differences obtained using different basis sets are reported in Table 5.8. Notably, the cumulative difference in correlation energy from the 33 removed states is lower than the contribution from the true LUMO when using the cc-pVTZ+8p basis set. Thus, these pseudo-continuum states do not significantly affect the correlation energy. Additionally, Similar observations are made regarding the computational time that the time remains nearly the same regardless of the number of diffuse function additions compared to the basis set without extra augmentation.

Table 5.8: The table presents the correlation energy obtained using conventional SCF method, as well as the results after removing pseudo-continuum states. It also includes the differences and percentage differences, along with the number of states removed using various basis sets for neutral HCHO molecule.

Basis Set	Correlation Energy (in a.u.)	Correlation Energy with reduced number of states (in a.u.)	Difference in Correlation Energy (in a.u.)	% Difference	Number of states removed
cc-pVTZ+3p	-0.4255	-0.4233	0.0022	0.51	3
cc-pVTZ+4p	-0.4255	-0.4184	0.0071	1.67	9
cc-pVTZ+5p	-0.4256	-0.4140	0.0115	2.70	15
cc-pVTZ+6p	-0.4256	-0.4103	0.0153	3.59	21
cc-pVTZ+7p	-0.4256	-0.4080	0.0175	4.11	27
cc-pVTZ+8p	-0.4256	-0.4071	0.0185	4.34	33
cc-pVTZ+8p	-0.4256	-0.3693	0.0563	13.22	34 (Including true LUMO)
cc-pVTZ+5s	-0.4249	-0.4223	0.0025	0.59	5
cc-pVTZ+5s8p	-0.4265	-0.4070	0.0194	4.54	36

Similarly to $C_2H_4^-$, the parameter η is varied using the PEM-CAP[202] approach for different basis sets with the optimized box size, resulting in the corresponding η trajectory. CAP calculations are carried out through the PEM-CAP method, which is implemented into the Fock matrix. Figure 5.3 illustrates the η trajectories at the HF and MP2 levels for various basis sets (i.e., cc-pVDZ+5p, aug-cc-pVDZ+5p, and aug-cc-pVTZ+5p). The stabilization point, or cusp, in the η trajectory plot indicates the resonance energy.

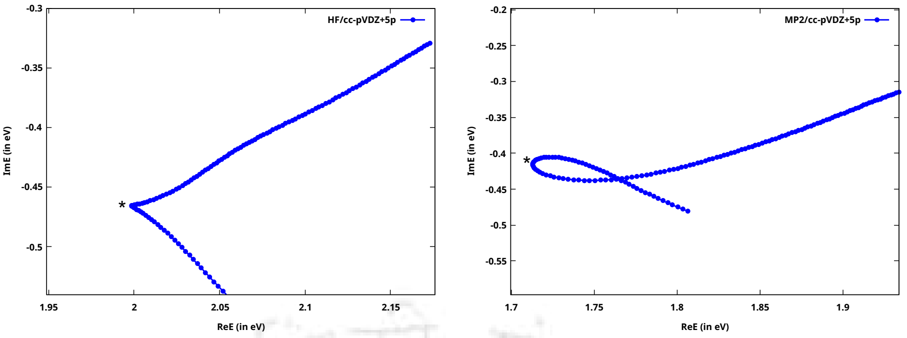

(a) HF/cc-pVDZ+5p (b) MP2/cc-pVDZ+5p

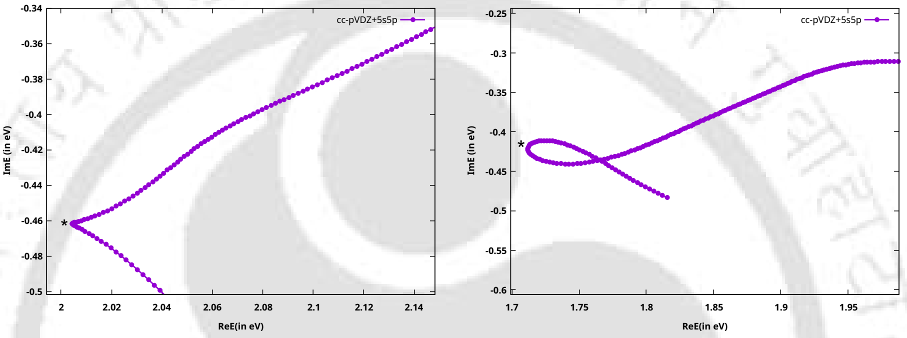

(c) HF/cc-pVDZ+5s5p (d) MP2/cc-pVDZ+5s5p

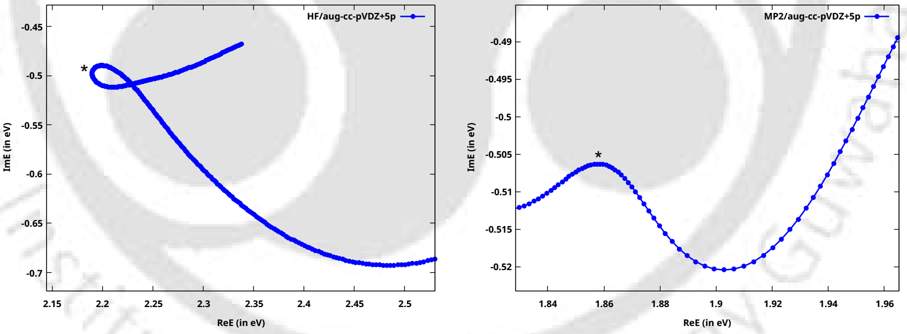

(e) HF/aug-cc-pVDZ+5p (f) MP2/aug-cc-pVDZ+5p

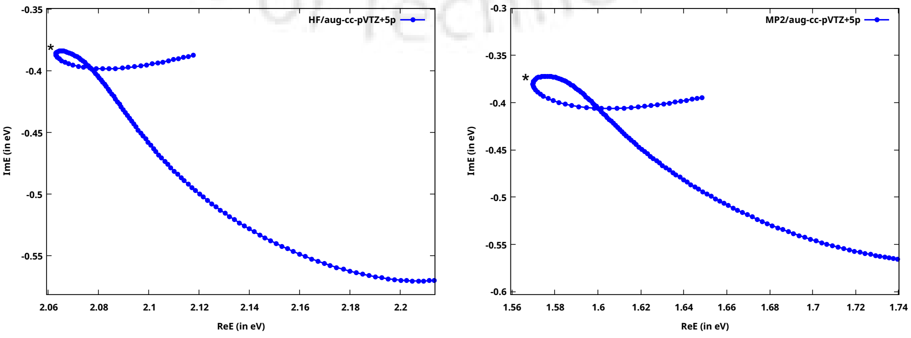

(g) HF/aug-cc-pVTZ+5p (h) MP2/aug-cc-pVTZ+5p

FIGURE 5.3: The η-trajectories corresponding to the $^2B_1$ resonance in HCHO$^-$ using various basis sets at both the HF and MP2 levels.

Resonance energies are obtained at both the HF and MP2 levels using various basis sets, as shown in Table 5.9, which also includes the optimal η (η_{opt}) value. The obtained resonance energies are in good agreement with experimental results and previously available theoretical studies. A summary of the resonance energies, along with the experimental results and findings from earlier theoretical studies, is provided in Table 5.10. The value of S^2 was found to be in the range of 0.75–0.77 in all cases, which is close to the expected value of 0.75 for one unpaired electron.

TABLE 5.9: Resonance energies for $^2B_1$ resonance in $HCHO^-$ at both HF and MP2 methods are presented using different basis sets.

Basis Set	Resonance Energy at HF level			Resonance Energy at MP2-level		
	Resonance Position (in eV)	Resonance Width (in eV)	η_{opt} value	Resonance Position (in eV)	Resonance Width (in eV)	η_{opt} value
cc-pVDZ+5p	2.00	0.92	0.0094	1.71	0.83	0.0104
cc-pVDZ+5s5p	2.01	0.92	0.0100	1.71	0.84	0.0101
cc-pVDZ+6p	2.02	0.98	0.0094	1.72	0.88	0.0102
cc-pVDZ+7p	2.03	0.98	0.0095	1.72	0.91	0.0102
aug-cc-pVDZ+5p	2.18	0.98	0.0141	1.85	1.00	0.0128
aug-cc-pVTZ+5p	2.06	1.00	0.0071	1.57	0.75	0.0074

TABLE 5.10: Tabular data corresponding to previous theoretical and experimental result for resonance Energy and width of the $^2B_1$ resonance of $HCHO^-$.

Reference/Method	Resonance Energy(in eV)	Resonance Width(in eV)
Electron transmission[160, 161]	1.0/0.86	
Vibrational excitation[162]	0.87	
Complex Kohn[208]	1.0	0.5
Diagonal 2ph-TDA[57]	0.89	0.12
R-matrix method/DZPd[209]	1.46	0.79
CAP/EOM-EA-CCSD (1st order)[192]	1.31	0.28
CAP/SAC-CI[206]	1.18	0.38
EOM-EA-CCSD[210]	1.16	0.57
CAP/XMS-CASPT2[211]	1.27–1.28	0.47–0.48
SA-15-CASSCF(3e, 16o)[207]	2.43	0.34
MP2/cc-pVDZ+5p (this work)	1.71	0.83
MP2/aug-cc-pVDZ+5p (this work)	1.85	1.00
MP2/aug-cc-pVTZ+5p (this work)	1.57	0.75

5.4 Concluding Remarks

This chapter provides a meaningful SCF solution for metastable anions after removing the pseudo-continuum states by modifying the Fock matrix. Here, CAP is implemented at the HF-level to make the metastable anion wavefunction square integrable, and to obtain the lifetime of the attached electron. In this chapter, the SCF solution for metastable anions is attained in a non-Hermitian domain after the removal of these pseudo-continuum continuum states. This elimination is achieved by modifying the SCF procedure to remove the states located between the HOMO and the true LUMO. The obtained SCF solution can then be used for post-SCF calculations, such as CI, CCSD, MP2, and MP4, to account for electron correlation. The methodology consists of two steps. The first step involves accurately identifying the true LUMO in the neutral system and removing the pseudo-continuum states located between the HOMO and the true LUMO, as these states are responsible for variational collapse. The second step modifies the occupation number for the metastable anion by adding an extra electron to the true LUMO. The first step is particularly crucial; filling an incorrect orbital would lead to a solution that does not correspond to a metastable anion. In the present case, MP2 calculations are performed on C_2H_4 and HCHO neutral molecules, and it is observed that removing these pseudo-continuum states has no significant effect on the correlation energy. This method is extremely important as no variational collapse will occur for the metastable anion if the electronic state filled by the extra electron is identified correctly. Additionally, it significantly reduces computational time, making it a cost-effective approach for studying species that require diffuse functions to accurately describe the system. Two anionic species have been studied using this method, and their resonance energies are found to be in good agreement with experimental results. This method could potentially be expanded to investigate core-excited shape or Feshbach resonances in the future.

Chapter 6

Reflection-Free CAP using Parametric Equations of Motion

6.1 Introduction

To make resonance wave functions square integrable an CAP is added to the Hamiltonian. This addition of CAP to the Hamiltonian helps to absorb the wave function at the grid boundary. In the CAP method, the Hamiltonian is perturbed with an appropriate potential to achieve an absorbing boundary condition. However, because of its non-physical nature, the CAP can introduce artificial perturbations in the system, potentially leading to shifts in the calculated energy. When a propagating wave packet approaches the grid boundary, CAPs do not completely absorb the wave packet. This results in artificial reflections that can degrade the accuracy of the computed results. The extent of these artificial reflections depends on the parameters of the CAP, particularly its onset and strength. These reflections by CAPs have been analyzed in detail in refs [37] and [212].

The perturbations caused by CAPs become more pronounced as the CAP strength, denoted by η, increases[213, 214]. Ideally, it is preferred to keep η close to zero where the perturbation caused by the CAP will be minimum. High values of η can lead to significant perturbations, resulting in unreliable resonance energies and discontinuous potential energy surfaces (CPES)[213, 215]. For any given basis, there is a critical value of η below which the wave function remains non-square integrable, making it impossible to accurately represent resonances with a finite basis. This phenomenon was clearly demonstrated by Moiseyev and co-workers[216] in their study of a one-dimensional potential model. They showed that the results obtained with a finite basis sets converge with the exact eigenvalues when sufficiently high values of η are used. Additionally, they identified a critical value, η_c, below which the resonance wavefunction is no longer square integrable for a finite basis set as η decreases. The value of η_c depends on the set of basis functions employed; in general, a larger basis set corresponds to a smaller η_c. In the limit of a complete basis set, η_c approaches zero, meaning that $(\mathrm{E}(\eta = 0) = \mathrm{E}_{res})$, where E_{res} is the exact complex energy corresponding to a resonance state. However, for finite basis sets, taking (η) to zero yields a purely real spectrum, which does not provide any information on complex resonance energies.

It is evident from the previous discussion that a relatively large value of η specifically, $(\eta \geq \eta_c)$ is necessary for finite basis to ensure that the resonance wavefunction is square-integrable. However, using extremely large values of η_{large} (i.e., $\eta \gg \eta_c$) may result in strong artificial reflections. Therefore, to have meaningful and reliable eigenvalues, it is recommended to choose values of η within the range of $(\eta_c \leq \eta \leq \eta_{large})$. Moiseyev and his colleagues [216] demonstrated in a one-dimensional model that resonance energy can be determined through analytical continuation using the Padé approximant when data with $\eta \geq \eta_c$ are used. Their results, obtained from the finite basis set, align with the exact results that would be obtained if we could solve the time-independent Schrödinger equation with outgoing boundary conditions (OBCs). Specifically, this analytical continuation is carried out using the Padé approximant by fitting an energy function $\mathrm{E}(\eta)$ and then dilating the polynomial function to $\mathrm{E}(\eta \rightarrow 0)$ in order to obtain the complex resonance energy (E_{res}).The data set used to obtain the complex eigenvalues for resonance at $(\eta = 0)$ is selected from the range $(\eta \geq \eta_c)$, where the fitted function from the finite basis set coalesce with the exact ones. Later this approach was also applied to molecular systems where complex resonance energies are obtained at $\eta = 0$ through analytical continuation using the Padé approximant[193, 79]

In this study, the same results (i.e., numerically exact results) are obtained without the need for data extrapolation in the range where $\eta_c \geq \eta$, or where the numerical energies begin to coalesce. This is accomplished using a backward PEM-CAP approach, starting from the point where η_c is sufficient to make the resonance wavefunction square integrable, or where the numerical energies start to coalesce.

6.2 Methodology

The methodology discussed in the introduction chapter involves incorporating the CAP into the Fock matrix. However, in this chapter, a reflection-free CAP approach has been applied to a one-dimensional problem. This will lead to different equations for the PEM-CAP approach.A brief discussion is provided below regarding the one-dimensional CAP form and to obtain the PEM-CAP equation for this one-dimensional problem.

In the CAP approach, a complex potential $-i\eta W$ is added to the physical Hamiltonian H_0,

$$H = H_0 - i\eta W. \tag{6.1}$$

For one dimensional case, W can described by the following equations,

$$W = \begin{cases} 0, & |x| < x_0 \\ (x - x_0)^2, & |x| > x_0 \end{cases} \tag{6.2}$$

where x denotes the one-dimensional Cartesian coordinate and x_0 represents the CAP box-size parameter.

For PEM-CAP approach, considering the following eigenvalue problem

$$\bar{\bar{H}}\bar{C}_i^R = \bar{C}_i^R E_i \tag{6.3}$$

$$(\bar{C}_i^L)^T \bar{\bar{H}} = E_i (\bar{C}_i^L)^T \tag{6.4}$$

where $\bar{\bar{H}}$ is linearly dependent on η as

$$\bar{\bar{H}} = \bar{\bar{H}}_0 + \eta\bar{\bar{V}} \tag{6.5}$$

$\bar{\bar{H}}_0$ and $\bar{\bar{V}}$ are matrices which are independent of η and $\bar{C}_i^R$ and $\bar{C}_i^L$ are the respective right and left eigenvectors of complex general matrix $\bar{\bar{H}}$ having complex eigenvalues E_i. It is important to note the V contains the information of CAP potential matrix as (-iW). However in this case, Hamiltonian is complex symmetric matrix , therefore $\bar{C}_i^R = \bar{C}_i^L = \bar{C}_i$.

The evolution of eigenvalues (E) and eigenvectors (C) as a function of the linear perturbation parameter η is given as follows:

$$\frac{\partial E_n}{\partial \eta} = V_{nn} \tag{6.6}$$

$$\frac{\partial C_i}{\partial \eta} = -\Sigma_{j\neq i}\frac{C_j V_{ji}}{E_j - E_i} \tag{6.7}$$

For the application of PEM to calculate the eigenvalues using the Hamiltonian, V_{mn} is defined as

$$V_{mn} = C_m^T(\eta) V C_n(\eta) \tag{6.8}$$

Equations (6.6), (6.7) and (6.8) form a close set of equations and can be integrated to calculate eigenvalues and eigenvectors.

6.3 Results and Discussion

The Hamiltonian, $H_0 = -0.5d^2/dx^2 + (x^2/2 - 0.8)\exp(-0.1x^2)$, is chosen for the test-study model to calculate resonances. In this test-study model, the potential consists of a well embedded between two potential barriers of equal height. This potential supports one bound state and multiple resonance states, three of which will be discussed in this work. The wave function associated with these resonances are not square-integrable. To address this, a CAP is added to the Hamiltonian, which will absorb the outgoing tail of the resonance wave function and thus make it square-integrable. The efficacy of the CAP depends on both the strength parameter and the box size parameters, so both need to be optimized accordingly.

In initial calculations, a box size of 0 atomic units (a.u.) is used i.e., CAP within interaction region and η-trajectory calculations are carried out using a grid basis[217] with 200 functions, spanning η-values from 0 to 0.005. This η-trajectory is computed by diagonalizing the $\mathrm{H}_{\mathrm{CAP}}$ matrix. Then the backward η-trajectory calculations are performed starting from different η values using PEM-CAP approach, continuing until η approaches zero. It has been observed that starting from a particular value of η while performing backward PEM-CAP results in the following different η-trajectory path. As shown in Figure 6.1, when starting from an η value of 0.0004 or 0.0010 near the cusp, the trajectory follows the same path as that obtained from the forward η-trajectory using diagonalization approach. However, for η values greater than 0.0017, the trajectory continues along a different path while exhibiting complex eigenvalues at $\eta = 0$. It is found that as the higher values of η is used for backward η trajectory using PEM-CAP approach, the resonance values converges "numerically exact value" providing both resonance position and lifetime which are also reported in ref[216]. It is crucial to address the observation that, with a higher value of η, the backward PEM-CAP trajectory deviates from its expected path, which ideally should follow the forward trajectory. Interestingly it is not only following different path but also converging to a numerically exact result at $\eta = 0$.

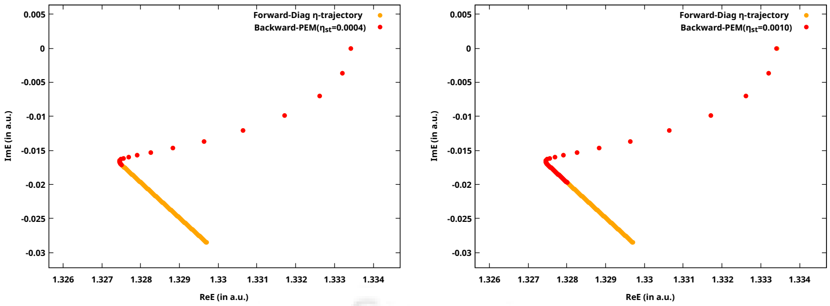

(a) η=0.0004 (b) η=0.0010

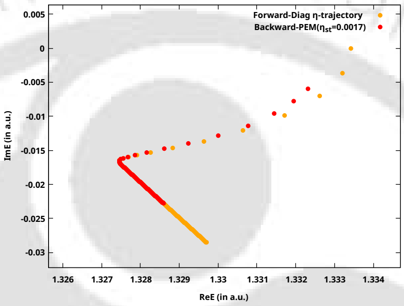

(c) η=0.0017

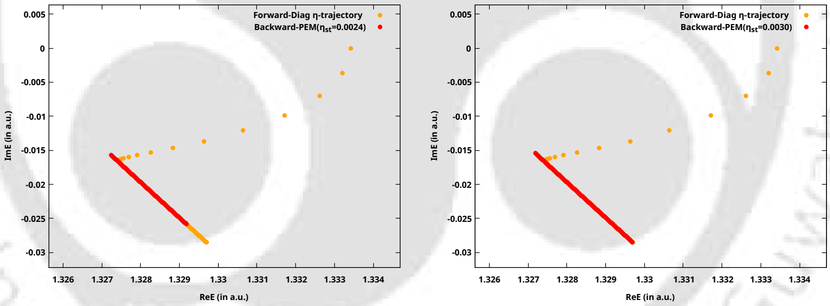

(d) η=0.0024 (e) η=0.0030

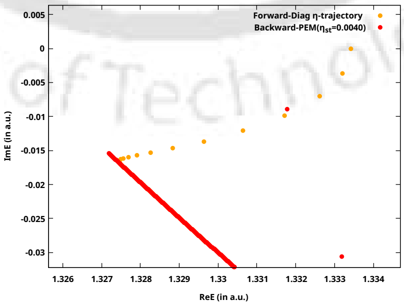

(f) η=0.0040

FIGURE 6.1: η-trajectory plot corresponding to Forward η-trajectory obtained by diagonalization(represented by orange dots) and backward PEM-CAP calculations starting from different η values (i.e., represented by red dots) using grid basis with 200 functions. In the first two top panels, red dots are on top of the orange dots as they follow the same trajectories.

More important and impressive results regarding multiple resonances is found. It is found that when implementing backward PEM-CAP approach starting from higher value of η, the resonance energies corresponding to multiple higher resonances converges to a complex value at $\eta = 0$ and is exactly the same obtained via complex scaling (i.e., numerically exact values). In this study, for comparison of obtained results for multiple resonances, highly accurate complex scaling is carried out using grid basis with 2000 functions. As shown in Figure 6.2, every resonance state is getting converged to complex scaling results after performing the backward PEM-CAP approach. Energies at $\eta = 0$ obtained after performing backward PEM-CAP starting from different η values are reported in Table 6.1 along with the complex scaling result obtained using grid basis with 2000 functions. This approach offers advantage over Pade Approximation approach as in Pade approximant approach one has to rely on the data set for each higher resonances and then need to extrapolate till η value of zero, while backward PEM-CAP approach make this possible in single calculation without extrapolation.

TABLE 6.1: Tabular data for resonance energies (in a.u.) corresponding to first three resonances obtained at $\eta = 0$ after performing back-PEM starting from different η-values using grid basis with 200 functions. Complex scaling results are also obtained for comparison using grid basis with 2000 functions

η_{start}**-value**	**First resonance**	**Second resonance**	**Third resonance**
0.00040	(0.62103,0)	(1.33341,0)	(1.78951,0)
0.00100	(0.62103,0)	(1.33341,0)	(1.78951,0)
0.00170	(0.62097,-5.831×10^{-5}	(1.33232, -0.00603)	(1.82808,-0.087390)
0.00240	(0.62097,-5.828×10^{-5}	(1.32719,-0.015448)	(1.79088,-0.177557)
0.00300	(0.62097,-5.828×10^{-5}	(1.32720,-0.015447)	(1.78459,-0.173752)
0.00400	(0.62097,-5.825×10^{-5}	(1.32720,-0.015447)	(1.78459,-0.173751)
Complex Scaling/ Numerical Exact value	(0.62097,-5.826×10^{-5}	(1.32720,-0.015447)	(1.78458,-0.173751)

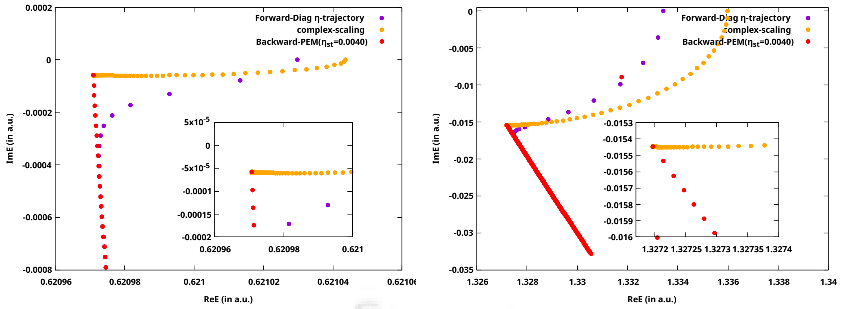

(a) First resonance (b) Second resonance

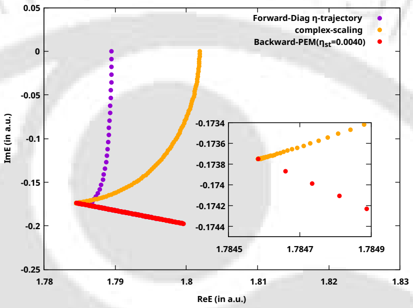

(c) Third resonance

FIGURE 6.2: η-trajectory plot corresponding to Forward η-trajectory obtained by diagonalization(represented by violet dots) and backward PEM-CAP calculation goes to $\eta = 0$ starting from $\eta = 0.0040$ (i.e., represented by red dots) using grid basis with 200 functions. Complex scaling results are also plotted for comparison and represented by orange dots.

A set of additional calculations also conducted calculations using different box sizes to observe their effect on the resonance energy obtained at $\eta = 0$ after employing the backward PEM-CAP approach, starting from an η value greater than the critical value. It was found that the resonance energies obtained at $\eta = 0$ after the backward PEM-CAP approach remain consistent across all cases, indicating that they are unaffected by the choice of box size. As shown in Figure 6.3, every resonance state with different box-size is getting converged to complex scaling results after performing the backward PEM-CAP approach. Energies at $\eta = 0$ obtained after performing backward PEM-CAP starting from different η values are reported in Table 6.2 for various box size. First three resonance wavefunction obtained at $\eta = 0$ after performing backward PEM-CAP are also shown in Figure 6.4. Here it is important to note that after performing the backward PEM-CAP calculation till $\eta = 0$, one can obtain the information about wavefunction in the physical limit of

$\eta = 0$ while it was not possible in the case of analytical continuation using Pade approximant.

TABLE 6.2: Tabular data for resonance energies (in a.u.) corresponding to first three resonances obtained at $\eta = 0$ after performing back-PEM for different boxes using grid basis with 200 functions.

x$_0$/η_{start}-value	**First resonance**	**Second resonance**	**Third resonance**
0.0 a.u./0.0040	$(0.62097,-5.826\times10^{-5}$	(1.32720,-0.015447)	(1.78459,-0.173751)
5.0 a.u./0.0055	$(0.62097,-5.825\times10^{-5}$	(1.32720,-0.015447)	(1.78459,-0.173751)
10.0 a.u./0.0085	$(0.62097,-5.826\times10^{-5}$	(1.32720,-0.015447)	(1.78459,-0.173753)
15.0 a.u./0.0134	$(0.62097,-5.826\times10^{-5}$	(1.32720,-0.015447)	(1.78459,-0.173747)
Complex Scaling/ Numerical Exact value	$(0.62097,-5.826\times10^{-5}$	(1.32720,-0.015447)	(1.78458,-0.173751)

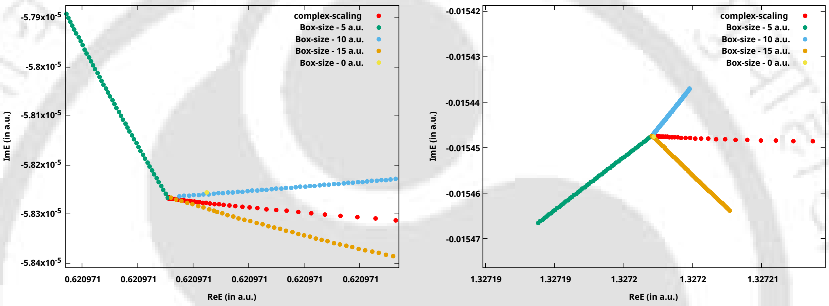

(a) First resonance (b) Second resonance

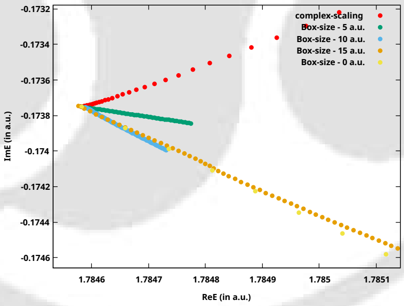

(c) Third resonance

FIGURE 6.3: η-trajectory plot corresponding to backward PEM-CAP calculation goes to $\eta = 0$ starting from $\eta = 0.0040$ for different box sizes using grid basis with 200 functions. Complex scaling results are also plotted for comparison and represented by red dots.

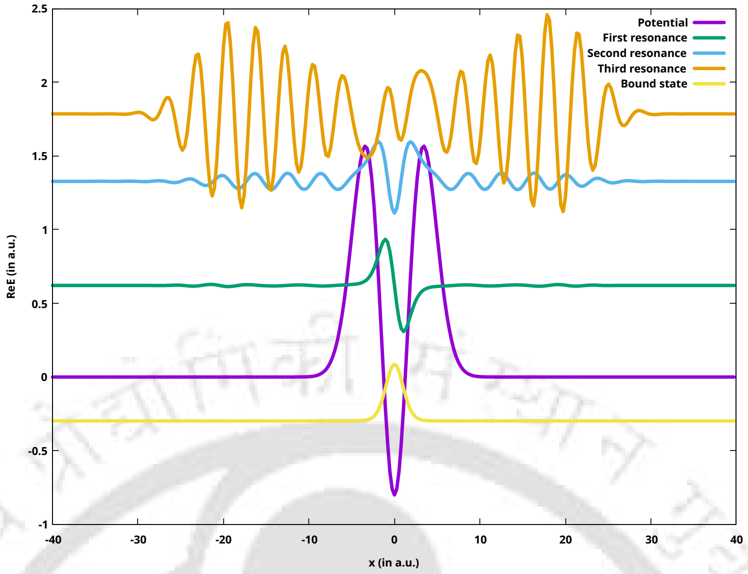

(a) wavefunction plot

FIGURE 6.4: Wavefunction plot corresponding to bound state and first three resonances using grid basis with 300 functions at $\eta = 0$ obtained after backward PEM-CAP approach.

6.4 Concluding Remarks

In this chapter, CAP is incorporated into the system Hamiltonian to make the resonance wavefunction square integrable. Since CAP is an artificial potential, a finite value of the CAP strength parameter (i.e., η) is necessary to determine the resonance energies. However, this finite value of η introduces perturbations to the system, causing artificial reflections that deteriorates the resonance energy values. This chapter presents an application of parametric equations of motion to calculate the resonances in the physical limit of $\eta = 0$ for the CAP. In this physical limit of $\eta = 0$, the effects of the CAP are eliminated, and complex values are still obtained for $\eta = 0$, indicating reflection-free results. So, a methodology is introduced to eliminate the artificial reflections caused by CAP through a backward PEM-CAP approach (i.e., starting from higher CAP strength parameter η to $\eta = 0$). During backward PEM-CAP, the eigenstates as a function of η do not follow the same path as forward trajectory (i.e., starting from $\eta = 0$ to higher η). Instead, the energy converges to the true numerically exact resonance energy, which includes both its position and lifetime. This technique enables us to reach the physical limit (i.e., $\eta = 0$), effectively removing the effects of the CAP. This approach offers several advantages: it allows the determination of resonance energies corresponding to multiple resonances at $\eta = 0$, and importantly, the box size does not influence the resonance energies obtained at $\eta = 0$. Additionally, it also provides accurate estimates for the resonance complex energies, (E($\eta = 0$)) corresponding to multiple resonances irrespective of box size in single calculation. As a consequence, there is no need to optimize the onsets, resulting in significant savings in computational time. Importantly, this methodology can be extended to atomic and molecular system, where one can reach the limit of $\eta = 0$ and also the obtained Hartree-Fock solution at $\eta = 0$ can be used to perform the post-SCF calculations.

Chapter 7

Summary and Conclusion

This thesis primarily focuses on developing innovative and effective theoretical methods for studying electronic resonance. It aims to identify problems related to electronic resonances and provide effective solutions. The thesis successfully provides methodology for the identification of the true LUMO and also provides methodology to obtain the meaningful SCF solutions for metastable anions. Additionally, a new approach known as PEM-CAP is introduced for implementing the CAP at the SCF level using PEM. By employing a nuclear charge stabilization method within the non-Hermitian domain, identification of multiple resonances is also achieved. Moreover, a methodology is also presented to eliminate pseudo-continuum states at the SCF level. Finally, the resonance energy in the physical limit, as η approaches 0, is obtained using the backward PEM-CAP approach. Below is a chapter-wise summary of the thesis.

Chapter 1 introduces the concept of resonances and reviews the existing methods used to study them. It also discusses the methodology implemented in this thesis for investigating resonances. Additionally, the chapter discusses the motivation behind the research presented in the thesis.

Chapter 2 presents an innovative and unique approach for the precise identification of the LUMO using parametric equations of motion. These LUMOs are crucial for studying various chemical processes and electronic resonances. It is important to note that SCF calculations do not always provide a meaningful LUMO representation. Our observations indicate that even with a compact basis set, obtaining a meaningful LUMO is not guaranteed. The nuclear charge stabilization method proves to be a significant approach for identifying the LUMO. However, reliance solely on this method makes it challenging as there is need to track the orbital changes that occur with variations in additional nuclear charge to generate the charge stabilization plot and it is nearly impossible to visualize any avoided crossings. To address these difficulties, a new approach is developed that combines nuclear charge stabilization with parametric equations of motion. This combination makes it significantly easier to track the orbitals and visualize avoided crossings. Not only does this new method allow us to visualize the avoided crossings, but the modified parametric equations of motion also successfully resolve the challenges posed by these avoided crossings. In our case study, the nuclear charge stabilization method along with the parametric equations of motion is applied for neutral N_2, C2H_2, and C_2H_4. It is observed that even with a compact basis set, the LUMO does not always exhibit the characteristics of a true LUMO. Instead, some LUMO+N^{th} state resembles the true LUMO (i.e., localized and well-defined character). Additionally, this study was extended to investigate the effects of extra diffuse basis functions for neutral C_2H_2 and C_2H_4, utilizing the cc-pVDZ+np basis set. It is found that avoided crossings were occurring between states of the same symmetry, complicating the task of identifying the true LUMO. To overcome this issue, the modified parametric equations of motion is implemented alongside the nuclear charge stabilization method. This approach allows to identify the true LUMO more easily, even when using heavily diffuse basis sets.

In Chapter 3, an attempt has been made to obtain the meaningful SCF solution for metastable anions. It is known that when a heavily diffuse basis set is used, the SCF solution for a metastable anion often yields a minimum energy configuration with an extra electron present in the most diffuse orbital. With the increases in additional diffuse basis functions, the SCF solution converges to a neutral molecule and a free electron. This phenomenon is referred to as ”variational collapse.” Any SCF solution with variation collapse does not describe the metastable anion, and hence, it should not be employed in post-SCF calculations intended to study these anions. To address variational collapse in the case of metastable anions, the nuclear charge stabilization method in conjunction with PEM is applied and a meaningful SCF solution is obtained. At higher nuclear charge values, the metastable anion becomes a bound anion, making the SCF solution more reliable. The basic idea is to utilize the solution at higher nuclear charges, where the electron occupies the correct orbital, and to obtain the SCF solution in the unbound region by reducing the additional nuclear charge to zero via PEM approach. A key feature of the PEM calculation is the fixed occupation number throughout the variation of the additional nuclear charge, which helps ensure that the electron occupies the correct orbital even in the unbound region. This method has been applied to obtain the SCF solutions for $C_2H_4^-$, $C_2H_2^-$, N_2^-, and $HCHO^-$ using cc-pVDZ+np basis sets, and it is observed that avoided crossings are occurring with the same symmetry states of diffuse character, leading to further breakdown of the solution. To overcome the issue of variational collapse occurring due to avoided crossing, a modified PEM is implemented in conjunction with the nuclear charge stabilization method, and a meaningful SCF solution is achieved without variational collapse. Additionally, MP2 calculations are carried out to incorporate electron correlation effects, and it has been found that the vertical electron affinities obtained are in good agreement with previously reported theoretical and experimental results.

Chapter 4 discusses the application of PEM in a non-Hermitian domain. In this chapter, a CAP is incorporated to study the ethylene and uracil anions, from which resonance energies are obtained. PEM is employed to solve the eigenvalue problem which has linearly dependent parameter. The addition of CAP to the Fock matrix represents an exact scenario in which PEM can be effectively applied. This chapter primarily focuses on two aspects. First, it presents an alternative approach for incorporating CAP at the SCF level using PEM (i.e., PEM-CAP approach). Second, it implements the nuclear charge stabilization method in a non-Hermitian domain to accurately identify the correct resonance state. The η-trajectories obtained from the PEM-CAP approach match exactly with those obtained through the diagonalization approach, confirming the accuracy of the PEM-CAP method. Additionally, the PEM-CAP approach is nearly ten times faster than the diagonalization method, this computational time advantage is even more pronounced when larger basis sets, such as triple-zeta and quadruple-zeta, are used. Furthermore, the nuclear charge stabilization method is effective in identifying multiple resonance states within the non-Hermitian domain. Since nucleobases are known to have multiple resonance states, identifying them on the η-trajectory can be quite challenging. For uracil, calculations demonstrate that the nuclear charge stabilization method successfully identifies multiple resonance states in a single calculation.

Chapter 5 presents a methodology to eliminate pseudo-continuum states from the SCF solution and utilize the obtained solution at the post-SCF level. It has been observed that when diffuse basis functions are employed, pseudo-continuum states can arise, leading to various difficulties, for example, variational collapse. By removing these pseudo-continuum states from the SCF solution, the problem of variational collapse can be avoided, and will make the computation part more straightforward. In this chapter, the SCF solution for metastable anions is attained in a non-Hermitian domain after the removal of these pseudo-continuum continuum states. This elimination is achieved by modifying the SCF procedure to remove the states located between the HOMO and the true LUMO. Additionally, it is also observed that these states do not significantly contribute to the correlation energy. The methodology consists of two steps. The first step involves accurately identifying the true LUMO and removing the pseudo-continuum states located between the HOMO and the true LUMO, as these states are responsible for variational collapse. The second step modifies the occupation number for the metastable anion by adding an extra electron to the true LUMO. The first step is particularly crucial; filling an incorrect orbital would lead to a solution that does not correspond to a metastable anion. In this study, the anions $C_2H_4^-$ and $HCHO^-$ are studied using this methodology, and MP2 calculations are also performed to account for electron correlation effects.

In Chapter 6, the focus is on obtaining the resonance energy in the physical limit as $\eta \to 0$ while using CAP. It is well known that applying CAP to the Hamiltonian requires a finite value of η as one can not reach the limit of complete basis, which introduces an artificial perturbation to the system and deteriorate the resonance energy. Therefore, efforts have been made to eliminate the effects of a finite η and to obtain the resonance energy in the limit of $\eta \to 0$. During backward PEM-CAP calculations starting with higher values of η, it is observed that at $\eta = 0$, the solution converges to a complex value. Notably, this value matches the one obtained using the complex scaling method with 2000 basis functions. Complex scaling result with 2000 basis functions is used as benchmark to compare the obtained results from backward PEM-CAP approach. Additionally, regardless of variations in the CAP box size, the backward PEM-CAP starting from higher η values consistently converges to the same benchmark result. Thus, it is possible to successfully obtain the resonance energy in the physical limit of $\eta \to 0$ using PEM-CAP approach while applying CAP for the study of resonances. Currently, this methodology is implemented in a one-dimensional model potential, but there are ongoing efforts to apply it to atomic and molecular systems.

Appendix A

Molecular Coordinates

Cartesian coordinates in Angstroms C_2H_2

Atom	**X**	**Y**	**Z**
C	0.0000	0.0000	0.6013
C	0.0000	0.0000	-0.6013
H	0.0000	0.0000	1.6644
H	0.0000	0.0000	-1.6644

Cartesian coordinates in Angstroms N_2

Atom	**X**	**Y**	**Z**
N	0.0000	0.0000	0.5450
N	0.0000	0.0000	-0.5450

Cartesian coordinates in Angstroms HCHO

Atom	**X**	**Y**	**Z**
C	0.0000	0.0000	0.0000
O	0.0000	0.0000	1.2050
H	0.0000	0.9429	-0.5876
H	0.0000	-0.9429	-0.5876

Cartesian coordinates in Angstroms for C_2H_4

Atom	X	Y	Z
C	0.6676247	0.0000000	0.0000000
C	-0.6676247	0.0000000	0.0000000
H	1.2300435	-0.9237114	0.0000000
H	1.2300435	0.9237114	0.0000000
H	-1.2300435	0.9237114	0.0000000
H	-1.2300435	-0.9237114	0.0000000

Cartesian coordinates in Angstroms for Uracil

Atom	X	Y	Z
C	1.28109662	0.39318602	0.00000000
O	2.28322476	1.08865341	0.00000000
C	1.24408094	-1.06621706	0.00000000
C	0.05220420	-1.70946984	0.00000000
N	-1.14194260	-1.02582427	-0.00000000
C	-1.23861893	0.36210188	-0.00000000
N	0.00000000	0.98235199	0.00000000
O	-2.30098333	0.95450956	-0.00000000
H	-0.02903028	-2.79141180	-0.00000000
H	-2.02461385	-1.51724723	-0.00000000
H	-0.02426956	1.99660865	-0.00000000
H	2.18100334	-1.60655354	0.00000000

Bibliography

[1] W. P. Reinhardt, "Complex coordinates in the theory of atomic and molecular structure and dynamics," *Annu. Rev. Phys. Chem.*, vol. 33, no. 1, pp. 223–255, 1982.

[2] N. Moiseyev, "Quantum theory of resonances: calculating energies, widths and cross-sections by complex scaling," *Phys. Rep.*, vol. 302, no. 5-6, pp. 212–293, 1998.

[3] N. Moiseyev, *Non-Hermitian quantum mechanics.* Cambridge University Press, 2011.

[4] G. Gamow, *The quantum theory of the atomic nucleus.* US Atomic Energy Commission, Division of Technical Information Extension, 1963.

[5] B. Boudaıffa, P. Cloutier, D. Hunting, M. A. Huels, and L. Sanche, "Resonant formation of DNA strand breaks by low-energy (3 to 20 ev) electrons," *Science*, vol. 287, no. 5458, pp. 1658–1660, 2000.

[6] A. D. Bass and L. Sanche, "Dissociative electron attachment and charge transfer in condensed matter," *Radiat. Phys. Chem.*, vol. 68, no. 1-2, pp. 3–13, 2003.

[7] J. Simons, "How do low-energy (0.1- 2 ev) electrons cause DNA-strand breaks?," *Acc. Chem. Res.*, vol. 39, no. 10, pp. 772–779, 2006.

[8] R. D. Thomas, "When electrons meet molecular ions and what happens next: dissociative recombination from interstellar molecular clouds to internal combustion engines," *Mass Spectrom. Rev.*, vol. 27, no. 5, pp. 485–530, 2008.

[9] C. R. Arumainayagam, H.-L. Lee, R. B. Nelson, D. R. Haines, and R. P. Gunawardane, “Low-energy electron-induced reactions in condensed matter,” *Surf. Sci. Rep.*, vol. 65, no. 1, pp. 1–44, 2010.

[10] R. Schürmann, T. Tsering, K. Tanzer, S. Denifl, S. Kumar, and I. Bald, “Resonant formation of strand breaks in sensitized oligonucleotides induced by low-energy electrons (0.5–9 ev),” *Angew. Chem. Int. Ed.*, vol. 56, no. 36, pp. 10952–10955, 2017.

[11] W. C. Stolte, Y. Lu, J. A. Samson, O. Hemmers, D. L. Hansen, S. B. Whitfield, H. Wang, P. Glans, and D. W. Lindle, “The K-shell auger decay of atomic oxygen,” *J. Phys. B: At. Mol. Opt. Phys.*, vol. 30, no. 20, p. 4489, 1997.

[12] T. Gorczyca and B. McLaughlin, “Inner-shell photoexcited resonances in atomic oxygen,” *J. Phys. B: At. Mol. Opt. Phys.*, vol. 33, no. 24, p. L859, 2000.

[13] S. Petrie and D. K. Bohme, “Ions in space,” *Mass Spectrom. Rev.*, vol. 26, no. 2, pp. 258–280, 2007.

[14] W. D. Geppert and M. Larsson, “Dissociative recombination in the interstellar medium and planetary ionospheres,” *Mol. Phys.*, vol. 106, no. 16-18, pp. 2199–2226, 2008.

[15] N. J. Mason, B. Nair, S. Jheeta, and E. Szymanska, “Electron induced chemistry: a new frontier in astrochemistry,” *Faraday Discuss.*, vol. 168, pp. 235–247, 2014.

[16] M. C. Boyer, N. Rivas, A. A. Tran, C. A. Verish, and C. R. Arumainayagam, “The role of low-energy ($\leq$ 20 ev) electrons in astrochemistry,” *Surf. Sci*, vol. 652, pp. 26–32, 2016.

[17] T. J. Millar, C. Walsh, and T. A. Field, “Negative ions in space,” *Chem. Rev.*, vol. 117, no. 3, pp. 1765–1795, 2017.

[18] C. Bressler and M. Chergui, “Ultrafast X-ray absorption spectroscopy,” *Chem. Rev.*, vol. 104, no. 4, pp. 1781–1812, 2004.

[19] P. B. Corkum and F. Krausz, "Attosecond science," *Nature physics*, vol. 3, no. 6, pp. 381–387, 2007.

[20] V. Strelkov, "Role of autoionizing state in resonant high-order harmonic generation and attosecond pulse production," *Phys. Rev. Lett.*, vol. 104, no. 12, p. 123901, 2010.

[21] J. Ullrich, A. Rudenko, and R. Moshammer, "Free-electron lasers: New avenues in molecular physics and photochemistry," *Annu. Rev. Phys. Chem.*, vol. 63, no. 1, pp. 635–660, 2012.

[22] G. Sansone, F. Kelkensberg, J. Pérez-Torres, F. Morales, M. F. Kling, W. Siu, O. Ghafur, P. Johnsson, M. Swoboda, E. Benedetti, *et al.*, "Electron localization following attosecond molecular photoionization," *Nat.*, vol. 465, no. 7299, pp. 763–766, 2010.

[23] J. Simons and K. D. Jordan, "Ab initio electronic structure of anions," *Chem. Rev.*, vol. 87, no. 3, pp. 535–555, 1987.

[24] J. Simons, "Molecular anions," *J. Phys. Chem. A*, vol. 112, no. 29, pp. 6401–6511, 2008.

[25] T.-C. Jagau, K. B. Bravaya, and A. I. Krylov, "Extending quantum chemistry of bound states to electronic resonances," *Annu. Rev. Phys. Chem.*, vol. 68, no. 1, pp. 525–553, 2017.

[26] T.-C. Jagau, "Theory of electronic resonances: fundamental aspects and recent advances," *Chem. Comm.*, vol. 58, no. 34, pp. 5205–5224, 2022.

[27] J. Simons, "Molecular anions perspective," *J. Phys. Chem. A*, vol. 127, no. 18, pp. 3940–3957, 2023.

[28] L. Sanche and G. Schulz, "Electron transmission spectroscopy: Rare gases," *Phys. Rev. A*, vol. 5, no. 4, p. 1672, 1972.

[29] R. Mabbs, E. R. Grumbling, K. Pichugin, and A. Sanov, "Photoelectron imaging: an experimental window into electronic structure," *Chem. Soc. Rev.*, vol. 38, no. 8, pp. 2169–2177, 2009.

[30] J. Aguilar and J.-M. Combes, “A class of analytic perturbations for one-body schrödinger hamiltonians,” *Commun. Math. Phys.*, vol. 22, pp. 269–279, 1971.

[31] E. Balslev and J.-M. Combes, “Spectral properties of many-body schrödinger operators with dilatation-analytic interactions,” *Commun. Math. Phys.*, vol. 22, pp. 280–294, 1971.

[32] D. T. Chuljian and J. Simons, “Coordinate rotation studies of H^-, He^-, Be^-, Mg^- resonances: Basis set and configuration list dependence,” *Int. J. Quantum Chem.*, vol. 23, no. 5, pp. 1723–1738, 1983.

[33] N. Moiseyev and J. Hirschfelder, “Representation of several complex coordinate methods by similarity transformation operators,” *J. Chem. Phys.*, vol. 88, no. 2, pp. 1063–1065, 1988.

[34] G. Jolicard and E. J. Austin, “Optical potential stabilisation method for predicting resonance levels,” *Chem. Phys. Lett.*, vol. 121, no. 1-2, pp. 106–110, 1985.

[35] G. Jolicard and E. J. Austin, “Optical potential method of calculating resonance energies and widths,” *Chem. Phys.*, vol. 103, no. 2-3, pp. 295–302, 1986.

[36] U. Riss and H.-D. Meyer, “Calculation of resonance energies and widths using the complex absorbing potential method,” *J. Phys. B: At. Mol. Opt. Phys.*, vol. 26, no. 23, p. 4503, 1993.

[37] U. V. Riss and H.-D. Meyer, “Reflection-free complex absorbing potentials,” *J. Phys. B At. Mol. Opt. Phys.*, vol. 28, no. 8, p. 1475, 1995.

[38] N. Rom, E. Engdahl, and N. Moiseyev, “Tunneling rates in bound systems using smooth exterior complex scaling within the framework of the finite basis set approximation,” *J. Chem. Phys.*, vol. 93, no. 5, pp. 3413–3419, 1990.

[39] H. O. Karlsson, “Accurate resonances and effective absorption of flux using smooth exterior scaling,” *J. Chem. Phys.*, vol. 109, no. 21, pp. 9366–9371, 1998.

[40] N. Moiseyev, “Derivations of universal exact complex absorption potentials by the generalized complex coordinate method,” *J. Phys. B At. Mol. Opt. Phys.*, vol. 31, no. 7, p. 1431, 1998.

[41] D. J. Kalita and A. K. Gupta, “Use of modified smooth exterior scaling method as an absorbing potential and its application,” *J. Chem. Phys.*, vol. 134, no. 9, 2011.

[42] M. Banuary and A. K. Gupta, “Application of modified smooth exterior scaling method to study $^2\pi_g$ N_2^- and $^2\pi$ CO^- shape resonances,” *ACS omega*, vol. 8, no. 7, pp. 7143–7150, 2023.

[43] M. Banuary, D. Kumar, and A. K. Gupta, “Use of the dilated electron propagator in conjunction with the modified smooth exterior scaling method to characterize ^2S $Be^+(1s^{-1})$, ^2S $Ne^+(1s^{-1})$ auger and ^2P Be^- shape resonances,” *New J. Chem.*, vol. 48, no. 11, pp. 4772–4782, 2024.

[44] J. Aguilar and J.-M. Combes, “A class of analytic perturbations for one-body schrödinger hamiltonians,” *Commun. Math. Phys.*, vol. 22, no. 4, pp. 269–279, 1971.

[45] E. Balslev and J.-M. Combes, “Spectral properties of many-body schrödinger operators with dilatation-analytic interactions,” *Commun. Math. Phys.*, vol. 22, no. 4, pp. 280–294, 1971.

[46] B. Simon, “Quadratic form techniques and the balslev-combes theorem,” *Commun. Math. Phys.*, vol. 27, no. 1, pp. 1–9, 1972.

[47] T. Rescigno, C. McCurdy Jr, and A. E. Orel, “Extensions of the complex-coordinate method to the study of resonances in many-electron systems,” *Phys. Rev. A*, vol. 17, no. 6, p. 1931, 1978.

[48] M. Mishra, Y. Öhrn, and P. Froelich, “Self-consistent field theory of dilated atomic hamiltonians: Some remarks,” *Phys. Lett. A*, vol. 84, no. 1, pp. 4–8, 1981.

[49] M. Mishra, P. Froelich, and Y. Öhrn, “The dilated electron propagator: a bi-orthogonal approach,” *Chem. Phys. Lett.*, vol. 81, no. 2, pp. 339–346, 1981.

[50] D. L. Whitenack and A. Wasserman, "Density functional resonance theory of unbound electronic systems," *Phys. Rev. Lett.*, vol. 107, no. 16, p. 163002, 2011.

[51] K. Samanta and D. L. Yeager, "Investigation of ^{2}P Be^- shape resonances using a quadratically convergent complex multiconfigurational self-consistent field method," *J. Phys. Chem. B*, vol. 112, no. 50, pp. 16214–16219, 2008.

[52] K. Samanta and D. L. Yeager, "Obtaining positions and widths of scattering resonances from a complex multiconfigurational self-consistent field state using the M_1 method," *Int. J. Quantum Chem.*, vol. 110, no. 4, pp. 798–812, 2010.

[53] Y. Sajeev and N. Moiseyev, "Reflection-free complex absorbing potential for electronic structure calculations: Feshbach-type autoionization resonances of molecules," *J. Chem. Phys.*, vol. 127, no. 3, p. 034105, 2007.

[54] N. Moiseyev and C. Corcoran, "Autoionizing states of H_2 and H_2^- using the complex-scaling method," *Phys. Rev. A*, vol. 20, no. 3, p. 814, 1979.

[55] M. N. Medikeri and M. K. Mishra, "Treatment of molecular resonances using the bi-orthogonal dilated electron propagator with application to the $^2\pi_g$ shape resonance in e-N_2 scattering," *Int. J. Quantum Chem.*, vol. 52, no. S28, pp. 29–37, 1994.

[56] M. N. Medikeri and M. K. Mishra, "Characterization of molecular shape resonances using different decouplings of the dilated electron propagator with application to $^2\pi$ CO- and $^2B_{2g}$ $C_2H_4^-$ shape resonances," *J. Chem. Phys.*, vol. 103, no. 2, pp. 676–682, 1995.

[57] S. Mahalakshmi and M. K. Mishra, "The $^2B_1$ shape resonance in electron-formaldehyde scattering: an investigation using the dilated electron propagator method," *Chem. Phys. Lett.*, vol. 296, no. 1-2, pp. 43–50, 1998.

[58] A. Venkatnathan and M. K. Mishra, "The $^2\pi_g$ shape resonance in electron-acetylene scattering: an investigation using the dilated electron propagator method," *Chem. Phys. Lett.*, vol. 296, no. 3-4, pp. 223–232, 1998.

[59] S. Mahalakshmi and M. Mishra, "Basis set, correlation and relaxation effects in the characterisation of electron-molecule scattering resonances using the

dilated electron propagator method with application to the $^2\pi_g$ N_2^-shape resonances," *Indian J. Chem. Sect. A*, vol. 39, no. 1/3, pp. 22–31, 2000.

[60] N. Lipkin, N. Moiseyev, and E. Brändas, "Resonances by the exterior-scaling method within the framework of the finite-basis-set approximation," *Phys. Rev. A*, vol. 40, no. 2, p. 549, 1989.

[61] B. Simon, "The definition of molecular resonance curves by the method of exterior complex scaling," *Phys. Lett. A*, vol. 71, no. 2-3, pp. 211–214, 1979.

[62] N. Moiseyev, *Non-Hermitian Quantum Mechanics.* Cambridge University Press, 2011.

[63] C. McCurdy Jr and T. Rescigno, "Extension of the method of complex basis functions to molecular resonances," *Phys. Rev. Lett.*, vol. 41, no. 20, p. 1364, 1978.

[64] C. W. McCurdy, J. G. Lauderdale, and R. C. Mowrey, "Complex self-consistent-field calculations on shape resonances in electron-Mg and electron-Ca scattering," *J. Chem. Phys.*, vol. 75, no. 4, pp. 1835–1842, 1981.

[65] J. G. Lauderdale, C. W. McCurdy, and A. U. Hazi, "Conversion of bound states to resonances with changing internuclear distance in molecular anions," *J. Chem. Phys.*, vol. 79, no. 5, pp. 2200–2205, 1983.

[66] M. Honigmann, R. J. Buenker, and H.-P. Liebermann, "Complex self-consistent field and multireference single-and double-excitation configuration interaction calculations for the $^2\pi_g$ resonance state of N_2^-," *J. Chem. Phys.*, vol. 125, no. 23, 2006.

[67] M. Honigmann, R. J. Buenker, and H.-P. Liebermann, "Complex multireference configuration interaction calculations employing a coupled diabatic representation for the $^2\pi_g$ resonance states of N_2^-," *J. Chem. Phys.*, vol. 131, no. 3, 2009.

[68] M. Honigmann, R. J. Buenker, and H.-P. Liebermann, "Complex configuration interaction calculations of the cross section for the dissociative electron attachment process $e^- + F_2 \rightarrow F_2^- \rightarrow F + F^-$ using the complex basis function method," *J. Comput. Chem.*, vol. 33, no. 4, pp. 355–362, 2012.

[69] A. F. White, E. Epifanovsky, C. W. McCurdy, and M. Head-Gordon, "Second order møller-plesset and coupled cluster singles and doubles methods with complex basis functions for resonances in electron-molecule scattering," *J. Chem. Phys.*, vol. 146, no. 23, p. 234107, 2017.

[70] A. F. White, M. Head-Gordon, and C. W. McCurdy, "Complex basis functions revisited: Implementation with applications to carbon tetrafluoride and aromatic n-containing heterocycles within the static-exchange approximation," *J. Chem. Phys.*, vol. 142, no. 5, 2015.

[71] A. F. White, C. W. McCurdy, and M. Head-Gordon, "Restricted and unrestricted non-hermitian hartree-fock: Theory, practical considerations, and applications to metastable molecular anions," *J. Chem. Phys.*, vol. 143, no. 7, 2015.

[72] R. Santra and L. S. Cederbaum, "Complex absorbing potentials in the framework of electron propagator theory. i. general formalism," *J. Chem. Phys.*, vol. 117, no. 12, pp. 5511–5521, 2002.

[73] S. Feuerbacher, T. Sommerfeld, R. Santra, and L. S. Cederbaum, "Complex absorbing potentials in the framework of electron propagator theory. ii. application to temporary anions," *J. Chem. Phys.*, vol. 118, no. 14, pp. 6188–6199, 2003.

[74] Y. Sajeev, R. Santra, and S. Pal, "Analytically continued fock space multireference coupled-cluster theory: Application to the $^2\pi_g$ shape resonance in e-N_2 scattering," *J. Chem. Phys.*, vol. 122, no. 23, 2005.

[75] D. Zuev, T.-C. Jagau, K. B. Bravaya, E. Epifanovsky, Y. Shao, E. Sundstrom, M. Head-Gordon, and A. I. Krylov, "Complex absorbing potentials within EOM-CC family of methods: Theory, implementation, and benchmarks," *J. Chem. Phys.*, vol. 141, no. 2, 2014.

[76] T.-C. Jagau, D. Zuev, K. B. Bravaya, E. Epifanovsky, and A. I. Krylov, "A fresh look at resonances and complex absorbing potentials: Density matrix-based approach," *J. Phys. Chem. Lett.*, vol. 5, no. 2, pp. 310–315, 2014.

[77] A. Landau and N. Moiseyev, “Molecular resonances by removing complex absorbing potentials via Padé; application to CO^- and N_2^-,” *J. Chem. Phys.*, vol. 145, no. 16, 2016.

[78] M. Ehara, Y. Kanazawa, and T. Sommerfeld, “Low-lying $\pi^\star$ resonances associated with cyano groups: A CAP/SAC-CI study,” *Chem. Phys.*, vol. 482, pp. 169–177, 2017.

[79] S. Das, Y. Sajeev, and K. Samanta, “An electron propagator approach based on a multiconfigurational reference state for the investigation of negative-ion resonances using a complex absorbing potential method,” *J. Chem. Theory Comput.*, vol. 16, no. 8, pp. 5024–5034, 2020.

[80] M. Thodika and S. Matsika, “Projected complex absorbing potential multireference configuration interaction approach for shape and feshbach resonances,” *J. Chem. Theory Comput.*, vol. 18, no. 6, pp. 3377–3390, 2022.

[81] D. J. Tozer and F. De Proft, “Modeling temporary anions in density functional theory: Calculation of the Fukui function,” *J. Chem. Phys.*, vol. 127, no. 3, 2007.

[82] N. Sablon, F. De Proft, P. Geerlings, and D. J. Tozer, “On the position of the potential wall in DFT temporary anion calculations,” *Phys. Chem. Chem. Phys.*, vol. 9, no. 44, pp. 5880–5884, 2007.

[83] H. S. Taylor, “Models, interpretations, and calculations concerning resonant electron scattering processes in atoms and molecules,” *Adv. Chem. Phys.*, pp. 91–147, 1970.

[84] A. U. Hazi and H. S. Taylor, “Stabilization method of calculating resonance energies: Model problem,” *Phys. Rev. A*, vol. 1, no. 4, p. 1109, 1970.

[85] J. Simons, “Resonance state lifetimes from stabilization graphs,” *J. Chem. Phys.*, vol. 75, no. 5, pp. 2465–2467, 1981.

[86] J. G. Lauderdale and D. G. Truhlar, “Stabilization calculations of resonance energies for the coplanar reactions H+FH and H+H_2,” *J. Chem. Phys.*, vol. 84, no. 1, pp. 192–196, 1986.

[87] A. Macías and A. Riera, “Stabilization versus feshbach techniques in the determination of resonances,” *Chem. Phys. Lett.*, vol. 139, no. 3-4, pp. 300–305, 1987.

[88] A. Macias and A. Riera, “On calculations of resonance parameters from stabilization graphs,” *J. Chem. Phys.*, vol. 96, no. 4, pp. 2877–2880, 1992.

[89] J. Simons, “Analysis of stabilization and extrapolation methods for determining energies and lifetimes of metastable electronic states,” *J. Phys. Chem. A*, vol. 125, no. 35, pp. 7735–7749, 2021.

[90] B. Nestmann and S. Peyerimhoff, “Calculation of the discrete component of resonance states in negative ions by variation of nuclear charges,” *J. Phys. B: At. Mol. Phys.*, vol. 18, no. 4, p. 615, 1985.

[91] B. Nestmann and S. Peyerimhoff, “CI method for determining the location and width of resonances in electron-molecule collision processes,” *J. Phys. B: At. Mol. Phys.*, vol. 18, no. 21, p. 4309, 1985.

[92] T. Sommerfeld, U. Riss, H. Meyer, L. Cederbaum, B. Engels, and H. Suter, “Temporary anions-calculation of energy and lifetime by absorbing potentials: The resonance,” *J. Phys. B: At. Mol. Opt. Phys.*, vol. 31, no. 18, p. 4107, 1998.

[93] I. Anusiewicz and P. Skurski, “Shape resonance of the ethylene anion stabilized in a molecular trap,” *Chem. Phys. Lett.*, vol. 370, no. 3-4, pp. 345–352, 2003.

[94] S. Feuerbacher, T. Sommerfeld, and L. S. Cederbaum, “Extrapolating bound state data of anions into the metastable domain,” *J. Chem. Phys.*, vol. 121, no. 14, pp. 6628–6633, 2004.

[95] T. Sommerfeld and M. Ehara, “Short-range stabilizing potential for computing energies and lifetimes of temporary anions with extrapolation methods,” *J. Chem. Phys.*, vol. 142, no. 3, 2015.

[96] Z. Bacic and J. Simons, “Resonance energies and lifetimes from stabilization-based methods,” *J. Phys. Chem.*, vol. 86, no. 7, pp. 1192–1200, 1982.

[97] A. Whitehead, R. Barrios, and J. Simons, “Stabilization calculation of the energy and lifetime of metastable SO_4^{2-},” *J. Chem. Phys.*, vol. 116, no. 7, pp. 2848–2851, 2002.

[98] P. Sangwan and Vikas, “Exploring the metastability and the pathways for polyanionic isomerization in the dianions and trianions of doubly-and triply-deprotonated benzene,” *Theor. Chem. Acc.*, vol. 134, pp. 1–25, 2015.

[99] P. Sangwan and V. Vikas, “Molecular anions of polydeprotonated naphthalenes: An investigation on the metastability and deprotonation energies using nuclear-charge stabilization method,” *J. Chem. Phys.*, vol. 144, no. 4, 2016.

[100] P. Sangwan, R. Kaur, *et al.*, “Chemical pathways for poly-anionic isomerisation in the metastable anions of tetra-deprotonated naphthalene: an intra-molecular inter-ring proton-transfer,” *Phys. Chem. Chem. Phys.*, vol. 19, no. 18, pp. 11571–11580, 2017.

[101] J. Horáček, P. Mach, and J. Urban, “Calculation of S-matrix poles by means of analytic continuation in the coupling constant: Application to the $^2\pi_g$ state of N_2^-,” *Phys. Rev. A*, vol. 82, no. 3, p. 032713, 2010.

[102] E. Arthur-Baidoo, K. Falkiewicz, L. Chomicz-Mańka, A. Czaja, S. Demkowicz, K. Biernacki, W. Kozak, J. Rak, and S. Denifl, “Electron-induced decomposition of uracil-5-yl o-(n, n-dimethylsulfamate): role of methylation in molecular stability,” *Int. J. Mol. Sci.*, vol. 22, no. 5, p. 2344, 2021.

[103] J. Horáček, I. Paidarová, and R. Čurík, “On a simple way to calculate electronic resonances for polyatomic molecules,” *J. Chem. Phys.*, vol. 143, no. 18, 2015.

[104] A. Szabo and N. S. Ostlund, *Modern quantum chemistry: introduction to advanced electronic structure theory.* Courier Corporation, 2012.

[105] D. A. Mazziotti, M. K. Mishra, and H. A. Rabitz, “Energy eigenvalues and eigenvectors for bound quantum systems using parametric equations of motion,” *J. Phys. Chem.*, vol. 99, no. 1, pp. 112–117, 1995.

[106] P. Pechukas, “Distribution of energy eigenvalues in the irregular spectrum,” *Phys. Rev. Lett.*, vol. 51, no. 11, p. 943, 1983.

[107] T. Yukawa, “Lax form of the quantum mechanical eigenvalue problem,” *Phys. Lett. A*, vol. 116, no. 5, pp. 227–230, 1986.

[108] X. Yang and J. Burgdörfer, “Statistics of avoided crossings for generic quantum systems,” *Phys. Rev. A*, vol. 48, no. 1, p. 83, 1993.

[109] P. Gross, A. Gupta, D. B. Bairagi, and M. K. Mishra, “An efficient method for determining quantum dynamics in strong fields by integrating through amplitude and frequency parameter space,” *Chem. Phys. Lett.*, vol. 236, no. 1-2, pp. 8–14, 1995.

[110] A. K. Gupta, P. Gross, D. B. Bairagi, and M. K. Mishra, “Laser control of population dynamics with bichromatic fields: direct search through field amplitude, frequency, and phase space,” *Chem. Phys. Lett.*, vol. 257, no. 5-6, pp. 658–664, 1996.

[111] D. J. Kalita, A. Rao, I. Rajvanshi, and A. K. Gupta, “Application of parametric equations of motion to study the laser induced multiphoton dissociation of H_2^+ in intense laser field,” *J. Chem. Phys.*, vol. 134, no. 22, 2011.

[112] D. Kalita and A. K. Gupta, “Laser-induced multiphoton dissociation of H_2^+ as a function of the field frequency using parametric equations of motion,” *Phys. Rev. A*, vol. 85, no. 3, p. 033413, 2012.

[113] D. J. Kalita and A. K. Gupta, “Application of parametric equations of motion to study the resonance coalescence in H_2^+,” *J. Chem. Phys.*, vol. 137, no. 21, 2012.

[114] J. Linderberg and Y. Öhrn, *Propagators in quantum chemistry.* John Wiley & Sons, 2004.

[115] C. D. Sherrill and H. F. Schaefer III, “The configuration interaction method: Advances in highly correlated approaches,” in *Adv. Quantum Chem.*, vol. 34, pp. 143–269, Elsevier, 1999.

[116] C. Møller and M. S. Plesset, "Note on an approximation treatment for many-electron systems," *Phys. Rev.*, vol. 46, pp. 618–622, Oct 1934.

[117] R. J. Bartlett and G. D. Purvis, "Many-body perturbation theory, coupled-pair many-electron theory, and the importance of quadruple excitations for the correlation problem," *Int. J. Quantum Chem.*, vol. 14, no. 5, pp. 561–581, 1978.

[118] R. J. Bartlett, "Perspective on coupled-cluster theory. the evolution toward simplicity in quantum chemistry," *Phys. Chem. Chem. Phys.*, vol. 26, pp. 8013–8037, 2024.

[119] A. I. Krylov, "Equation-of-motion coupled-cluster methods for open-shell and electronically excited species: The hitchhiker's guide to fock space," *Annu. Rev. Phys. Chem.*, vol. 59, pp. 433–462, 2008.

[120] J. F. Stanton and R. J. Bartlett, "The equation of motion coupled-cluster method. a systematic biorthogonal approach to molecular excitation energies, transition probabilities, and excited state properties," *J. Chem. Phys.*, vol. 98, no. 9, pp. 7029–7039, 1993.

[121] K. Fukui, T. Yonezawa, and H. Shingu, "A molecular orbital theory of reactivity in aromatic hydrocarbons," *J. Chem. Phys.*, vol. 20, no. 4, pp. 722–725, 1952.

[122] R. B. Woodward and R. Hoffmann, "The conservation of orbital symmetry," *Angew. Chem., Int. Ed. Engl.*, vol. 8, no. 11, pp. 781–853, 1969.

[123] G. J. Schulz, "Resonances in electron impact on diatomic molecules," *Rev. Mod. Phys.*, vol. 45, pp. 423–486, Jul 1973.

[124] K. D. Jordan and P. D. Burrow, "Studies of the temporary anion states of unsaturated hydrocarbons by electron transmission spectroscopy," *Acc. Chem. Res.*, vol. 11, no. 9, pp. 341–348, 1978.

[125] J. Simons and K. D. Jordan, "Ab initio electronic structure of anions," *Chem. Rev.*, vol. 87, no. 3, pp. 535–555, 1987.

[126] D. Chen and G. A. Gallup, “The relationship of the virtual orbitals of self-consistent-field theory to temporary negative ions in electron scattering from molecules,” *J. Chem. Phys.*, vol. 93, no. 12, pp. 8893–8901, 1990.

[127] M. N. Medikeri and M. K. Mishra, “Lowest unoccupied molecular orbital as the resonant orbital. an investigation using the bi-variational self-consistent field method,” *Chem. Phys. Lett.*, vol. 246, no. 1-2, pp. 26–32, 1995.

[128] T. Sommerfeld and M. Ehara, “Short-range stabilizing potential for computing energies and lifetimes of temporary anions with extrapolation methods,” *J. Chem. Phys.*, vol. 142, p. 034105, 01 2015.

[129] N. H. Beebe, “Modification of virtual orbitals,” *Int. J. Quantum Chem.*, vol. 15, no. 6, pp. 589–600, 1979.

[130] W. L. Luken and B. A. Seiders, “Interaction-optimized virtual orbitals, i. external double excitations,” *Chem. Phys.*, vol. 92, no. 2-3, pp. 235–246, 1985.

[131] R. Caballol and J.-P. Malrieu, “Improved non-valence virtual orbitals for CI calculations,” *Chem. Phys.*, vol. 140, no. 1, pp. 7–18, 1990.

[132] A. I. Krylov, “From orbitals to observables and back,” *J. Chem. Phys.*, vol. 153, no. 8, 2020.

[133] M. W. Schmidt, E. A. Hull, and T. L. Windus, “Valence virtual orbitals: An unambiguous ab initio quantification of the LUMO concept,” *J. Phys. Chem. A*, vol. 119, no. 41, pp. 10408–10427, 2015.

[134] D. Hait and M. Head-Gordon, “Orbital optimized density functional theory for electronic excited states,” *J. Phys. Chem. Lett.*, vol. 12, no. 19, pp. 4517–4529, 2021.

[135] R. Z. Khaliullin, A. T. Bell, and M. Head-Gordon, “Analysis of charge transfer effects in molecular complexes based on absolutely localized molecular orbitals,” *J. Chem. Phys.*, vol. 128, no. 18, 2008.

[136] M. Falcetta and K. Jordan, “Ab initio investigation of the temporary anion states of silane and the linear silanes:(Si_nH_{2n+2}), n= 2–5,” *Chem. Phys. Lett.*, vol. 300, no. 5, pp. 588–594, 1999.

[137] C.-S. Chen, T.-H. Feng, and J. S.-Y. Chao, "Stabilized koopmans' theorem calculations on the $\pi^\star$ temporary anion states of benzene and substituted benzenes," *J. Phys. Chem.*, vol. 99, no. 21, pp. 8629–8632, 1995.

[138] I. Anusiewicz, P. Skurski, and J. Simons, "Finding valence antibonding levels while avoiding rydberg, pseudo-continuum, and dipole-bound orbitals," *J. Am. Chem. Soc.*, vol. 144, no. 25, pp. 11348–11363, 2022.

[139] S. Miertuš, E. Scrocco, and J. Tomasi, "Electrostatic interaction of a solute with a continuum. a direct utilizaion of ab initio molecular potentials for the prevision of solvent effects," *Chem. Phys.*, vol. 55, no. 1, pp. 117–129, 1981.

[140] S. Miertus and J. Tomasi, "Approximate evaluations of the electrostatic free energy and internal energy changes in solution processes," *Chem. Phys.*, vol. 65, no. 2, pp. 239–245, 1982.

[141] M. Cossi, V. Barone, R. Cammi, and J. Tomasi, "Ab initio study of solvated molecules: a new implementation of the polarizable continuum model," *Chem. Phys. Lett.*, vol. 255, no. 4, pp. 327–335, 1996.

[142] C. Titeca, F. De Proft, and T.-C. Jagau, "Conceptual density functional theory for temporary anions stabilized by scaled nuclear charges," *J. Chem. Phys.*, vol. 157, no. 21, 2022.

[143] F. Bruneval, T. Rangel, S. M. Hamed, M. Shao, C. Yang, and J. B. Neaton, "molgw 1: Many-body perturbation theory software for atoms, molecules, and clusters," *Comput. Phys. Commun.*, vol. 208, pp. 149–161, 2016.

[144] M. e. Frisch, G. Trucks, H. B. Schlegel, G. Scuseria, M. Robb, J. Cheeseman, G. Scalmani, V. Barone, G. Petersson, H. Nakatsuji, *et al.*, "Gaussian 16," 2016.

[145] T. Lu and F. Chen, "Multiwfn: A multifunctional wavefunction analyzer," *J. Comput. Chem.*, vol. 33, no. 5, pp. 580–592, 2012.

[146] A. Venkatnathan, S. Mahalakshmi, and M. K. Mishra, "Higher order decouplings of the dilated electron propagator with applications to ^2P Be$^-$,^2P mg$^-$ shape and ^2P Be$^+(1s^{-1})$ auger resonances," *J. Chem. Phys.*, vol. 114, pp. 35–47, 01 2001.

[147] J. M. Herbert, "The quantum chemistry of loosely-bound electrons," *Reviews in Computational Chemistry Volume 28*, pp. 391–517, 2015.

[148] R. Barrios, P. Skurski, and J. Simons, "Mechanism for damage to DNA by low-energy electrons," *J. Phys. Chem. B*, vol. 106, no. 33, pp. 7991–7994, 2002.

[149] J. Simons, "How very low-energy (0.1–2 ev) electrons cause DNA strand breaks," *Adv. Quantum Chem.*, vol. 52, pp. 171–188, 2007.

[150] J. Schirmer, L. S. Cederbaum, and O. Walter, "New approach to the one-particle green's function for finite fermi systems," *Phys. Rev. A*, vol. 28, no. 3, p. 1237, 1983.

[151] M. Nooijen and R. J. Bartlett, "Equation of motion coupled cluster method for electron attachment," *J. Chem. Phys.*, vol. 102, no. 9, pp. 3629–3647, 1995.

[152] D. Kumar, M. Banuary, and A. K. Gupta, "An innovative approach for precise identification of the lowest unoccupied molecular orbital using the parametric equation of motion," *J. Chem. Theory Comput*, vol. 20, no. 14, pp. 6009–6019, 2024.

[153] D. Kumar and A. K. Gupta, "A unique approach to address avoided crossings in the charge stabilization curve for lumo identification," *J. Chem. Phys.*, vol. 161, no. 9, p. 094108, 2024.

[154] I. C. Walker, A. Stamatovic, and S. Wong, "Vibrational excitation of ethylene by electron impact: 1–11 ev," *J. Chem. Phys.*, vol. 69, no. 12, pp. 5532–5537, 1978.

[155] K.-H. Kochem, W. Sohn, K. Jung, H. Ehrhardt, and E. Chang, "Direct and resonant vibrational excitation of C_2H_2 by electron impact from 0 to 3.6 ev," *J. Phys. B: Atom. Mol. Phys.*, vol. 18, no. 6, p. 1253, 1985.

[156] O. May, J. Fedor, B. C. Ibănescu, and M. Allan, "Absolute cross sections for dissociative electron attachment to acetylene and diacetylene," *Phys. Rev. A*, vol. 77, no. 4, p. 040701, 2008.

[157] R. Dressler and M. Allan, "A dissociative electron attachment, electron transmission, and electron energy-loss study of the temporary negative ion of acetylene," *J. Chem. Phys.*, vol. 87, no. 8, pp. 4510–4518, 1987.

[158] V. Krumbach, B. Nestmann, and S. Peyerimhoff, "The $^2\pi_g$ shape resonance of the electron-acetylene scattering system: an ab initio treatment," *J. Phys. B: At. Mol. Opt. Phys.*, vol. 22, no. 24, p. 4001, 1989.

[159] M. Berman, H. Estrada, L. S. Cederbaum, and W. Domcke, "Nuclear dynamics in resonant electron-molecule scattering beyond the local approximation: The 2.3-ev shape resonance in n_2," *Phys. Rev. A*, vol. 28, no. 3, p. 1363, 1983.

[160] P. Burrow and J. Michejda, "Electron transmission study of the formaldehyde electron affinity," *Chem. Phys. Lett.*, vol. 42, no. 2, pp. 223–226, 1976.

[161] E. Van Veen, W. Van Dijk, and H. Brongersma, "Low-energy electron-impact excitation spectra of formaldehyde, acetaldehyde and acetone," *Chem. Phys.*, vol. 16, no. 3, pp. 337–345, 1976.

[162] C. Benoit and R. Abouaf, "Low-energy electron collisions with formaldehyde: interference phenomena in the differential vibrational excitation cross section," *Chem. Phys. Lett.*, vol. 123, no. 1-2, pp. 134–138, 1986.

[163] J. Berdys, I. Anusiewicz, P. Skurski, and J. Simons, "Damage to model DNA fragments from very low-energy (¡ 1 ev) electrons," *J. Am. Chem. Soc.*, vol. 126, no. 20, pp. 6441–6447, 2004.

[164] R. Abouaf and H. Dunet, "Structures in dissociative electron attachment cross-sections in thymine, uracil and halouracils," *Eur. Phys. J. D.*, vol. 35, pp. 405–410, 2005.

[165] S. Ptasinska, S. Denifl, P. Scheier, E. Illenberger, and T. Mark, "Bond-and site-selective loss of H atoms from nucleobases by very-low-energy electrons ($<$ 3 ev)," *Angew. Chem. Int. Ed.*, vol. 44, no. 42, p. 6941, 2005.

[166] T. Takayanagi, T. Asakura, and H. Motegi, "Theoretical study on the mechanism of low-energy dissociative electron attachment for uracil," *J. Phys. Chem. A*, vol. 113, no. 16, pp. 4795–4801, 2009.

[167] M. A. Fennimore and S. Matsika, "Core-excited and shape resonances of uracil," *Phys. Chem. Chem. Phys.*, vol. 18, no. 44, pp. 30536–30545, 2016.

[168] M. A. Huels, B. Boudaïffa, P. Cloutier, D. Hunting, and L. Sanche, "Single, double, and multiple double strand breaks induced in DNA by 3- 100 ev electrons," *J. Am. Chem. Soc.*, vol. 125, no. 15, pp. 4467–4477, 2003.

[169] I. Baccarelli, I. Bald, F. A. Gianturco, E. Illenberger, and J. Kopyra, "Electron-induced damage of DNA and its components: Experiments and theoretical models," *Phys. Rep.*, vol. 508, no. 1-2, pp. 1–44, 2011.

[170] E. Alizadeh, A. G. Sanz, G. Garcia, and L. Sanche, "Radiation damage to DNA: The indirect effect of low-energy electrons," *J. Phys. Chem. Lett.*, vol. 4, no. 5, pp. 820–825, 2013.

[171] Y. Shao, Y. Dong, D. Hunting, Y. Zheng, and L. Sanche, "Unified mechanism for the generation of isolated and clustered DNA damages by a single low energy (5–10 ev) electron," *J. Phys. Chem. C*, vol. 121, no. 4, pp. 2466–2472, 2017.

[172] C. Zhou, S. Matsika, M. Kotur, and T. C. Weinacht, "Fragmentation pathways in the uracil radical cation," *J. Phys. Chem. A*, vol. 116, no. 37, pp. 9217–9227, 2012.

[173] Y. Kawarai, T. Weber, Y. Azuma, C. Winstead, V. McKoy, A. Belkacem, and D. Slaughter, "Dynamics of the dissociating uracil anion following resonant electron attachment," *J. Phys. Chem. Lett.*, vol. 5, no. 21, pp. 3854–3858, 2014.

[174] M. A. Fennimore, T. N. Karsili, and S. Matsika, "Mechanisms of h and co loss from the uracil nucleobase following low energy electron irradiation," *Phys. Chem. Chem. Phys.*, vol. 19, no. 26, pp. 17233–17241, 2017.

[175] T. Sommerfeld, "Intramolecular electron transfer from dipole-bound to valence orbitals: Uracil and 5-chlorouracil," *J. Phys. Chem. A*, vol. 108, no. 42, pp. 9150–9154, 2004.

[176] H.-Y. Cheng and C.-W. Chen, "Energy and lifetime of temporary anion states of uracil by stabilization method," *J. Phys. Chem. A*, vol. 115, no. 35, pp. 10113–10121, 2011.

[177] I. Gonzalez-Ramirez, J. Segarra-Marti, L. Serrano-Andres, M. Merchan, M. Rubio, and D. Roca-Sanjuan, "On the N1-H and N3-H bond dissociation in uracil by low energy electrons: a CASSCF/CASPT2 study," *J. Chem. Theory Comput.*, vol. 8, no. 8, pp. 2769–2776, 2012.

[178] K. Aflatooni, G. A. Gallup, and P. Burrow, "Electron attachment energies of the DNA bases," *J. Phys. Chem. A*, vol. 102, no. 31, pp. 6205–6207, 1998.

[179] A. M. Scheer, K. Aflatooni, G. A. Gallup, and P. Burrow, "Bond breaking and temporary anion states in uracil and halouracils: Implications for the DNA bases," *Phys. Rev. Lett.*, vol. 92, no. 6, p. 068102, 2004.

[180] F. A. Gianturco and R. Lucchese, "Radiation damage of biosystems mediated by secondary electrons: Resonant precursors for uracil molecules," *J. Chem. Phys.*, vol. 120, no. 16, pp. 7446–7455, 2004.

[181] S. Tonzani and C. H. Greene, "Low-energy electron scattering from DNA and RNA bases: Shape resonances and radiation damage," *J. Chem. Phys.*, vol. 124, no. 5, 2006.

[182] A. Dora, J. Tennyson, L. Bryjko, and T. Van Mourik, "R-matrix calculation of low-energy electron collisions with uracil," *J. Chem. Phys.*, vol. 130, no. 16, 2009.

[183] F. Kossoski, M. Bettega, and M. d. N. Varella, "Shape resonance spectra of uracil, 5-fluorouracil, and 5-chlorouracil," *J. Chem. Phys.*, vol. 140, no. 2, 2014.

[184] M. Thodika, M. Fennimore, T. N. Karsili, and S. Matsika, "Comparative study of methodologies for calculating metastable states of small to medium-sized molecules," *J. Chem. Phys.*, vol. 151, no. 24, 2019.

[185] Y. Kanazawa, M. Ehara, and T. Sommerfeld, "Low-lying $\pi^\star$ resonances of standard and rare DNA and RNA bases studied by the projected CAP/SAC-CI method," *J. Phys. Chem. A*, vol. 120, no. 9, pp. 1545–1553, 2016.

[186] R. A. Donnelly and J. Simons, "Complex coordinate rotation of the electron propagator," *J. Chem. Phys.*, vol. 73, no. 6, pp. 2858–2866, 1980.

[187] M. J. Frisch, G. W. Trucks, H. B. Schlegel, G. E. Scuseria, M. A. Robb, J. R. Cheeseman, G. Scalmani, V. Barone, G. A. Petersson, H. Nakatsuji, X. Li, M. Caricato, A. V. Marenich, J. Bloino, B. G. Janesko, R. Gomperts, B. Mennucci, H. P. Hratchian, J. V. Ortiz, A. F. Izmaylov, J. L. Sonnenberg, D. Williams-Young, F. Ding, F. Lipparini, F. Egidi, J. Goings, B. Peng, A. Petrone, T. Henderson, D. Ranasinghe, V. G. Zakrzewski, J. Gao, N. Rega, G. Zheng, W. Liang, M. Hada, M. Ehara, K. Toyota, R. Fukuda, J. Hasegawa, M. Ishida, T. Nakajima, Y. Honda, O. Kitao, H. Nakai, T. Vreven, K. Throssell, J. A. Montgomery, Jr., J. E. Peralta, F. Ogliaro, M. J. Bearpark, J. J. Heyd, E. N. Brothers, K. N. Kudin, V. N. Staroverov, T. A. Keith, R. Kobayashi, J. Normand, K. Raghavachari, A. P. Rendell, J. C. Burant, S. S. Iyengar, J. Tomasi, M. Cossi, J. M. Millam, M. Klene, C. Adamo, R. Cammi, J. W. Ochterski, R. L. Martin, K. Morokuma, O. Farkas, J. B. Foresman, and D. J. Fox, “Gaussian˜16 Revision C.01,” 2016. Gaussian Inc. Wallingford CT.

[188] A. Ghosal, P. Joshi, and V. K. Voora, “Taming negative ion resonances using nonlocal exchange-correlation functionals,” *J. Phys. Chem. Lett.*, vol. 15, no. 22, pp. 5994–6001, 2024.

[189] K. D. Jordan and P. D. Burrow, “Temporary anion states of polyatomic hydrocarbons,” *Chem. Rev.*, vol. 87, no. 3, pp. 557–588, 1987.

[190] C. Winstead and V. McKoy, “Low-energy electron collisions with gas-phase uracil,” *J. Chem. Phys.*, vol. 125, no. 17, 2006.

[191] G. Bouskila, A. Landau, I. Haritan, N. Moiseyev, and D. Bhattacharya, “Complex energies and transition dipoles for shape-type resonances of uracil anion from stabilization curves via padé,” *J. Chem. Phys.*, vol. 156, no. 19, 2022.

[192] D. Zuev, T.-C. Jagau, K. B. Bravaya, E. Epifanovsky, Y. Shao, E. Sundstrom, M. Head-Gordon, and A. I. Krylov, “Complex absorbing potentials within EOM-CC family of methods: Theory, implementation, and benchmarks,” *J. Chem. Phys.*, vol. 141, no. 2, 2014.

[193] A. Landau and N. Moiseyev, “Molecular resonances by removing complex absorbing potentials via Padé; application to CO^- and N_2^-,” *J. Chem. Phys.*, vol. 145, no. 16, 2016.

[194] M. M. Fujimoto, E. V. de Lima, and J. Tennyson, “Elastic scattering of low-energy electrons by CH_3CN and CH_3NC molecules,” *Eur. Phys. J. D*, vol. 69, no. 6, p. 153, 2015.

[195] H.-Y. Cheng, C.-W. Chen, J.-T. Chang, and C.-C. Shih, “Application of the stabilization method to temporary anion states of CH_3CN, CH_3NC, CH_3SCN, and ch3ncs in density functional theory with asymptotically corrected potentials,” *J. Phys. Chem. A*, vol. 115, no. 1, pp. 84–93, 2011.

[196] M. Falcetta and K. D. Jordan, “Assignments of the temporary anion states of the chloromethanes,” *J. Phys. Chem.*, vol. 94, no. 15, pp. 5666–5669, 1990.

[197] M. F. Falcetta, L. A. DiFalco, D. S. Ackerman, J. C. Barlow, and K. D. Jordan, “Assessment of various electronic structure methods for characterizing temporary anion states: Application to the ground state anions of N_2, C_2H_2, C_2H_4, and C_6H_6,” *J. Phys. Chem. A*, vol. 118, no. 35, pp. 7489–7497, 2014.

[198] M. Falcetta and K. Jordan, “Ab initio investigation of the temporary anion states of silane and the linear silanes:(Si_nH_{2n+2}), n= 2-5,” *Chem. Phys. Lett.*, vol. 300, no. 5-6, pp. 588–594, 1999.

[199] H. Rajbongshi, D. Kumar, M. Banuary, and A. K. Gupta, “Study of shape resonances in silane and linear polysilanes using complex absorbing potential.” submitted, 2025.

[200] D. Kumar and A. K. Gupta, “Self-consistent-field solution for unstable anions,” *Phys. Rev. A*, vol. 110, no. 6, p. 062821, 2024.

[201] T.-C. Jagau, “Non-iterative triple excitations in equation-of-motion coupled-cluster theory for electron attachment with applications to bound and temporary anions,” *J. Chem. Phys.*, vol. 148, no. 2, 2018.

[202] D. Kumar and A. K. Gupta, “Application of parametric equations of motion to study uracil anion,” *J. Chem. Phys.*, vol. 163, no. 1, 2025.

[203] B. I. Schneider, T. N. Rescigno, B. Lengsfield III, and C. McCurdy, “Accurate ab initio treatment of low-energy electron collisions with ethylene,” *Phys. Rev. Lett.*, vol. 66, no. 21, p. 2728, 1991.

[204] C. S. Trevisan, A. E. Orel, and T. N. Rescigno, “Ab initio study of low-energy electron collisions with ethylene,” *Phys. Rev. A*, vol. 68, no. 6, p. 062707, 2003.

[205] J. Horacek, I. Paidarová, and R. Curik, “Determination of the resonance energy and width of the $^2B_{2g}$ shape resonance of ethylene with the method of analytical continuation in the coupling constant,” *J. Phys. Chem. A*, vol. 118, no. 33, pp. 6536–6541, 2014.

[206] T. Sommerfeld, J. B. Melugin, P. Hamal, and M. Ehara, “Resonance energies and lifetimes from the analytic continuation of the coupling constant method: Robust algorithms and a critical analysis,” *J. Chem. Theory Comput.*, vol. 13, no. 6, pp. 2550–2560, 2017.

[207] S. Mondal and K. B. Bravaya, “Analytic nuclear gradients for complex potential energy surfaces: A projected cap approach,” *J. Chem. Theory Comput.*, 2025.

[208] B. I. Schneider, T. N. Rescigno, and C. McCurdy, “Resonant vibrational excitation of H_2CO by low-energy electron impact,” *Phys. Rev. A*, vol. 42, no. 5, p. 3132, 1990.

[209] M. Vinodkumar, H. Bhutadia, B. Antony, and N. Mason, “Electron-impact rotationally elastic total cross sections for H_2CO and HCOOH over a wide range of incident energy (0.01–2000 ev),” *Phys. Rev. A*, vol. 84, no. 5, p. 052701, 2011.

[210] A. F. White, E. Epifanovsky, C. W. McCurdy, and M. Head-Gordon, “Second order møller-plesset and coupled cluster singles and doubles methods with complex basis functions for resonances in electron-molecule scattering,” *J. Chem. Phys.*, vol. 146, no. 23, 2017.

[211] Q. M. Phung, Y. Komori, T. Yanai, T. Sommerfeld, and M. Ehara, “Combination of a voronoi-type complex absorbing potential with the XMS-CASPT2 method and pilot applications,” *J. Chem. Theory Comput.*, vol. 16, no. 4, pp. 2606–2616, 2020.

[212] U. Riss and H. Meyer, “The transformative complex absorbing potential method: a bridge between complex absorbing potentials and smooth exterior scaling,” *J. Phys. B: At. Mol. Opt. Phys.*, vol. 31, no. 10, p. 2279, 1998.

[213] R. Santra and L. S. Cederbaum, “Non-hermitian electronic theory and applications to clusters,” *Phys. Rep.*, vol. 368, no. 1, pp. 1–117, 2002.

[214] J. G. Muga, J. Palao, B. Navarro, and I. Egusquiza, “Complex absorbing potentials,” *Phys. Rep.*, vol. 395, no. 6, pp. 357–426, 2004.

[215] T.-C. Jagau and A. I. Krylov, “Complex absorbing potential equation-of-motion coupled-cluster method yields smooth and internally consistent potential energy surfaces and lifetimes for molecular resonances,” *J. Phys. Chem. Lett.*, vol. 5, no. 17, pp. 3078–3085, 2014.

[216] R. Lefebvre, M. Sindelka, and N. Moiseyev, “Resonance positions and lifetimes for flexible complex absorbing potentials,” *Phys. Rev. A.*, vol. 72, no. 5, p. 052704, 2005.

[217] D. T. Colbert and W. H. Miller, “A novel discrete variable representation for quantum mechanical reactive scattering via the s-matrix Kohn method,” *J. Chem. Phys.*, vol. 96, no. 3, pp. 1982–1991, 1992.